DEPOSITION, CHARACTERIZATION, PATTERNING AND MECHANISTIC STUDY OF INORGANIC RESISTS FOR NEXT-GENERATION NANOLITHOGRAPHY

by

FEIXIANG LUO

A dissertation submitted to the

Graduate School-New Brunswick

Rutgers, The State University of New Jersey

In partial fulfillment of the requirements

For the degree of

Doctor of Philosophy

Graduate Program in Chemistry

Written under the direction of

Dr. Eric Garfunkel

And approved by

_____

_____

_____

_____

New Brunswick, New Jersey

May, 2016

ABSTRACT OF THE DISSERTATION

DEPOSITION, CHARACTERIZATION, PATTERNING AND MECHANISTIC STUDY OF INORGANIC RESISTS FOR NEXT-GENERATION NANOLITHOGRAPHY

by FEIXIANG LUO

Dissertation Director

Prof. Eric Garfunkel

The semiconductor industry has witnessed a continuous decrease in the size of logic, memory and other computer chip components since its birth over half a century ago. The shrinking (scaling) of components has to a large extent been enabled by the development of micro- and now nano-lithographic techniques. This thesis focuses on one central component of lithography, the resist, which is essentially a thin film that when appropriately exposed enables a pattern to be printed onto a surface. Smaller features require an ever more precisely focused photon, electron or ion beam with which to expose the resist. The likely next generation

source of radiation that will enable sub-20nm features to be written will employ extreme ultraviolet radiation (EUV), 92eV (13.5nm).

The work discussed here involves a novel class of inorganic resists (including a solution processed Hf-based resist called HafSOx), as the organic resists that have dominated the microlithography industry for the past few decades have approached fundamental scaling limits. In order to maintain the high throughput required by high volume semiconductor manufacturing, metal oxide resists have been proposed and developed to meet the resolution and sensitivity in EUV lithography. One can think of our resists as the nano-lithographic analog to the silver halide film that dominated the photographic print industry for a century.

In this thesis, we mainly describe our work on HafSOx, a “first generation” metal oxide EUV resist system. HafSOx thin films can be deposited by spin-coating a mixed solution of $HfOCl_2$, H_2O_2, and H_2SO_4. Various materials characterization techniques have been employed to achieve a comprehensive understanding of film composition and structure at both surface and bulk level, as well as a mechanistic understanding of the film radiation chemistry. Taking advantage of the high energy x-rays

used in the XPS experiment, we developed an experiment to dynamically monitor the photochemistry within the HafSOx films. Based on this experiment, we found that an insoluble Hf-O-Hf network is eventually formed after film exposure and development by the removal of SO_x, OH, and H_2O, and the cross-linking of Hf_xO_y nanoparticles. Using photoemission and complementary Raman results, and knowing that both free and bound peroxide co-exist in the precursor solution, we confirmed that there is a specific peroxide stoichiometry needed in the film to chelate to Hf. Sulfate groups were found to act as the spacers between metal oxide nanoparticles to prevent early stage nanoparticle aggregation in the as-deposited films. Too much sulfate sacrifices resist sensitivity, while too little promotes undesired nanoparticle cross-linking during film preparation.

In EUV lithography, low energy secondary electron activation had been suggested as a mechanism explaining how film exposure to EUV photons through a mask can result in a patterned film, but this hypothesis lacked experimental evidence. We constructed a low energy electron beam exposure system, exposed HafSOx resists with electrons with energy ranging from 2 eV to 100 eV, and then characterized the film changes after the exposure. Surprisingly, we found electrons with an energy as low as 2

eV can activate the film if given a sufficient electron dose. Electrons with a lower energy require higher doses to fully activate the resist. Our results strongly support the hypothesis that relatively low energy secondary electrons are central in the mechanism responsible for patterning, in this case by interacting with peroxyl species bound to Hf in the films.

With the recent arrival of a state-of-art Zeiss-Orion helium ion beam microscope at Rutgers, we also tested the patterning performance of a HafSOx resist with 30 keV He^+ ions. (HIBL = helium ion beam lithography). 30 keV He ions were found to be 50-100 more sensitive than 30 keV electrons at patterning HafSOx, and this boost was attributed to the higher stopping power of helium ions compared with electrons. Sub-10 nm critical dimensions were achieved with fairly good line edge roughness (a key metric in assessing lithographic performance). Additionally, Monte Carlo simulations were conducted to compare the ion and electron trajectories in the solid films and to investigate energy loss in the HafSOx films.

In summary, a systematic approach has been developed to understand the mechanism behind HafSOx as an EUV resist. Our work helps lead to a more comprehensive mechanistic understanding of how metal

oxide EUV photoresists work in general, and suggests ways to optimize their performance.

Acknowledgement

Life is a journey. I'm so grateful that I can stop by New Jersey for a couple of years and was offered such a great opportunity to study and do research at Rutgers. First of all, I would like to thank my thesis adviser Prof. Eric Garfunkel. When I first joined this group, he gave me tremendous freedom to do research based on my own interests and was always ready to offer his insights to help me overcome the roadblocks I encountered in my research. Meanwhile, with his help, I've got the experience working on both academic and industrial projects involving extensive teamwork and collaboration, which practiced my interpersonal skills.

I would also like to thank Viacheslav Manichev, for offering his expertise in helium ion microscope and patterning, and Mengjun Li for her help with AFM. Here, I'd like to extend my thanks to all other members of GGF (Garfunkel + Gustafsson + Feldman) group: Prof. Torgny Gustafsson, Prof. Leonard Feldman, Dr. Ning Wu, Dr. Yi Xu, Dr. Can Xu, Dr. Hao Wang, Dr. Xiuyan Li, Dr. Hong Dong Lee, Dr. Voshadhi Amarasinghe, Dr. Wenchun Feng, Dan Mastrogiovanni, Aleksandra Biedron, Malathi Kalyanikar, Shinjae Huang and Hongbin Yang.

Spending almost four years in Center for Sustainable Material Chemistry (CSMC), I really enjoyed the collaborative environment and got inspired by so many exciting research projects. I'd like to thank Prof. Douglas Keszler, Prof. Gregory Herman, Dr. Rose Ruther, Dr. Richard Oleksak, Jennie Amador, Ryan Fredrick and all other CSMC members.

For all my instrumentation work, I'd like to give my special thanks to Dr. Alexei Ermakov. His "magic fingers" fixed every problem I had during instrument installation. I would also like to thank Leszek Wielunski and Boris Yakshinskiy for both giving me immense help on RBS measurement.

I would like to thank my committee members Prof. Jing Li, Prof. KiBum Lee and Dr. Sylvie Rangan for their guidance, support and constructive suggestions on my thesis writing.

Finally, I want to take this opportunity to thank my parents and my wife for their unconditional trust and support, which will help me confidently face more challenges in the future.

Table of Contents

ABSTRACT OF THE DISSERTATION ii
Acknowledgement vii
Table of Contents ix
List of Figures xii
List of Tables xvii
Chapter 1 : Introduction xvii
1.1 Moore's Law and Microelectronic Fabrication 1
1.2 Lithography 4
1.2.1. Photolithography 8
1.2.2 E-beam lithography 13
1.3 Resist 15
1.3.1 Organic resists 18
1.3.1.1 DNQ-Novolak Resists 19
1.3.1.2 Chemical Amplification Resists (CAR) 22
1.3.2 Inorganic Resists 24
1.4 EUVL and HafSOx resist 1
1.4.1 EUV light source 31
1.4.2 Multi-layer coating and optics 34
1.4.3 Reflective mask 36
1.4.4 Resists 37
1.4.4.1 Chemically amplified resist 37
1.4.4.2 MSOx inorganic resists 38
1.4.4.3 Tin based inorganic resists 40
References 42
Chapter 2 : Characterization methods 46

2.1 X-ray Photoelectron Spectroscopy (XPS) 46
2.2 Rutherford Backscattering Spectrometry (RBS) 51
2.3 Atomic Force Microscopy (AFM) 54
2.4 Raman Spectroscopy 57
2.5 Secondary Ion Mass Spectrometry (SIMS) 59
2.6 Scanning Electron Microscope (SEM) and Helium Ion Microscope (HIM) 61
2.7 Other Characterization Methods 66
References 67
Chapter 3 : HafSOx thin film characterization 68
3.1. Introduction 68
3.2. Experimental Section 70
3.3. Results and Discussion 74
3.4. Summary 88
References 90
Chapter 4 : Radiation chemistry of HafSOx as a lithographic resist 92
4.1 Introduction 92
4.2 Experimental Section 97
4.3 Results and Discussion 98
4.4 Summary 123
References 125
Chapter 5 : Low energy electron exposure on HafSOx resists 126
5.1 Introduction 126
5.2 Experimental Section 133
5.3 Results and Discussion 136
5.4 Summary 153
References 155
Chapter 6 : Helium Ion Beam Lithography on HafSOx films 157
6.1 Introduction 157
6.2 Experimental Section 158
6.3 Results and Discussion 161
6.3.1 HafSOx resist sensitivity test with HIBL and EBL 161

6.3.2 Study of CD and LER on HafSOx resist 163
6.3.3 High dose feature inflation issues 166
6.3.4 Simulation model construction with Rutherford backscattering spectrometry (RBS) 168
6.3.5 Monte Carlo simulation of helium ions and electrons in HafSOx films 170
6.4 Summary 172
References 174
Chapter 7 Conclusions 175
Bibliography 176

List of Figures

Figure 1.1 CPU transistor counts vs the introduction year 2

Figure 1.2 Fabrication of a p-n junction: (a) A n-type Si wafer; (b) the oxidation of Si wafer; (c) deposition of photoresist; (d) exposing the resist through a patterned mask 5

Figure 1.3(a) Patterned photoresist via development; (b) pattern transferred to underneath oxide layer; (c) stripping away photoresist; (d) formation of a p-well via ion implantation; (e) metal deposition as the top contact; (f) finish of a p-n junction 6

Figure 1.4 Shadow printing methods: (a) contact printing and (b) proximity printing. 9

Figure 1.5 Schematic of a photolithographic stepper 11

Figure 1.6 The timeline of the minimum feature size achieved versus light source wavelength . 12

Figure 1.7A schematic diagram for a high energy e-beam lithography system 15

Figure 1.8 Positive tone and negative tone lithographic resists. 16

Figure 1.9 Chemical structure of a Novolac resin and a DNQ molecule..... 19

Figure 1.10 The decomposition path of the DNQ initiated by heat or photons..... 21

Figure 1.11 A typical mechanism of post-exposure bake for the chemical amplification resists . 24

Figure 1.12 The chemical structure of (a) cage form monomer (b) networked form after exposure 27

Figure 1.13 The resist chemistry change during preparation: (a) Hydrolysis and (b) Condensation 29

Figure 1.14 The working principle of LPP and DPP sources..... 32

Figure 1.15 The emission spectra of plasma generated from the Sn and Xe EUV sources. 34

Figure 2.1 The working principle of XPS exampling with a pure Cu sample..... 47

Figure 2.2 The principle of angle resolved XPS..... 50

Figure 2.3 The scheme of an AFM setup. 55

Figure 2.4 The schematic working principle of SIMS. 60

Figure 2.5 A scheme showing how a conventional SEM works. 64

Figure 3.1 An Example of a TGA curve of the $HfOCl_2$ solution mass loss in three-stage heating process. 75

Figure 3.2 XPS data for an 80˚C annealed HafSOx film on Si wafer: (a) the survey spectrum, (b) the Hf 4f spectrum, (c) the S 2p spectrum and (d) the O 1s spectrum. 77

Figure 3.3 XPS peak comparison between various temperatures: (top, a) S, (middle, b) O and (bottom, c) Hf. 80

Figure 3.4 RBS data of an 80˚C annealed HafSOx sample 83

Figure 3.5 Depth profiles of HafSOx annealing at 80˚C, 150˚C and 300˚C from MEIS. 85

Figure 3.6 Raman spectrum of a HafSOx film annealed at 80 °C. 87

Figure 4.1 The scheme of the cluster composed HafSOx films. 93

Figure 4.2 Proposed bond breaking and bond formation induced by photons/electrons with the sufficient energy 95

Figure 4.3 Film solubility change in different stages of the lithography process 96

Figure 4.4 The O XPS peak evolvement with x-ray exposure: (top left, a) 1^{st}scan, (top right, b) 5^{th}scan and (bottom, c) 20^{th} scan. 101

Figure 4.5 O1s peak B percentage change with scan number for films annealed at various temperature: (top, a) 80°C and 150 °C 102

Figure 4.6 The O1s peak B percentage change vs scan numbers for HafSOx films with various Hf-to-peroxo ratios 104

Figure 4.7 Raman spectra comparison among HafSOx precursor solutions with various Hf-to-peroxo ratios 108

Figure 4.8 The O1s peak B percentage change vs scan numbers for HafSOx films with various Hf-to-sulfate ratios..... 110

Figure 4.9 The scheme of the tested HafSOx films at different stages of a typical lithographic process..... 111

Figure 4.10 The comparison of Hf 4f XPS spectra between as-deposit and exposed & developed films..... 114

Figure 4.11 The comparison of O1s XPS spectra between (left, a) exposed & developed films and (right, b) as-deposit films..... 115

Figure 4.12 The XPS Hf 4f peaks for the HafSOx films (left, a) w/ H2O2 and (right, b) after direct development..... 117

Figure 4.13 The XPS O1s peak binding energy comparison for HafSOx films made (left, a) w/ H_2O_2 and (right, b) w/o H_2O_2 after direct development..... 119

Figure 4.14 The number of Hf in a cluster made from different HafSOx and Hf oxide/hydroxide films..... 120

Figure 4.15 The SIMS spectra comparison among different HafSOx films..... 122

Figure 5.1 An overview the potential of various resists applied in the EUV lithography..... 127

Figure 5.2 The proposed EUV photon absorption and secondary electron production and its interaction with the HafSOx film..... 129

Figure 5.3 A chart of the EUV photo-absorption cross section for various elements..... 130

Figure 5.4 The inelastic mean free path for electrons with different energies..... 132

Figure 5.5 The scheme of the low energy electron exposure system setup..... 134

Figure 5.6 Images of the real (top) sample holder, (middle) electron gun and (bottom) the chamber..... 135

Figure 5.7 An example of an energy diagram between the sample and filament**.**..... 137

Figure 5.8 The electron energy calibration: experiment design and data analysis 139

Figure 5.9 A scheme of sample design for the experiment exploring the minimum HafSOx activation energy 139

Figure 5.10 The XPS Hf mapping of (top, left) the no electron control film, (top, right) 2 eV electrons exposed film and (bottom) 50 eV electrons exposed film after 25% TMAH development. 141

Figure 5.11 (top left) An example of a XPS O1s peak fitting and XPS O component, at lower binding energy, mapping of (top, right) the no electron control film, (bottom left) 2 eV electrons exposed film and (bottom, right) 50 eV electrons exposed film after 25% TMAH development. 142

Figure 5.12 The contrast curves for HafSOx films exposed by electrons with various energies. 143

Figure 5.13 A typical example of secondary electron yield against the primary incident energy (E_p). E.g. for Mg, the usually reported E_I=20 eV, E_m=950 eV and E_{II}= 10 keV. 145

Figure 5.14 The contrast curve comparison between high energy (30 keV) and low energy (<100 eV) electron exposed films with the thickness characterized by AFM and RBS respectively..... 146

Figure 5.15 The substantial S residue was found for all 100% exposed samples by the low energy electron exposure 147

Figure 5.16 The XPS S2p peak comparison for as-deposit and low energy electron exposed and developed HafSOx films 148

Figure 5.17 The CASINO simulation on HafSOx film exposed by 100 eV electron with minimum simulation energy 5 eV (top) and 2 eV (bottom) 150

Figure 5.18 The CASINO simulation on HafSOx film exposed by 100 eV electrons with minimum simulation energy 5 eV (top) and 2 eV (bottom) 151

Figure 5.19 The electron backscattering coefficient variance according to different incident energy 153

Figure 6.1(a) The contrast curve comparison between HIBL and EBL with a 30 kV acceleration voltage, and (b) the stopping power ratio between He^{2+} and e^- in a few common materials. 162

Figure 6.2 (a) A line pattern showing below-10 nm average line width and LER (3σ) 2.9 nm and the dependence of (b) average line width and (c) LER on doses. 2, 5, 10, 20 nm are the input line width values we set in the software during exposure, not the measured real line widths. 166

Figure 6.3(a) A scheme showing the exposed square areas at various doses in units of mC/cm^2, and (b) an AFM 3D image of the film after exposure, development (25 wt.% TMAH, 1 min) and post-development hard-bake (300 °C, 5 mins). Reorganization of data in (b) into panel (c) exhibiting the change in the height of the square features as a function of dose**.** 168

Figure 6.4(a) a RBS spectrum of as-deposited HafSOx films including both experimental data and the simulated curve, and (b) a 3-layer film model derived from it. The top layer density was calculated based on areal density data (RBS) and thickness data (AFM). 169

Figure 6.5(a) The simulation result of energy loss, due to ionization, inside the HafSOx film and its substrate; (b) The trajectory comparison between He ion and electron at 30 keV. 172

List of Tables

Table 3.1 Atomic percentages of Hf, S and O in HafSOx annealed at various temperatures..... 82

Table 3.2 Areal density and calculated thickness for different temperature annealed samples.. 85

Table 4.1 Atomic percentages of each element in HafSOx films at various lithographical stages. 113

Table 4.2 Atomic percentage comparison between HafSOx w/ H_2O_2 and HafSOx w/o H_2O_2 117

Table 4.3 The XPS Hf 4f peak binding energy shift for HafSOx w/o H_2O_2after direct development. 118

Table 6.1 Resists sensitivity comparison using helium ion beam as incident particles. Acronyms: poly (methyl methacrylate) = PMMA; hydrogen silsesquioxane = HSQ; chemically amplified resist = CAR 163

Chapter 1: Introduction

1.1 Moore's Law and Microelectronic Fabrication

Decades ago, Gordon E. Moore, the co-founder of Intel, predicted[1] that approximately every two years the number of components per integrated circuit will be doubled, also known as "Moore's law".[1] In the past 50 years, Moore's laws (of exponential scaling) have projected the growth of many metrics of the semiconductor industry, such as transistor counts in microprocessors, memory capacity, cost per transistor, and pixel number in charge-coupled devices (CCD). Benefiting from the relatively accuracy of Moore's Law, semiconductor companies have used it as a golden rule to direct their research and development. **Figure 1.1** shows Intel's transistor CPU count over past 45 years, which follows Moore's Law quite well.

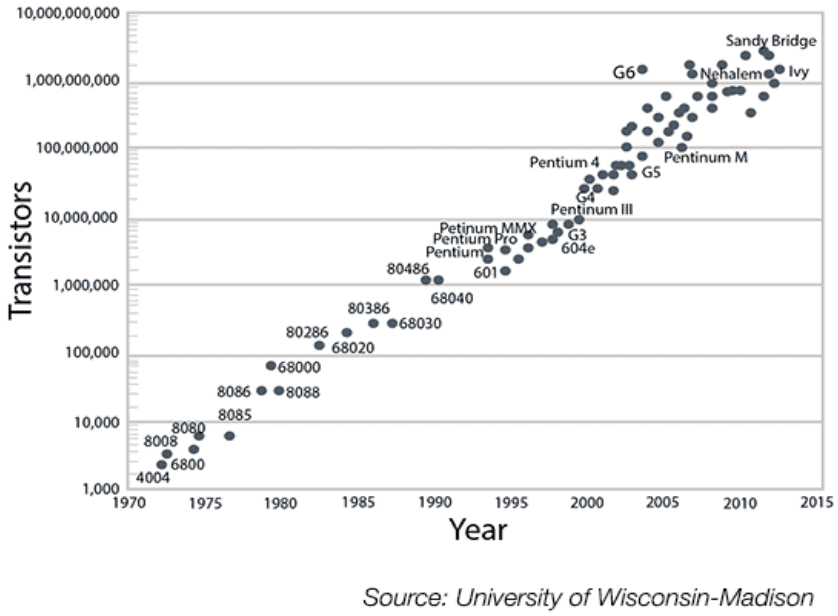

Source: University of Wisconsin-Madison

Figure 1.1 CPU transistor counts vs the introduction year[2]

With the size of transistors now close to the atomic level (the "channel" of a transistor is now of order 10-15nm across and the "gate insulator" now 1-2nm thick), it becomes an increasingly critical challenge to further scale and follow Moore's law, at least using the same materials and principles as have been developed over the past six decades. Therefore, in addition to development of integrated circuit design and packaging, new nano-fabrication methods are required if one wished to follow the roadmap suggested by Moore's Law.

Microfabrication[3, 4] now involves a series of highly integrated and complicated set of processes to fabricate nanometer-level features with

precise control. The methods developed and used must take into account all aspects of lithography, including cost, throughput, quality, variability, yield, and reliability. Currently over a thousand steps are required to fabricate a current generation microprocessor. The most important techniques include processes for cleaning, oxidation, lithography, etching, doping, deposition and planarization. **Figure 1.2** and **Figure 1.3** show the schematic of basic processes to fabricate a simple p-n junction. Starting with a bare n-type Si wafer, dry or wet oxidation is used to grow SiO_2 with a defined thickness on top of Si. Then an organic polymers based photoresist film, sensitive to UV light, is spin-coated on the surface, followed by UV exposure through a patterned mask. In the near future, organic resists will likely be replaced by inorganic ones. HafSOx, as we investigate in this thesis, is a promising inorganic photoresist candidate that can be used for extreme UV lithography (EUVL). After the exposure and development, a patterned photoresist will remain on the surface and then the pattern is further transferred to the SiO_2 layer via a wet or plasma-based etching process. After stripping away the photoresist, a window exposing bare Si below the SiO_2 will be doped with impurities by diffusion or ion implantation. Finally, front and back metal contacts can be deposited by either e-beam

deposition or thermal evaporation. Finishing these processes will result in a very simple, proof-of-concept, p-n junction. Such a device is often the first device made by students who learn basic microfabrication methods in a cleanroom.

1.2 Lithography

Lithography[5, 6], now nanolithography since many key structures in current generation integrated circuits are fabricated at the nanometer level, is one of the most vital processes in the whole chain of semiconductor microfabrication. **Figures 1.2(c), (d) and Figures 1.3(a), (b), (c)** outline a typical process flow for photolithography. Generalizing from this example, three basic steps are included: exposure, development and etching.

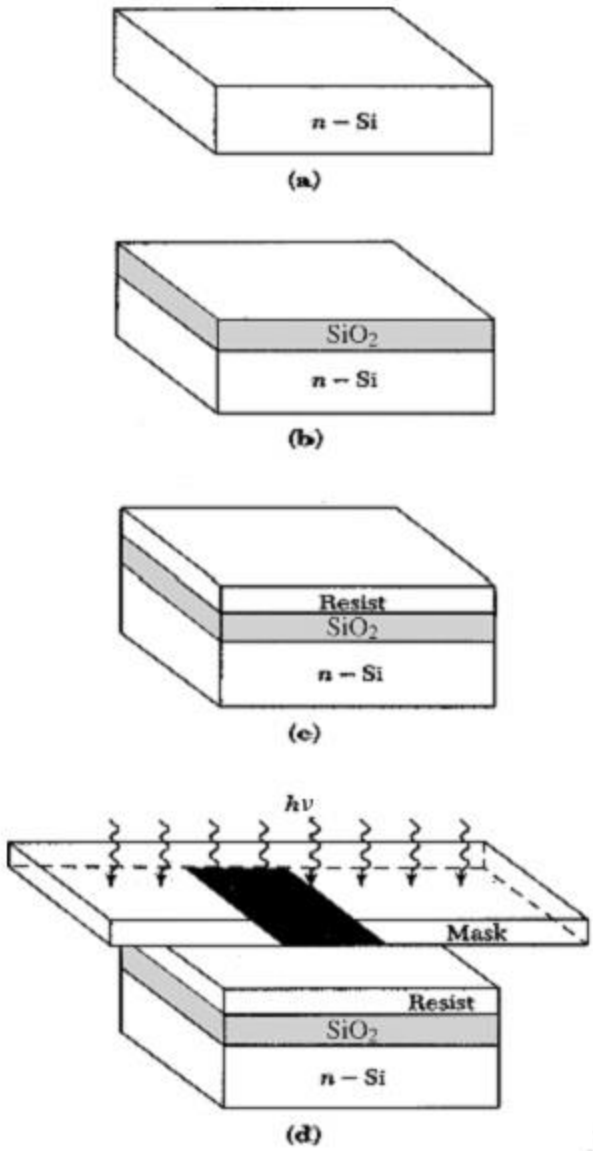

Figure 1.2 Fabrication of a p-n junction: (a) A n-type Si wafer; (b) the oxidation of Si wafer; (c) deposition of photoresist; (d) exposing the resist through a patterned mask[4]

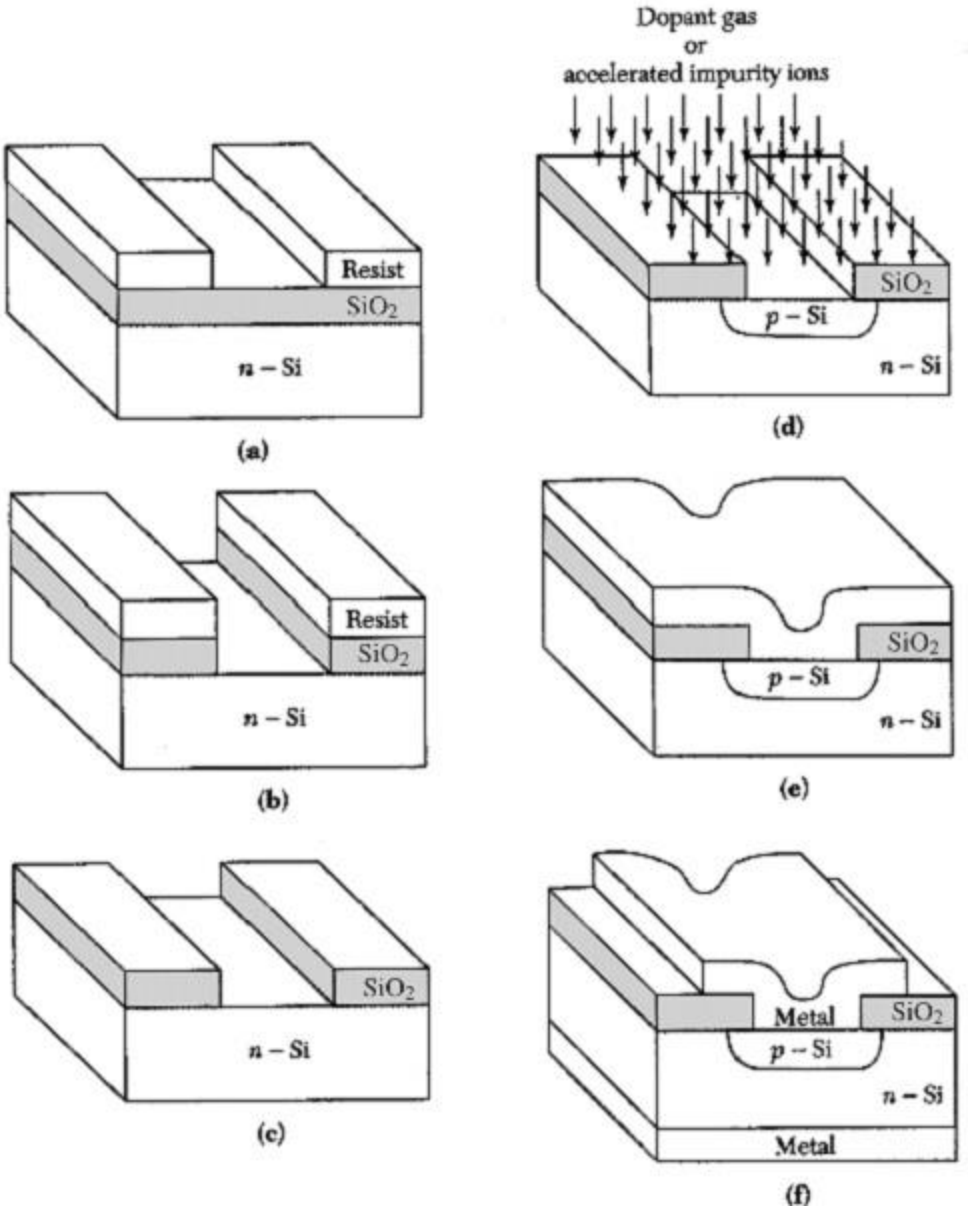

Figure 1.3(a) Patterned photoresist via development; (b) pattern transferred to underneath oxide layer; (c) stripping away photoresist; (d) formation of a p-well via ion implantation; (e) metal deposition as the top contact; (f) final p-n junction steps[4]

Exposure enables a pattern transfer from mask to resist via chemical changes that take place in the film initiated by exposure sources, such as photons or electrons, or byproducts of the initial exposure, such as secondary electrons, ions or chemical radicals within the film. The chemical changes within the film lead to a change in solubility of the resist in certain development solutions. Development takes advantage of the solubility difference between the exposed and unexposed area on the same resist. A development solution and process should dissolve away the soluble part and leave the insoluble resist, in essence, patterning surface with resist. The remaining resist should present a larger resistance against etching, protecting the resist's covered region and letting the uncovered substrate be etched. The patterned resist is then usually transferred to its substrate using either a wet chemical etch or a dry plasma etch. Anisotropic etching and etching selectivity are two major issues to consider when designing the etching processes. Other patterning methods are also used, including deposition on top of a patterned resist and lifting off the resist (and materials deposited on the resist) leaving the deposed material only in the areas containing no resist.

A variety of techniques, such as nanoimprint[7, 8], plasmonic nanolithography[9-11], and directed self-assembly[12-14], are being explored to either transfer the pattern of mask to the final target film or to masklessly achieve a target pattern. Among these and other lithographic techniques, photolithography and e-beam lithography are the two most well-developed ones with UV photolithography currently the dominant one of the semiconductor industry.

1.2.1. Photolithography

Photolithography, also known as optical lithography, was first invented by Alphonse Louis Poitevin[15], a French chemist and photographer, who found the photosensitivity of bichromated gelatin in the 19th century. After continuously development over the last two hundred years, photolithography has become the most predominant lithography method in the semiconductor industry.

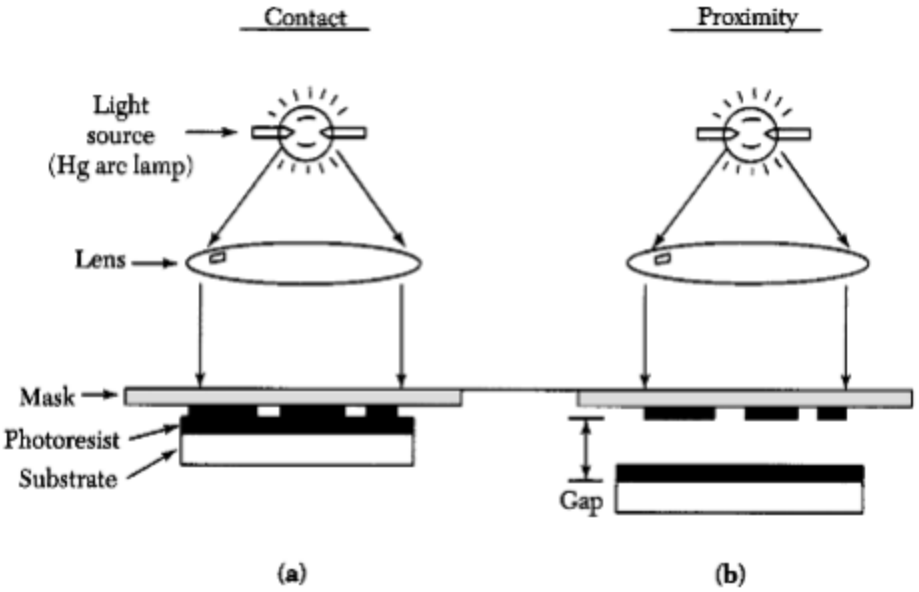

Figure 1.4 Shadow printing methods: (a) contact printing, and (b) proximity printing.[4]

In terms of the exposure tools, there are two primary methods: shadow printing and projection printing. For shadow printing, two approaches exist as shown in **Figure 1.4**. In contact printing, the photoresist intimately touches the back surface of mask during the exposure, which assists the achievement of higher resolution. However, even in a well maintained clean room, one always suffers from a dust (particulate) problem. Dust, from any number of sources, falls on the surface of the photoresist and will scratch the backside of the mask, which will in turn result in unwanted patterns on photoresists and dramatically shorten the

lifetime of masks. Proximity printing was introduced to solve the above problem. In proximity printing, a small gap around 10-50 μm is maintained between the photoresist and the photomask, which successfully avoids the dust scratching issues that exist in contact printing. However, proximity printing suffers its own problems. Undesired light diffraction will occur at the edge of the features on the photomask, exposing part of the mask-covered region and therefore reducing the final achievable resolution.

Projection printing was introduced as an alternative to avoid the compromise between resolution and mask scratching. **Figure 1.5** shows the schematic of the most important elements in a regular projection photolithographic stepper. The light-sources are mainly divided into the following wavelengths: near ultraviolet (UV) (> 300nm), deep UV (DUV, ~200nm-300 nm), and extreme UV (EUV, 10 nm-124 nm). More importantly, the wavelength of the light source determines the resolution of a projection printing system according to the equation below:

$$\mathrm{CD} = k_1 \frac{\lambda}{NA}$$

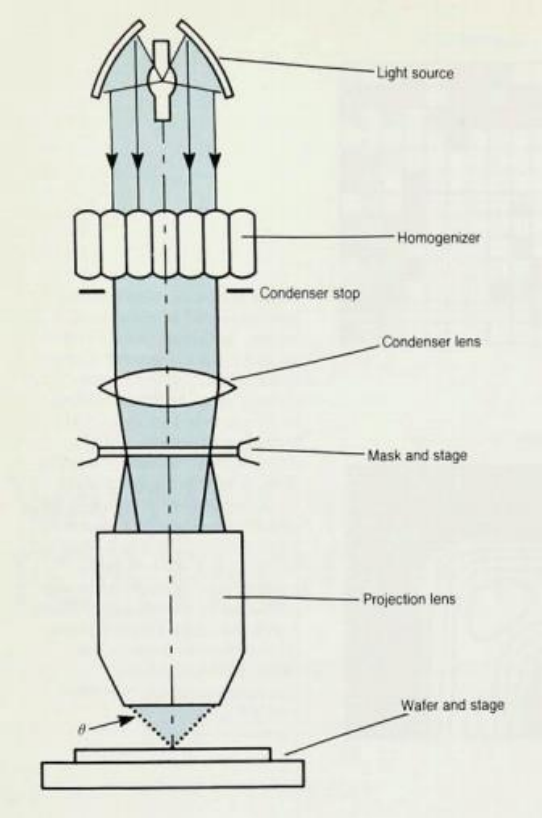

Figure 1.5 Schematic of a photolithographic stepper[16]

The CD (critical dimension) is the minimum line width that can be achieved, λ is the wavelength of incident photons, and k_1 is a process and instrument related constant. NA stands for numerical aperture, which is related to the index of refraction in the image medium and the angle of the maximum cone of light entering or exiting the lens. Shortening the wavelength of light sources is one of the most efficient methods to achieve

smaller features as is implied by the history of photolithography light source wavelength, as shown in **Figure 1.6**.

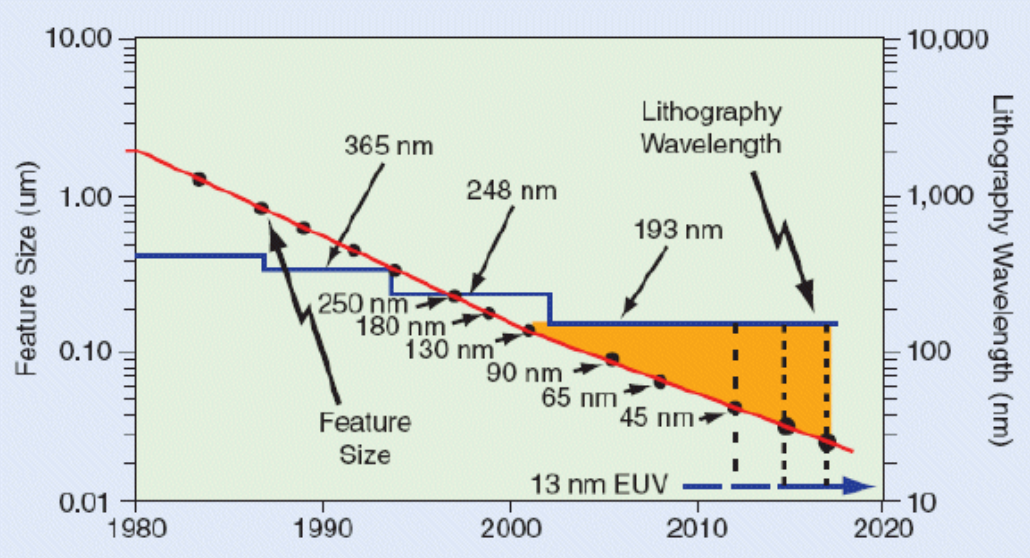

Figure 1.6 The timeline of the minimum feature size achieved versus light source wavelength[17]

A near UV light source, one of the first developed for integrated circuit fabrication, usually includes i-line (365 nm), g-line (436 nm), and h-line (405 nm) radiation emitted from a mercury arc lamp[18]. To enable critical dimensions to be fabricated below 250 nm, excimer lasers, such as KrF (248 nm) and ArF (193 nm)[19-21], were developed and have been

mainstream lithography light sources in the semiconductor industry. Although multiple-patterning techniques[22, 23] have greatly extended the limits of excimer lasers, they also dramatically increase the number of exposure steps and photomasks used, which complicates the fabrication process and adversely affects the final yield. With the demand of fabricating features smaller than 10 nm, EUV lithography[24-26] has emerged as a likely alternative and is being actively tested and developed in several semiconductor R&D departments around the world[27]. I discuss details about EUV lithography section later in this chapter.

1.2.2 E-beam lithography

Compared with photolithography, e-beam lithography[28-31] is a direct and maskless resist exposure method, which is primarily used in photomask fabrication. A schematic diagram of a high-energy e-beam lithography system is shown in **Figure 1.7**. The most commonly used thermionic emission sources for the electron gun are tungsten or iridium filaments. Single crystals of lanthanum hexaboride[32, 33] have also been utilized as they can disply longer life time, exceptional thermal, chemical and electrical stability, and more efficient electron emission resulting from its lower work

function. An alternative is a field emission gun[34] which has a low energy spread and high brightness. Different from thermionic filaments, a field emission filament is placed inside a very high electric field, which enables electrons emitted from the filament surface to have a much lower energy spread. The blanking electrode acts as a beam on/off switch. The condenser lenses, either electrostatic or electromagnetic, controls the beam spot size. The electrostatic deflector precisely allocates the e-beam spot to where it is set.

Compared with photolithography, e-beam lithography has greater depth of focus and is maskless. Thus issues of mask design, fabrication, repair and contamination disappear. However, one of the biggest disadvantages hindering e-beam lithography into wider application in the semiconductor industry is its low throughput, the time consumed to expose a certain area. The wafer writing time is estimated based on the equation[35] below:

$$\text{wafer writing time} = \text{area of the wafer} \times \text{resist sensitivity}/(\text{beam current})$$

For example, to expose a 1 cm × 1 cm area, given a reasonable resist sensitivity of 100 μC/cm^2 and a stable beam current of 1 nA, almost 28

hours are required to fully expose the entire area. E-beam lithography, in its normal mode of operation, requires a few orders of magnitude longer time than optical lithographic exposure tools as the latter can expose a large area comprised of many components at one time. Therefore, e-beam lithography is mainly used in processes not requiring high throughput, such as photomask fabrication.

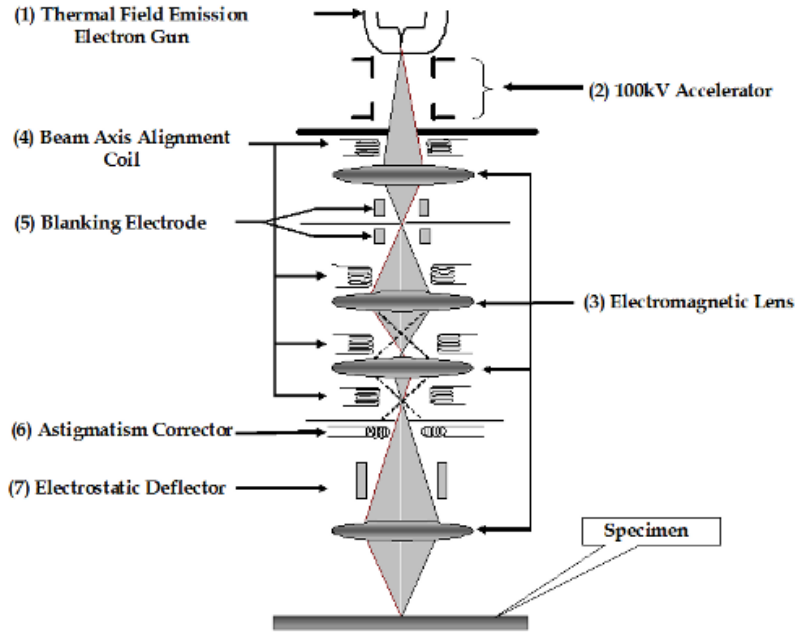

Figure 1.7 A schematic diagram for a high energy e-beam lithography system[36]

1.3 **Resist**

The resist is one of the most important materials used in lithography and is present and essential during exposure, development and etching processes. It is central in determining the quality of the final pattern produced on the substrate.

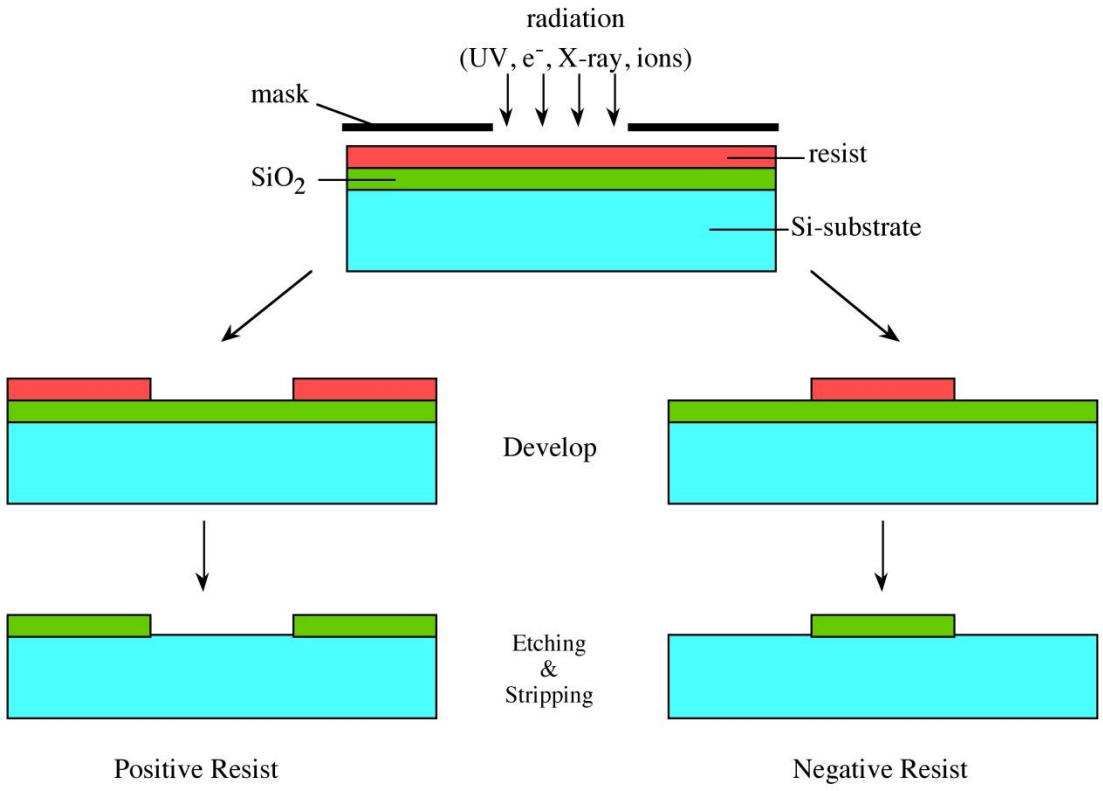

Figure 1.8 Positive tone and negative tone lithographic resists.[37]

Lithographic resists can be grouped into two categories based on observed changes in solubility of the resist after exposure, positive resists

and negative resists, as is shown in **Figure 1.8**. For positive resists, the exposed part becomes insoluble to its development solution, and thus remains on the surface, while the unexposed part is soluble and is washed away in the development solution. The negative resists acts exactly the opposite way. However, whether a resist is positive or negative is not entirely determined by the resist itself. A proper selection of development solutions sometimes can make the same resist either positive tone and negative tone, just by immersing it in different development solutions.

After reviewing the history of resist development, negative resists were prevalent at the early stage of microfabrication due to their increased adhesion to silicon and their lower cost. Nevertheless, with the requirement of fabricating smaller features, positive resists came into dominance with better resolution, generally speaking, and with less pin-hole production. The solvent swelling and image distortion during the development process may lead to poor resolution for negative resists.

From another perspective, resists can also be categorized into organic resists and inorganic resists based on its composition (although hybrid organic-inorganic resists also exist).

1.3.1 Organic resists

Organic resists, as its name suggested, are resists mainly comprised of organic polymers such as poly(methyl methacrylate) (PMMA), poly(methyl glutarimide) (PGMI), polydimethylsiloxane (PDMS) or other polymers. Organic resists have been investigated and developed for decades and are now the dominant resist used in photolithography. One of the most important reasons for this prevalence is their relatively low cost, since most organic resists are synthesized from inexpensive raw materials and deposited with solution processed approaches such as spin coating, dip coating and spraying. Moreover, benefiting from the development of synthetic polymer techniques for many other applications, organic resists, especially polymer resists, show great versatility, which enables trouble-free customization. For example, polymer resists can be chemically modified with different organic ligands on their branched chains, while maintaining the backbone unchanged, to intentionally change the solubility in the development solution, for example to switch between positive tone and negative tone response.

A brief look at the history of organic resist development shows that a few resists have received extensive attention.

1.3.1.1 DNQ-Novolak Resists

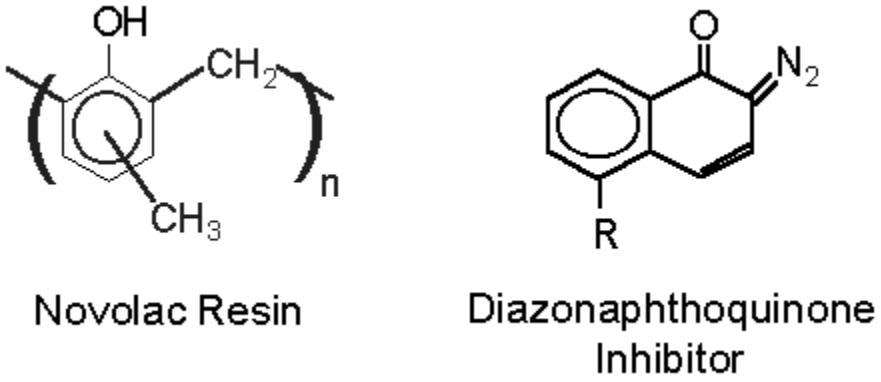

Figure 1.9 Chemical structure of a Novolac resin and a DNQ molecule[38].

Absorbing light with a wavelength between 300 nm and 450 nm, DNQ-Novolak serves as one of the most successfully commercialized and extensively used i-line and g-line resists. The DNQ-Novolak[39] resist usually contains three components: a Novolak resin, a photosensitive diazonaphthoquinone dissolution inhibitor, and an organic casting solvent (**Figure 1.9**). Later, in order to improve its thickness uniformity, a leveling agent[40] was added into its final ingredients.

Due to the acidity of the phenolic O-H group in the backbone chain, the pure Novolak resin is soluble in basic solutions such as NaOH, KOH, and tetramethylammonium hydroxide (TMAH) based aqueous solutions. However, the DNQ molecules dispersed inside the Novolak resin are themselves insoluble in basic solutions. Therefore, a higher percentage of DNQ in the Novolak resin will lead to lower solubility in basic solutions. Generally, the commercial DNQ-Novolak resists contain a sufficiently high concentration of DNQ molecules to result in an extreme low solubility in basic solutions. On the other hand, DNQ is a photo sensitive molecule which can be decomposed along the path suggested in **Figure 1.10**. Obtaining the energy given by heat or photons, a short lifetime keto-carbene will be produced, which will be further transformed into a ketene molecule via rearrangement. Therefore, after exposure, the unexposed portion is still the original DNQ embedded Novolak resin, while the exposed portion will become a ketene dispersed resin. Then if we immerse the resist into basic solution, such as TMAH, the unexposed part will be insoluble, thus remaining on the surface. However, in the exposed and ketene-contained resin, ketene molecules will react with water and produce the indene-carboxylic acid, which will dissolve in the development solution.

Finally, one can achieve a patterned resist on the surface according to the radiation chemistry mechanism proposed above.

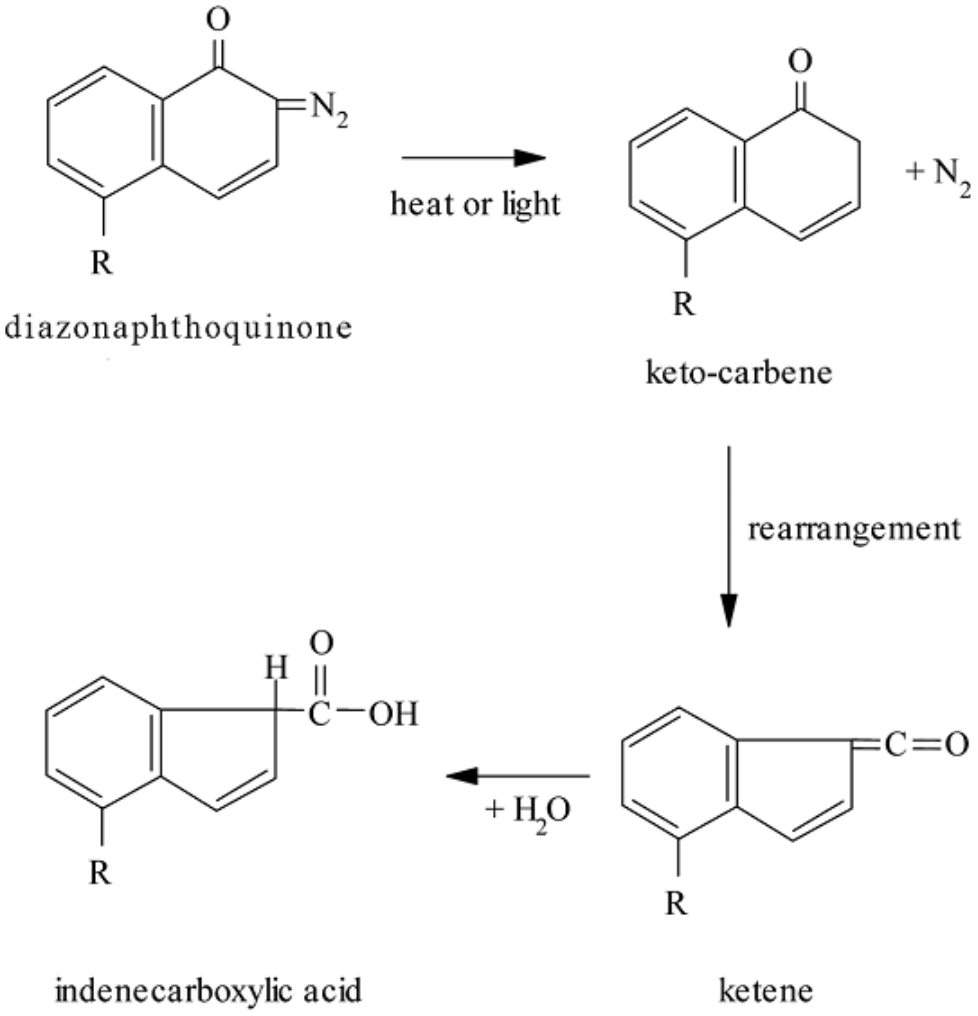

Figure 1.10 The decomposition path of the DNQ initiated by heat or photons[5]

One of the biggest disadvantages of DNQ-Novolak resists is the production of nitrogen, especially with intense photon exposure or very sensitive DNQ inhibitors. The produced nitrogen may diffuse and form bubbles inside the resists leading to a decreased film quality and even a delamination problem.

1.3.1.2 Chemical Amplification Resists (CAR)

With continuous scaling of microelectronic feature size, the traditional DNQ-Novolak resists lost their utility in DUV (deep UV) lithography due to very high photon absorption of Novolak resins leaving the bottom of the resists unreachable by incident light. To solve this problem, DUV transparent polymers (e.g. methacrylate, poly(hydroxystyrene) (PHOST)) were adopted. However, problems were not been perfectly solved; the DUV transparent polymer replacement suffers from low sensitivity. Therefore, a major new development in resists was needed to adapt to the higher energy photons and new DUV lithography processes. A key solution was the invention of chemical amplification resists (CAR) by IBM in early 1980s[41].

Since then, hundreds of CARs have been invented and developed to be used for different applications. Reviewing the CAR family, we can extract three common essential components: a matrix resin, a photoacid generator (PAG), and a dissolution inhibitor. In the matrix resin, the backbone polymer with hydrophilic groups (e.g. –OH, -COOH) usually is soluble in its development solution. However, the branches of the backbone polymer, known as protection groups in CAR, are designed to bond with bulky hydrophobic groups (e.g. tertiary-butoxycarbonyl, t-BOC[42]) to prevent the dissolution of the whole matrix resin playing the role of the dissolution inhibitor in the old DNQ-Novolak system. Typically, PAG molecules, such as triphenylsulfonium triflate (TPST) and diphenyliodonium nitrate (DPIN), are capable of photolysis, producing acid cations during the photon or electron exposure. After the exposure, a post-exposure bake is often required to facilitate the diffusion of acid cations and the cleavage of protection groups from the backbone polymer as indicated in **Figure 1.11**. Because each photon can release one or multiple catalytic acid cations, each of which can react with multiple protection groups, these resists have the ability of chemical amplification, boosting the resist sensitivity by orders of magnitude.

Although CAR-based resists benefit from chemical amplification, diffusion of released acid cations limits resolution. It is the diffusion diameter of the acid cations in the polymer that determines the final resolution when fabricating small features.

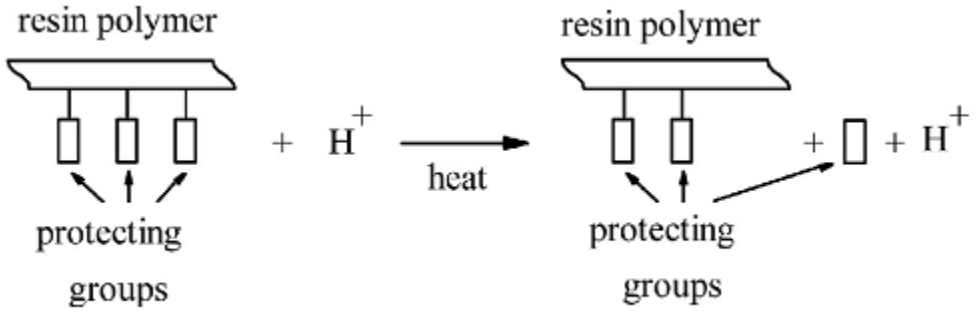

Figure 1.11 A typical reaction during the post-exposure bake of chemical amplification resists[5]

1.3.2 Inorganic Resists

Although organic resists dominate current generation microlithography in industry, the development of the inorganic resists has recently accelerated due to the potential of high resolution and low feature roughness. Different from most organic resists, which employ bulky polymers with a somewhat large radius of gyration as building blocks, the

smallest units of inorganic resists can be composed of clusters or nanoparticles with 1-20 metal atoms, having a size from 5-20 Angstroms across. The inorganic cluster to gel to insoluble solid reaction cascade is thought to occur without chemical amplification of the key steps, as occurs with the best CARs. Most inorganic resists are likely free of the resolution degrading and line edge roughing effect caused by amplification and diffusion of the catalytic acid cations. On the other hand, the drawbacks of inorganic resists are the relatively low sensitivity, essential in high throughput high volume manufacturing, and the high-dose damage to resists and substrates.

In the early stages of their development, most inorganic resists (e.g. the Ag_2S/As_2S_3 and Ge-Se systems) were deposited with expensive and time-consuming vacuum methods, such as thermal evaporation, sputtering, and e-beam deposition. To compete with inexpensive solution-processed organic resists, more recent investigations have focused on novel inorganic resists deposited by solution methods such as spin-coating.

The most well-known solution-deposited inorganic resist is hydrogen silsesquioxane (HSQ); its monomeric structure is shown in **Figure 1.12 (a)**.

Prepared by spin-coating and soft baking, HSQ has demonstrated the capability of patterning sub 5 nm half-pitch features.[43] Furthermore, it shows high mechanical stability, great etch resistance, and a relative ease of pattern-transfer to various substrates.

During electron or photon exposure, HSQ is proposed to undergo a cross-linking mechanism changing from soluble monomeric cage structures (**Figure 1.12 (a)**) to the insoluble cross-linked network structure (**Figure 1.12 (b)**), which makes HSQ a negative tone resist. With respect to the detailed radiation chemistry, Namatsu, *et al.*[44] proposed a three-step radical-catalyzed mechanism for e-beam exposure as shown below:

$$2HSiO_{3/2}\,(\text{cage}) + e^- \rightarrow 2Si\cdot + H_2 \quad (1)$$

$$2Si\cdot + 2H_2O \rightarrow 2SiOH + H_2 \quad (2)$$

$$2SiOH \rightarrow 2SiO_{1/2}\,(\text{network}) + H_2O \quad (3)$$

In the first step, the H-terminated cage structure monomer ($HSiO_{3/2}$) absorbed electrons to break the Si-H bonds followed by the production of Si radical sites and hydrogen. Since water is usually used as the solvent of HSQ precursor solutions and the pre-exposure soft baking cannot completely

remove all the water, the highly reactive Si radical sites further react with water and form new Si-OH bonds in the second step. Finally, two neighboring Si-OH bonds likely react with each other and dehydrate forming Si-O-Si bonds that cross-link monomers.

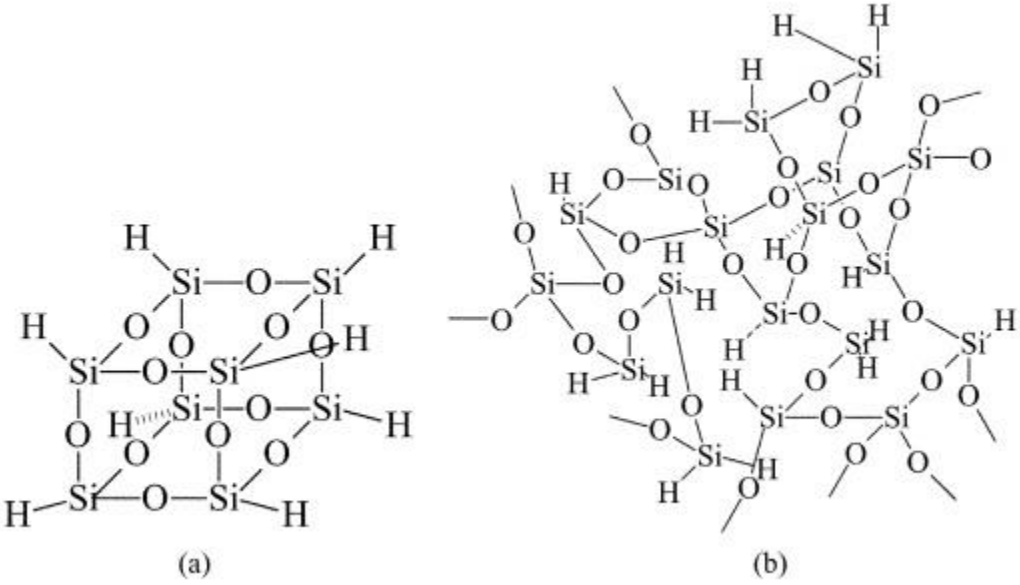

Figure 1.12 The chemical structure of (a) the cage HSQ monomer, and (b) the networked form after exposure[45]

In spite of their high resolution and high etching resistance, HSQ resists also have the disadvantage of low sensitivity, which greatly limits their applicability in high volume manufacturing.

By combining the high sensitivity of organic resists and the high resolution/high etching resistance of inorganic resists, some approaches employing organic/inorganic hybrid resists have also been demonstrated.

Zanchetta *et al*. reported a novel hybrid resist synthesized by sol-gel methods.[46] The resist preparation begins with mixing aluminum-tri-sec-butoxide and a phenyl-modified silane precursor followed by a 100 °C soft bake for 5 min. As shown in **Figure 1.13**, aluminum-tri-sec-butoxide undergoes hydrolysis first by vigorously stirring, then followed by condensation via a soft bake, and finally producing a ready-to-use alumina-like organic-ligand-chelated resist film. Depending on the development solution used, the resist can present either with a positive or negative tone. The hybrid resist shows excellent plasma etching resistance with etching of the exposed silicon to a depth of 3 μm, starting with only a 30 nm thick resist mask, leading to an extraordinary etch selectivity of 1:100. Additionally, a 20 nm dense line pattern has also been achieved using hybrid resists by e-beam lithography.

To investigate the radiation chemistry, high resolution Fourier transform infrared spectroscopy (FTIR) was employed. By comparing the

spectra pre- and post- UV exposure, researchers found a drastic peak intensity drop of the Si-phenyl peak at 1120 cm^{-1} and the presence of new peaks of Si-O-Si at 1030-1100 cm^{-1}, and Al-O-Al (broad peaks, 500-1000 cm^{-1}). The IR peak evolution confirms a mechanism of Si-phenyl bond breaking and inorganic network formation.

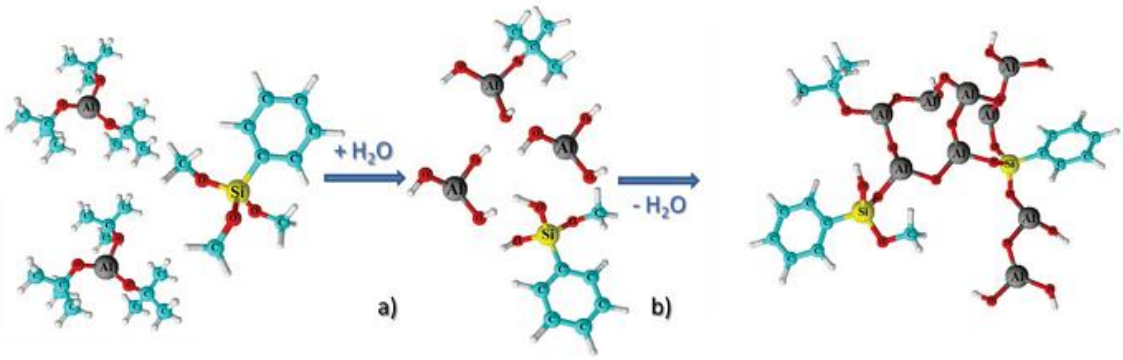

Figure 1.13 The resist chemistry change during preparation: (a) hydrolysis, and (b) condensation[46].

In summary, resists have been continuously investigated and advanced to optimize processing and performance. New exposure techniques (including photon energies) must be well-matched to the resist employed, and must be thoroughly investigated if eventually that are to be widely applied in high volume industrial production. DNQ-Novolak emerged

as the resist of choice for i-line and g-line lithography with mercury arc lamp exposure tools, then the invention and development of chemical amplification resists for DUV lithography. We will soon be producing sub-10 nm features, and EUV-based lithography, will likely become the dominant class of techniques replacing the current ones. To make this happen, the challenge of finding excellent resists that can work well with a 13.5nm EUV scanner has to be overcome.

1.4 EUVL and HafSOx resist

Lithography has advanced from i-line and g-line to the currently popular 193 nm ArF excimer laser. For the next generation lithography, the exposure wavelengths of 157nm, x-ray (0.4nm) and EUV (13.5 nm) have been proposed and studied for many years. The use of 157nm light was given up due to the emergence of immersion exposure and multi-patterning, which greatly extends the resolution limit. It has led to industry skip the moderate improvements that can be realized by moving from 193nm to 157 nm. EUV lithography was theoretically proposed and experimentally demonstrated in the late 1980s and early 1990s[47-49]. Compared with x-ray lithography, EUV lithography offers a way the extend

the optical projection method. Additionally, using 13.5 nm EUV photons, an average k (e.g. 0.4) and a large numerical aperture (e.g. 0.6) would enable a single exposure resolution limit to below the 10 nm level. Although it is currently the most promising candidate for next generation lithography, the aggressive wavelength shrinkage from 193 nm to 13.5 nm still faces many challenges.

1.4.1 EUV light source

For high energy (~92 eV) of EUV photons, many atmospheric gases, including oxygen and nitrogen, will absorb EUV light. Therefore, the entire light path, from the light source to the mask to the final wafer, should be placed inside a vacuum chamber. The basic requirements for the EUV light source include high EUV power, excellent contamination control, large collecting angle, and good thermal and radiation stability.

Synchrotron sources, explored as first EUV sources, are not practical for high volume manufacturing due to their high cost and size. The current candidates for the exposure tools are mainly discharge-produced plasma (DPP) and laser-produced plasma (LPP). The schematic of both exposure sources are shown in **Figure 1.14**.

For the DPP source, a high voltage (1-10 keV) is applied between electrodes and a low pressure gas, causing the gas to become ionized. The electron flow will make a circular magnetic field, which in turn self-constricts the current (also known as pinch effect) and finally produces a plasma that emits EUV photons.

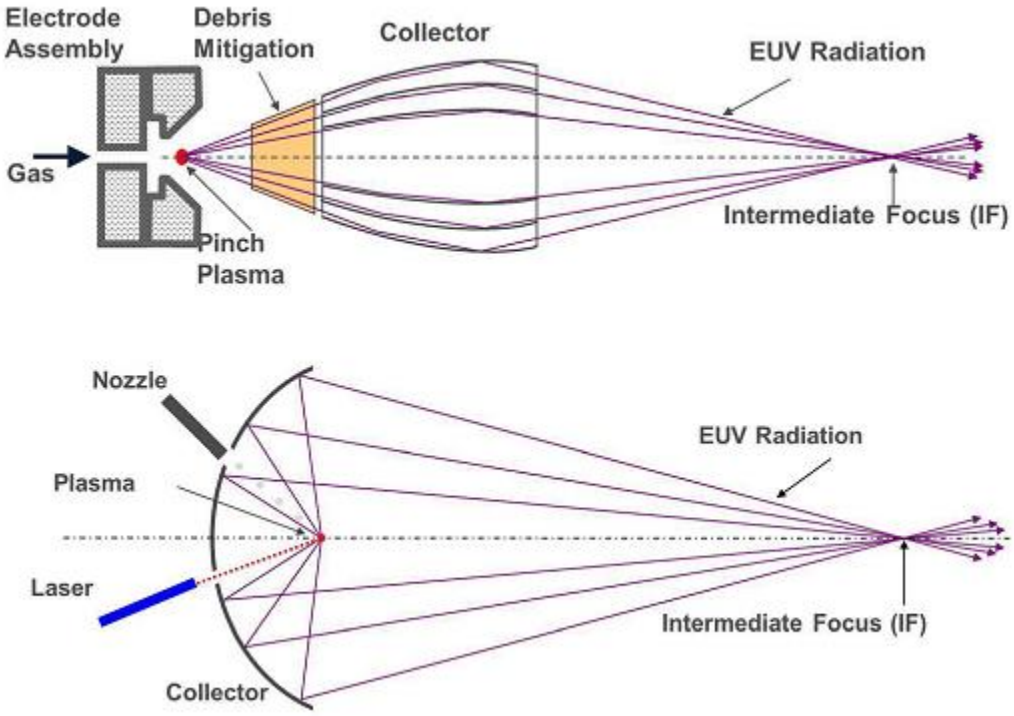

Figure 1.14 The working principle of LPP and DPP sources[50].

Compared with LPP sources, the DPP source has a higher conversion efficiency and a lower overall cost. However, as shown in the figure, the limited collecting angle and the grazing angle incidence collector greatly

restrict the maximum radiation collected at the intermediate focus (IF) point.

With LPP, a hot plasma is produced by heating the target material with a laser. According to the LPP source developed by Cymer LLC, acquired by ASML in 2013, a high power CO_2 drive laser (>10 kW) with a wavelength of 10.6 µm is employed to produce enough EUV power, factoring in a <5% conversion efficiency. A nozzle continuously supplies tin droplets (~20 µm) in order to maintain a fresh surface, greatly benefiting the plasma. Because of its advantages in power scalability, in mass-limited operation, and in enabling a normal incidence collector, the LPP source has become the most promising EUV source.

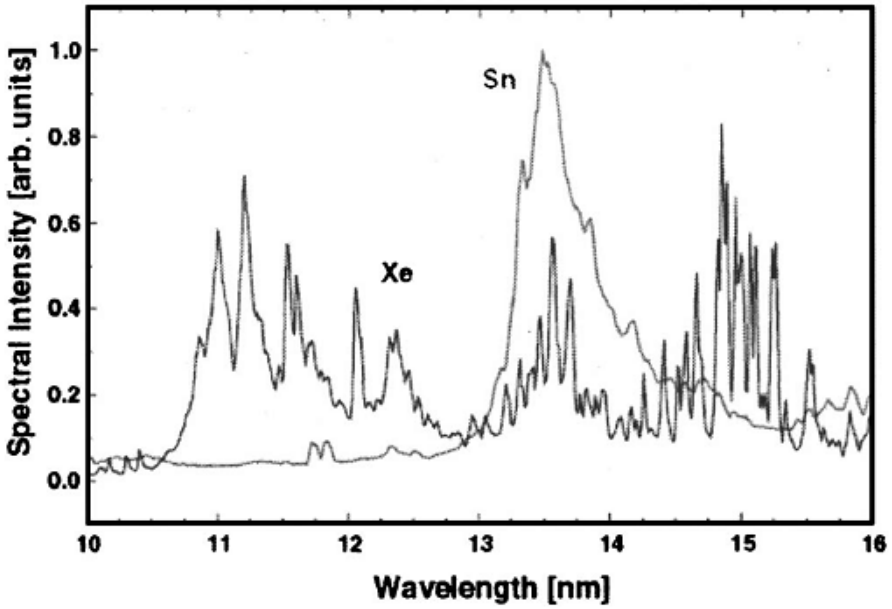

Figure 1.15 The emission spectra of plasma generated from the Sn and Xe EUV sources[51].

For the target material, high Z elements with higher electron densities, such as Xe and Sn, are the most promising candidates. However, as shown in **Figure 1.15,** Both EUV target (Xe & Sn) show emission peaks around 13.5 nm, but Xe source has significant emission around 11 nm, which limits its maximum achievable conversion efficient. Therefore, Sn currently stands as the candidate with the most potential.

In a recent configuration, Cymer LLC has demonstrated an in-house 100W source with a 3.5% conversion efficiency, driven by a 15kW CO_2 laser with a 17% overhead cost[52]. A 125W EUV source, the minimum power target for high volume manufacture, is believed to be achievable in the near future.

1.4.2 Multi-layer coating and optics

EUV lithography optics basically include both illumination mirrors and projection mirrors. The illumination mirrors collect the emitted EUV light and pass them on to the mask, thus the field uniformity is the most important parameter. On the other hand, the projection mirrors are

responsible for imaging the pattern onto the wafer, therefore requiring good control of aberration and diffraction. Because of the unique properties of EUV light absorbed by almost all materials in nature, all EUV lithography optic mirrors are coated with resonance-reflecting multi-layers. The most common structure is the multiple repeated bilayers: a high-electron density metal layer and a low-electron density spacer layer. Currently, the most popular multi-layer structure consists of 40 layers of Mo/Si.

However, even with excellent reflectivity of Mo/Si multi-layers, there is still substantial EUV light absorbed by the mirrors, causing heating. With heating, the bilayer thickness changes, inter-diffusion between bilayers is enhances, and surface layer oxidation can result. Clever annealing techniques and low-energy, low-growth-rate e-beam deposition can effectively improve the thermal stability of the multilayers by reducing the intrinsic stress. To limit the inter-diffusion, a diffusion buffer layer, such as B_4C[53], is usually sandwiched in between the metal layer and the spacer layer without affecting the reflectivity too much. Finally, to prevent the scattering and reflectance degradation resulting from surface oxidation, surface capping (e.g., TiO_2[54], RuO_2[54], SiC[55]…) layers have been developed.

1.4.3 Reflective mask

A tradition transmission mask as applied in projection steppers does not work with high power EUV sources. Reflective masks, using reflective Mo/Si multilayers, have been intensively investigated and have become the main candidate.

A key current challenge is to find the best mask substrate with a low coefficient of thermal expansion (CTE) to minimize EUV absorption and heating degradation and instabilities. Instead of using pure fused silica, fused silica with 7%-9% Ti doping[56] has been developed as it has a CTE of ~30 ppb/K , compared with 500 ppb/K for pure fused silica.

Another challenge is defect control. For the multilayer mask, two classes of defects determine the image quality transferred from the mask to the final wafer: the phase defects and the amplitude defects. For EUV lithography below 22nm node fabrication, a strict control of defects is required. The amplitude defects are defects/particles on the surface of the multilayers and are usually repairable. Phase defects, resulting in a phase change of the reflected wave, usually are buried inside the multilayers and even a small size defect can present as new printed features on wafers.

Therefore, the approaches to defect analysis, including defect detection and printability, have become one of the most critical issues in EUV lithography mask fabrication.

1.4.4 Resists

Much research has gone into finding the best EUV resist since the first demonstration of EUV lithography 25 years ago. The resists must demonstrate excellent performance in resolution, sensitivity, line edge roughness (LER), outgas control, etch resistance, and so forth. Moreover, due to strong EUV absorption, a thinner resist film is preferred enabling the EUV photons to pass through and fully expose the film. An ability to demonstrate a high aspect ratio and prevent pattern collapse with thin films is another key criterion for a good EUV resist.

1.4.4.1 Chemically amplified resist

Chemically amplified resists (CARs), adopted from current 193 nm exposure tools, have become one of the earliest developed EUV resists. Benefited from the loading of photo-acid generators (PAGs), high sensitivity has been achieved. More importantly, the sensitivity of resists determines the minimum power required by the EUV source.

However, the CARs are not without disadvantages. Two of the biggest challenges of CARs are outgassing and LER issues. The resist outgassing during exposure, originating mostly from PAG radiation chemistry, becomes an even more important problem since the whole EUV light-path is placed in a vacuum chamber. Nevertheless, the methods used to limit outgassing have to sacrifice the resist sensitivity because for a PAG, higher sensitivity usually means more outgassing. Therefore, a compromise between sensitivity and outgassing has to be made for the CARs. The LER problem results from various factors such as the polymer molecular size and the diffusion of photo-acids. Even now most PAG groups are directly chemically bonded to the backbone polymer aiming to mitigate the diffusion of photo-acids. In reality, this problem is still extremely hard to control. Additionally, the nature of polymers used in CARS is an obstacle to achieve better LER; it has proven difficult to make sufficient improvements to make current generation CARs the resist of choice.

1.4.4.2 MSOx inorganic resists

Compared with conventional CARs, inorganic resists are known for high resolution and low LER, such as HSQ, as discussed above. As the device

size keeps shrinking, soon below the 10 nm level, and LER becomes one of the most critical parameters for a EUV resist, more and more attention starts shifting to inorganic resists. Metal oxide sulfates (MSOx), as E-beam lithographic resists, were firstly reported by Jason Stowers, *et al* in 2008[57], in which the hafnium and zirconium oxide sulfates, called HafSOx and ZircSOx respectively, were investigated. Both films were deposited with solution-process methods and the H_2O_2 solution was added to act as the electron sensitive moiety. An SEM writing system with a 30 keV electron gun was employed as the initial exposure tool. Post-exposure films were developed in a tetramethylammonium hydroxide (TMAH) solution.

By varying the metal-to-sulfate ratio, an isolated 15-nm line and 36-nm dense lines were achieved with extremely low LERs, 1.9 nm and 2.1 nm respectively, which outperformed most of CARs and even low-LER HSQ resists. With regard to sensitivity, a turn-on dose below 10 μC/cm^2 was obtained for both HafSOx and ZircSOx with moderate contrasts. This closely matches the sensitivity level of CARs and exceeds most inorganic films including HSQ. In terms of EUV photo-absorption cross section, Hf has an order of magnitude higher EUV absorption (4.3E6 cm^2/mol) than C (3.5 x

10^5 cm^2/mol), which is the most abundant element in organic CARs, thus implying a higher sensitivity.

MSOx resists soon revealed high resolution and moderate sensitivity for various lithographic techniques. MSOx resists have begun to be actively investigated over the past 7 years as EUV resists due to their strong variability, including modifying metal-sulfate ratios, replacing the metal species, adding new radiation sensitive species, and changing the metal/cluster bridging groups.

1.4.4.3 Tin based inorganic resists

With high EUV absorption, tin based inorganic resists have been receiving much attention recently. The design concept usually includes two parts: an inorganic tin-oxo cluster[58] (or simply Sn atoms[59]), and organic photon/electron sensitive ligands[58, 59]. Benefiting from the small size of tin moieties and a non-chemical amplification mechanism, the tin based resist demonstrated very high resolution (e.g. 16 nm dense-line patterns) and low LERs (1.4 nm and 1.1 nm). Although tin has a naturally high EUV absorption, the films only showed moderate EUV sensitivity (e.g. 50-600 mJ/cm^2). More studies and chemistries are needed to improve the tin resist sensitivity.

In the following chapters, I'll first briefly introduce the main characterization methods I used in the thesis in Chapter 2. In Chapter 3, the HafSOx film composition would be probed with various techniques. In Chapter 4, XPS, coupled with other methods, would be chosen to shed lights on the radiation chemistry happened in the film with exposure. Chapter 5 illustrates results from the low energy electrons exposure experiments to help us achieve a better understanding on the role of low energy secondary electrons in EUV exposure. Finally, we discussed the patterning results we achieved with helium ion beam lithography in Chapter 6.

References

1. Moore, G. E., Cramming more components onto integrated circuits (Reprinted from Electronics, pg 114-117, April 19, 1965). *Proceedings of the Ieee* **1998,** 86, (1), 82-85.
2. Shuler, K. Moore's Law is Dead: Long Live SoC Designers. http://info.arteris.com/blog/moores-law-is-dead-long-live-soc-designers
3. Jaeger, R. C., *Introduction to microelectronic fabrication*. 2nd ed.; Prentice Hall: Upper Saddle River, N.J., 2002; p xiv, 316 p.
4. May, G. S.; Spanos, C. J., *Fundamentals of semiconductor manufacturing and process control*. IEEE ;

Wiley-Interscience: Piscataway

Hoboken, N.J., 2006; p xix, 463 p.
5. Levinson, H. J., Principles of lithography. In *Press monograph 198*, 3rd ed.; SPIE Press,: Bellingham, Wash., 2010; pp 1 online resource (xiv, 503 pages).
6. Bucknall, D. G., Nanolithography and patterning techniques in microelectronics. In *Woodhead Publishing in materials*, Woodhead Pub. ;

CRC Press,: Cambridge

Boca Raton, FL, 2005; pp 1 online resource (xiv, 409 p.).
7. Chou, S. Y.; Krauss, P. R.; Renstrom, P. J., Nanoimprint lithography. *Journal of Vacuum Science & Technology B* **1996,** 14, (6), 4129-4133.
8. Xia, Q. F.; Pease, R. F., Nanoimprint lithography 20 years on. *Nanotechnology* **2015,** 26, (18).
9. Srituravanich, W.; Fang, N.; Sun, C.; Luo, Q.; Zhang, X., Plasmonic nanolithography. *Nano Letters* **2004,** 4, (6), 1085-1088.
10. Kim, Y.; Kim, S.; Jung, H.; Lee, E.; Hahn, J. W., Plasmonic nano lithography with a high scan speed contact probe. *Optics Express* **2009,** 17, (22), 19476-19485.
11. Pan, L.; Park, Y.; Xiong, Y.; Ulin-Avila, E.; Wang, Y.; Zeng, L.; Xiong, S. M.; Rho, J.; Sun, C.; Bogy, D. B.; Zhang, X., Maskless Plasmonic Lithography at 22 nm Resolution. *Scientific Reports* **2011,** 1.
12. Kim, S. O.; Solak, H. H.; Stoykovich, M. P.; Ferrier, N. J.; de Pablo, J. J.; Nealey, P. F., Epitaxial self-assembly of block copolymers on lithographically defined nanopatterned substrates. *Nature* **2003,** 424, (6947), 411-414.
13. Jeong, S. J.; Kim, J. Y.; Kim, B. H.; Moon, H. S.; Kim, S. O., Directed self-assembly of block copolymers for next generation nanolithography. *Materials Today* **2013,** 16, (12), 468-476.
14. Kim, B. H.; Shin, D. O.; Jeong, S. J.; Koo, C. M.; Jeon, S. C.; Hwang, W. J.; Lee, S.; Lee, M. G.; Kim, S. O., Hierarchical self-assembly of block copolymers for lithography-free nanopatterning. *Advanced Materials* **2008,** 20, (12), 2303-+.
15. Alphonse-Louis Poitevin. http://www.getty.edu/art/collection/artists/1913/alphonse-louis-poitevin-french-1819-1882/
16. Levenson, M. D., Wave-Front Engineering for Photolithography. *Physics Today* **1993,** 46, (7), 28-36.

17. Borkar, S., Microarchitecture and Design Challenges for Gigascale Integration. In *Proceedings of the 37th annual IEEE/ACM International Symposium on Microarchitecture*, IEEE Computer Society: Portland, Oregon, 2004; pp 3-3.
18. Sansonetti, C. J.; Salit, M. L.; Reader, J., Wavelengths of spectral lines in mercury pencil lamps. *Applied Optics* **1996,** 35, (1), 74-77.
19. Besaucele, H.; Das, P.; Duffey, T.; Embree, T.; Ershov, A.; Fleurov, V.; Grove, S.; Melcher, P.; Ness, R.; Padmadandu, G. G., A comparison of ArF and KrF laser performance at 2kHz for microlithography. *Optical Microlithography Xiii, Pts 1 and 2* **2000,** 4000, 1476-1480.
20. Rothschild, M.; Goodman, R. B.; Hartney, M. A.; Horn, M. W.; Kunz, R. R.; Sedlacek, J. H. C.; Shaver, D. C., Photolithography at 193 Nm. *Journal of Vacuum Science & Technology B* **1992,** 10, (6), 2989-2996.
21. Sandstrom, R., Argon Fluoride Excimer Laser Source for Sub-0.25 Mm Optical Lithography. *Optical/Laser Microlithography Iv* **1991,** 1463, 610-616.
22. Ryan, D.; Parviz, B. A.; Linder, V.; Semetey, V.; Sia, S. K.; Su, J.; Mrksich, M.; Whitesides, G. M., Patterning multiple aligned self-assembled monolayers using light. *Langmuir* **2004,** 20, (21), 9080-9088.
23. French, R. H.; Tran, H. V., Immersion Lithography: Photomask and Wafer-Level Materials. *Annual Review of Materials Research* **2009,** 39, 93-126.
24. Flagello, D. G.; Renwick, S. P., Evolving Optical Lithography without EUV. *Optical Microlithography Xxviii* **2015,** 9426.
25. Singer, P., Lithography: What are the alternatives to EUV? Hopes remain high for EUV, but long delays has caused attention to shift to various alternatives. *Solid State Technology* **2014,** 57, (6), 14-17.
26. Tallents, G.; Wagenaars, E.; Pert, G., OPTICAL LITHOGRAPHY Lithography at EUV wavelengths. *Nature Photonics* **2010,** 4, (12), 809-811.
27. Hruska, J. TSMC announces lithography milestone as EUV moves closer to production. http://www.extremetech.com/computing/199782-tmsc-announces-lithography-milestone-as-euv-moves-closer-to-production
28. Manfrinato, V. R.; Zhang, L. H.; Su, D.; Duan, H. G.; Hobbs, R. G.; Stach, E. A.; Berggren, K. K., Resolution Limits of Electron-Beam Lithography toward the Atomic Scale. *Nano Letters* **2013,** 13, (4), 1555-1558.
29. Vieu, C.; Carcenac, F.; Pepin, A.; Chen, Y.; Mejias, M.; Lebib, A.; Manin-Ferlazzo, L.; Couraud, L.; Launois, H., Electron beam lithography: resolution limits and applications. *Applied Surface Science* **2000,** 164, 111-117.
30. Hohn, F. J., Electron-Beam Lithography - Its Applications. *Journal of Vacuum Science & Technology B* **1989,** 7, (6), 1405-1411.
31. Chen, Y. F., Nanofabrication by electron beam lithography and its applications: A review. *Microelectronic Engineering* **2015,** 135, 57-72.
32. Broers, A., Some experimental and estimated characteristics of the lanthanum hexaboride rod cathode electron gun. *Journal of Physics E: Scientific Instruments* **1969,** 2, (3), 273.
33. Ahmed, H.; Broers, A., Lanthanum hexaboride electron emitter. *Journal of Applied Physics* **1972,** 43, (5), 2185-2192.
34. Fukuhara, S.; Todokoro, H.; Sakitani, Y., Field emission electron gun. In Google Patents: 1981.
35. Parker, N. W.; Brodie, A. D.; McCoy, J. H., A high throughput NGL electron beam direct-write lithography system. *Emerging Lithographic Technologies Iv* **2000,** 3997, 713-720.

36. Wu, C. S.; Makiuchi, Y.; Chen, C., *High-energy Electron Beam Lithography for Nanoscale Fabrication*. 2010.
37. Barron, A. R. Composition and Photochemical Mechanisms of Photoresists. http://cnx.org/contents/2997481b-ecd7-4e38-9465-677d8adbe0ad@2/Composition-and-Photochemical-#id2321669
38. Henderson, C. L., Introduction to DNQ-Novolac Resists.
39. Dammel, R., *Diazonaphthoquinone-based resists*. SPIE Optical Engineering Press: Bellingham, Wash., USA, 1993; p 203 p.
40. Frasch, P.; Saremski, K. H., Feature Size Control in Ic Manufacturing. *Ibm Journal of Research and Development* **1982,** 26, (5), 561-567.
41. Ito, H.; Willson, C. G.; Frechet, J. H. In *New UV resists with negative or positive tone*, 1982 Symposium on VLSI Technology. Digest of Technical Papers, 1982; 1982; pp 86-87.
42. Ito, H., Chemical amplification resists: History and development within IBM. *IBM Journal of Research & Development* **2000,** 44, (1/2), 12p.
43. Yang, J. K. W.; Cord, B.; Duan, H. G.; Berggren, K. K.; Klingfus, J.; Nam, S. W.; Kim, K. B.; Rooks, M. J., Understanding of hydrogen silsesquioxane electron resist for sub-5-nm-half-pitch lithography. *Journal of Vacuum Science & Technology B* **2009,** 27, (6), 2622-2627.
44. Namatsu, H.; Takahashi, Y.; Yamazaki, K.; Yamaguchi, T.; Nagase, M.; Kurihara, K., Three-dimensional siloxane resist for the formation of nanopatterns with minimum linewidth fluctuations. *Journal of Vacuum Science & Technology B* **1998,** 16, (1), 69-76.
45. Yang, C. C.; Chen, W. C., The structures and properties of hydrogen silsesquioxane (HSQ) films produced by thermal curing. *Journal of Materials Chemistry* **2002,** 12, (4), 1138-1141.
46. Zanchetta, E.; Della Giustina, G.; Grenci, G.; Pozzato, A.; Tormen, M.; Brusatin, G., Novel Hybrid Organic-Inorganic Spin-on Resist for Electron- or Photon-Based Nanolithography with Outstanding Resistance to Dry Etching (vol 25, pg 6261, 2013). *Advanced Materials* **2014,** 26, (5), 674-674.
47. Bjorkholm, J. E.; Bokor, J.; Eichner, L.; Freeman, R. R.; Gregus, J.; Jewell, T. E.; Mansfield, W. M.; Mac Dowell, A. A.; Raab, E. L.; Silfvast, W. T.; Szeto, L. H.; Tennant, D. M.; Waskiewicz, W. K.; White, D. L.; Windt, D. L.; Wood, O. R.; Bruning, J. H., Reduction imaging at 14 nm using multilayer ‐ coated optics: Printing of features smaller than 0.1 μm. *Journal of Vacuum Science & Technology B* **1990,** 8, (6), 1509-1513.
48. Kinoshita, H.; Kurihara, K.; Ishii, Y.; Torii, Y., Soft x ‐ ray reduction lithography using multilayer mirrors. *Journal of Vacuum Science & Technology B* **1989,** 7, (6), 1648-1651.
49. Hawryluk, A. M.; Seppala, L. G., Soft x ‐ ray projection lithography using an x ‐ ray reduction camera. *Journal of Vacuum Science & Technology B* **1988,** 6, (6), 2162-2166.
50. Wu, B. Q.; Kumar, A., Extreme ultraviolet lithography and three dimensional integrated circuit-A review. *Applied Physics Reviews* **2014,** 1, (1).
51. Wua, B. Q.; Kumar, A., Extreme ultraviolet lithography: A review. *Journal of Vacuum Science & Technology B* **2007,** 25, (6), 1743-1761.
52. Bakshi, V. 2015 SPIE Advanced Lithography EUVL Conference – Summary and Analysis. http://electroiq.com/euvl-focus/2015/03/10/2015-spie-advanced-lithography-euvl-conference-summary-and-analysis/
53. Bajt, S.; Alameda, J. B.; Barbee, T. W.; Clift, W. M.; Folta, J. A.; Kaufmann, B.; Spiller, E. A., Improved reflectance and stability of Mo-Si multilayers. *Optical Engineering* **2002,** 41, (8), 1797-1804.
54. Yulin, S.; Benoit, N.; Feigl, T.; Kaiser, N.; Fang, M.; Chandhok, M., Mo/Si multilayers with enhanced TiO(2)- and RuO(2)-capping layers. *Emerging Lithographic Technologies Xii, Pts 1 and 2* **2008,** 6921.

55. Wang, F. L.; Liu, L.; Li, W. B.; Zhu, J. T.; Zhang, Z.; Wang, Z. S.; Chen, L. Y., Design of the chirped Mo/Si multilayer mirror with SiC capping layer in extreme ultraviolet region. *Optik* **2012,** 123, (24), 2222-2225.
56. JohnKadaksham, A.; Teki, R.; Godwin, M.; House, M.; Goodwin, F., Low Thermal Expansion Material (LTEM) Cleaning and Optimization for Extreme Ultraviolet (EUV) Blank Deposition. *Extreme Ultraviolet (Euv) Lithography Iv* **2013,** 8679.
57. Stowers, J.; Keszler, D. A., High resolution, high sensitivity inorganic resists. *Microelectronic Engineering* **2009,** 86, (4-6), 730-733.
58. Cardineau, B.; Del Re, R.; Al-Mashat, H.; Marnell, M.; Vockenhuber, M.; Ekinci, Y.; Sarma, C.; Neisser, M.; Freedman, D. A.; Brainard, R. L., EUV Resists based on Tin-Oxo Clusters. *Advances in Patterning Materials and Processes Xxxi* **2014,** 9051.
59. Del Re, R.; Sortland, M.; Passarelli, J.; Cardineau, B.; Ekinci, Y.; Vockenhuber, M.; Neisser, M.; Freedman, D. A.; Brainard, R. L., Low-LER Tin Carboxylate Photoresists using EUV. *Extreme Ultraviolet (Euv) Lithography Vi* **2015,** 9422.

Chapter 2 : Characterization methods

2.1 X-ray Photoelectron Spectroscopy (XPS)

X-ray photoelectron spectroscopy (XPS) is a materials characterization technique that qualitatively and quantitatively investigates near surface chemical composition. As shown in **Figure 2.1**, high energy x-rays impinge upon a material, and excite and emit core electrons. Some fraction of the photoemitted electrons escapes from the surface of a sample and a smaller fraction are collected by the detector. Based on the intensity and kinetic energies of the collected electrons, compositional information and oxidation states of elements can be determined. In the example in **Figure 2.1**, the Cu 2s, 2p, 3s, and 3p electrons are identified based on their kinetic energies. Some outer-shell electrons can fill the vacancies left by the electrons knocked out by x-rays, and pass their energies to the adjacent electrons. This results in electron emission, also known as Auger electrons. In this case, Cu Auger electrons were also found in the spectrum.

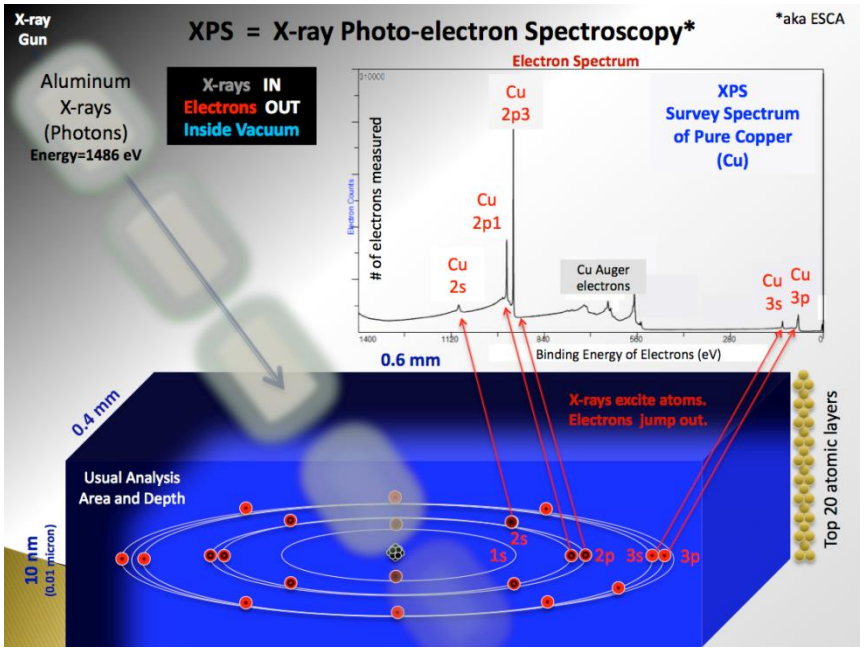

Figure 2.1 The working principle of XPS exampling with a pure Cu sample[1]

The central parts of an XPS system include an ultra-high-vacuum (UHV) chamber, an x-ray source, an electron energy analyzer, and an electron detector. Magnesium and aluminum are the two main anode targets usually used in commercial x-ray sources, emitting peak energies of 1253 eV and 1486.7 eV respectively. The old fashion twin anode non-monochromatic x-ray source includes both anode targets enabling the selection of either x-ray energy; it also incorporates a thin Al window which allows x-rays, but not electrons or lower energy photons (e.g. visible), to pass through. To obtain a narrower energy distribution, the monochromatic

x-ray source was developed with Al anode targets and a crystal quartz disc to constructively interfere with the 1486.7 eV photons. As for the electron energy analyzer, early generation cylinder mirror analyzer (CMA) was comprised of two co-axial cylinders applied with a potential difference. This allows only electrons with a certain energy to pass through, but it had poor energy resolution. Currently preferred structures of analyzers are hemisphere electron energy analyzers in which two concentric hemispheres are employed, instead of cylinders; leading to improved energy resolution.

Although the kinetic energy of an electron is detected, the binding energy (BE) is usually used to define peak position in a XPS spectrum to help compare between different systems. The calculation of BE is based on the equation below:

$$E_{BE} = E_{xray} - E_{kinetic} - \phi spec,$$

where E_{BE} and $E_{kinetic}$ are the binding energy and detected kinetic energy, respectively, E_{xray} is the energy of an x-ray photon, and ϕ_{spec} is the effective work function of the electron spectrometer. The BE determination becomes more complicated when dealing with low electron conductivity samples due to trapped charges. This will build up a static electric field on

the surface after the electron leaves, and shift the energy of the photoelectrons on their way to the detector. To compensate for trapped charges, a low energy electron flood gun is a popular choice. Another option is to calibrate the BE after one obtains the XPS spectra. One widely used method is to calibrate based on “adventitious” carbon, whose 1s peak is located at 248.8 eV (adventitious refers to carbon randomly adsorbed from background gasses, either in the ambient atmosphere, or in the vacuum system). Another popular way to reference the sample XPS energies is to introduce the chemically inert gold onto the substrate during measurement to then calibrate other peaks based on the Au 4f 7/2 at 84.0 eV.

Because of the relatively low mean free path of low energy electrons (5-1000eV), only electrons within a certain depth can escape from the surface and be collected by the detector. For most elements, the XPS detection limit on the vertical direction is around 5-10 nm (~20 atomic layers). To probe deeper inside the sample, destructive depth profiling methods[2, 3] are widely used. The dominate depth profile technique enables a layer-by-layer XPS measurement by using Ar sputtering to etch away layers with close to atomic thickness etching control. This enables XPS to

detect the composition layer by layer. To probe a deeper layer, just continue to etch and probe. One of several problems with this method is the preferential sputtering of different elements, resulting in film compositional changes during sputtering. To reduce this effect, a mild sputtering condition (e.g. low energy and low current) is recommended.

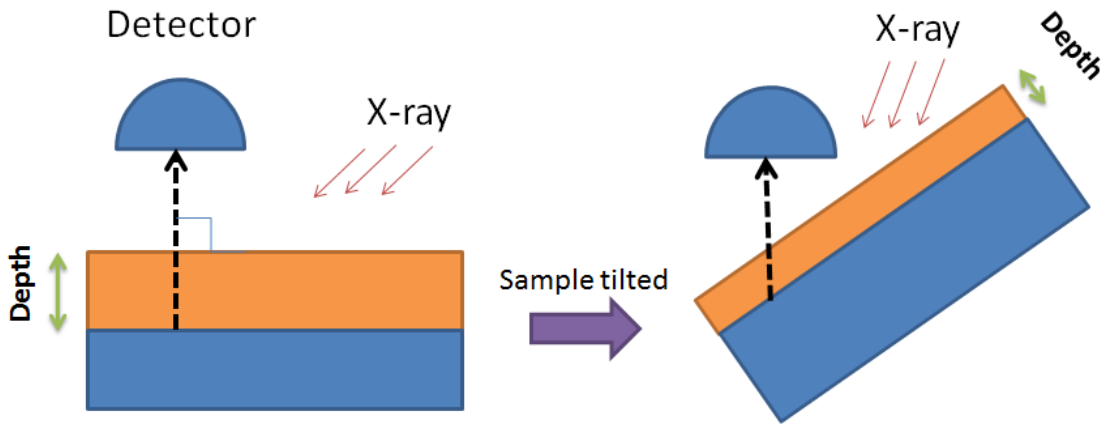

Figure 2.2 The principle of angle resolved XPS

Instead of probing the bulk using depth profile techniques, sometimes only the near surface region is of interest. In this case, another XPS technique called angle resolved XPS (**Figure 2.2**) is helpful. For normal angle emission relative to the surface, the escape depth that can be accurately detected with sufficient signal to noise is about 3 times the electron inelastic mean free path λ. However, when the sample is tilted

with an angle θ, the escape depth becomes cos θ of the original depth. When photoelectrons are detected with a much more glancing angle to the surface normal, only the material closest to the surface is probed. By carefully taking spectra as a function of emission angle, the spectra can be modeled in a manner that produces a depth profile[4].

2.2 Rutherford Backscattering Spectrometry (RBS)

Rutherford backscattering spectrometry (RBS), named after the well-known Rutherford gold foil experiment, is an analytical technique which can determine atomic mass and elemental concentration versus depth. In RBS, a beam of high energy ions (~MeV protons or helium) bombard the surface of a sample. While most of the ions come to rest inside the sample, a small portion of ions are backscattered and can be collected by the detector. The collision process can be simulated with classic energy (and momentum) conservation models for elastic collisions, as illustrated by the following equation[5]:

$$E_1 = \mathrm{k}E_0,$$

where E_0 and E_1 are the projectile energy before and after collision, respectively. The kinematic factor, k, is defined as:

$$\mathrm{k} = \frac{{M_1}^2}{(M_1 + M_2)^2}\left\{\cos\theta \pm \left[(\frac{M_2}{M_1})^2 - sin^2\theta\right]^{1/2}\right\}^2,$$

where M_1 and M_2 are the mass of the projectile atom and the target nucleus, respectively, and θ is the scattering angle. Based on this equation, the element (mass) of the scattering atom can be determined based on the energy of the backscattered ions (and a knowledge of mass of the incident particle and the scattering angle). Lighter atoms have more momentum transfer and thus have more energy loss in the backscattered ions. For the extreme case, hydrogen and helium atoms are undetectable in RBS since the incident ions are not backscattered, resulting in many of them forward scattered into the sample. In addition, incident atoms (H or He) lose energy as they travel through the solid. The energy loss depends on the species, energy of the projectile, the density and composition of the sample, and the distance traveled inside the solid. One can also obtain a depth profile by fitting the RBS spectra to a model of energy loss in materials (knowing certain materials properties).

Heavier atoms usually have higher sensitivity in ion scattering due to the higher scattering cross section when compared to lighter elements. On the other hand, even for two high-Z elements, if their atomic masses are

close to each other, it is very challenging to differentiate them in RBS spectra.

However, not all of the collisions between the projectile and the target are physical collisions. In some cases, a nuclear reaction occurs during the collision. By making use of the nuclear reaction, the capability of nuclear reaction analysis (NRA) is developed in the RBS chamber and becomes especially significant for low-Z element measurements (i.e. C, O, N, F) due to their low scattering cross sections in conventional RBS measurements. Moreover, NRA also makes it possible to detect hydrogen atoms in the solid films, which is extremely challenging for most of other elemental analysis techniques. The reactions below are a few popular nuclear reactions for the quantitative analysis of H, D, O and N:

$$^{15}N + {}^{1}H \rightarrow {}^{12}C + \alpha + \gamma$$

$$^{3}He + D \rightarrow \alpha + p$$

$$^{16}O + D \rightarrow {}^{17}O + p$$

$$^{14}N + D \rightarrow {}^{15}N + p$$

In the above nuclear reactions, either the characteristic γ-ray or the fast protons emitted by the reaction are detected in the NRA system.

In summary, RBS (and ion scattering more generally) offers a powerful way to quantitatively measure the elemental concentration with depth information in a solid, and is most quantitative and sensitive for high-Z elements. The extended application of nuclear reaction methods compensated for the low scattering cross section of low-Z elements in RBS and enables detection for most elements in the periodic table.

2.3 Atomic Force Microscopy (AFM)

Atomic force microscopy (AFM), one of the most popular scanning probe microscopy techniques, is a powerful tool to image surface topography of a material. There are many variants of AFM, some of which can be used to image mechanical, electronic, magnetic, optical, chemical and other properties of material surfaces, in addition to structure.

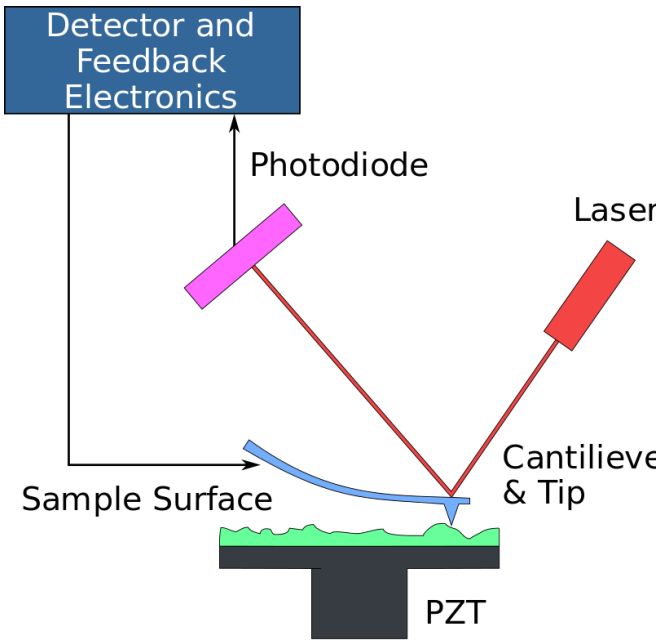

Figure 2.3 The scheme of an AFM setup[6].

Figure 2.3 is a simple scheme of an AFM instrument comprised of a cantilever (with a sharp tip at one end), a laser source, a position-sensitive photodiode, a piezoelectric scanner, and a detector with feedback electronics. When the tip is scanning across the surface of a sample, the cantilever will be deflected due to the atomic force between the tip and the sample surface. The cantilever deflection can be measured by detecting the reflected laser's position on the position-sensitive photodiode. To keep a constant force (or oscillation amplitude) between the tip and the sample surface and to prevent the possible tip damage, a feedback loop is

introduced. The sample is positioned at all three dimensional directions with the help of the piezoelectric to keep the force constant.

As the tip is moved towards the surface prior to scanning, an attractive force will usually appear when sufficiently close that weak interactions. Eventually a repulsive force will result when the tip is in contact with the surface, pushing into the bulk. One can image the surface either when in the attractive or repulsive regime, using either a DC or AC (tip and cantilever oscillating) mode. The non-contact mode is conducted under the attractive force and, as the name suggested, the tip doesn't contact with the surface and usually oscillates at a constant amplitude and/or resonance frequency. In contact mode, the tip contacts the surface and is usually accomplished in a DC (non-oscillatory) mode, with a slight constant repulsion between tip and surface. The non-contact mode has the advantage of less tip and sample surface damage benefiting from non-physical contact. However, the contact mode is the preferred method in some cases, such as probing the surface when immersed in a liquid. Both contact and non-contact are used in soft materials such as polymers. In the tapping mode, the tip is oscillated above a surface with a percentage of the tip's full amplitude. Tapping mode can provide moderately high resolution

and maintain a low level of tip/sample damage, although the exact properties in tapping mode are a complex convolution of film and tip mechanical properties and any other forces that may arise between the two materials.

AFM can be modified to extract more information from the sample. For example, lateral force microscopy (LSM) monitors friction, drag and lateral mechanical properties of the surface by monitoring the cantilever lateral deflection when a tip is scanned across a surface. Electrostatic force microscopy (EFM) and magnetic force microcopy (MFM) can be employed to study the electrostatic (i.e. charges, ferroelectric domains) and magnetic properties of the sample respectively. Kelvin probe force microscopy (KPFM) probes the local potential of a surface, and is used to investigate nanoscale electrical properties[7] (e.g. work function) at the surface of materials and in devices

2.4 Raman Spectroscopy

Raman spectroscopy[8], named after Sir C.V. Raman who won the Nobel Prize for Physics in 1930 due to the discovery of Raman scattering, probes a molecule's vibrational information. Raman spectroscopy yields

information about bonding in molecules and solids, and can help identify composition and chemistry.

To understand Raman spectroscopy, Raman scattering has to be discussed first. When a beam of monochromatic light impinges upon a sample surface, most of the scattered light collected experiences no frequency change; this is called elastic Rayleigh scattering. However, an extremely small portion of the scattered light does experience a lower or higher frequency (energy) shift corresponding to Stokes or anti-Stokes Raman scattering due to the interaction between light and molecular vibrations. By scanning the frequency of the scattered light, various excitation and loss modes in a molecule or material can be investigated. In reality, a near infrared (NIR), visible, or ultraviolet (UV) monochromatic laser is employed as the exposing source. To filter out the majority Rayleigh scattering, either an interference filter or a spectrophotometer is used. However, the biggest instrumental problem is the poor intensity of Raman scattering. To enhance it, many approaches has been developed, such as stimulated Raman with a pulsed high power laser source, coherent anti-Stokes Raman with two laser beams, resonance Raman, and surface-enhanced Raman[9] with proper surface modification.

As both are vibrational spectroscopies, infrared (IR) spectroscopy and Raman spectroscopy have a lot in common. However, the difference between them is significant, usually related to the symmetry of the mode, which helps us make the right choice in tool to use in any given case. The primary difference is that for IR active modes in molecules or solids, their dynamic dipole moments have to change during scanning (symmetric modes are not observed), while in Raman active ones have to have the polarization change (antisymmetric modes are not observed). For example, neutral bonds (i.e. O=O, C-C) with small dipole moment have weak IR absorption but strong Raman intensity. Other differences also exist in different spectra (absorption vs scattering), laser sources, cost of instrumental setup and so on.

2.5 Secondary Ion Mass Spectrometry (SIMS)

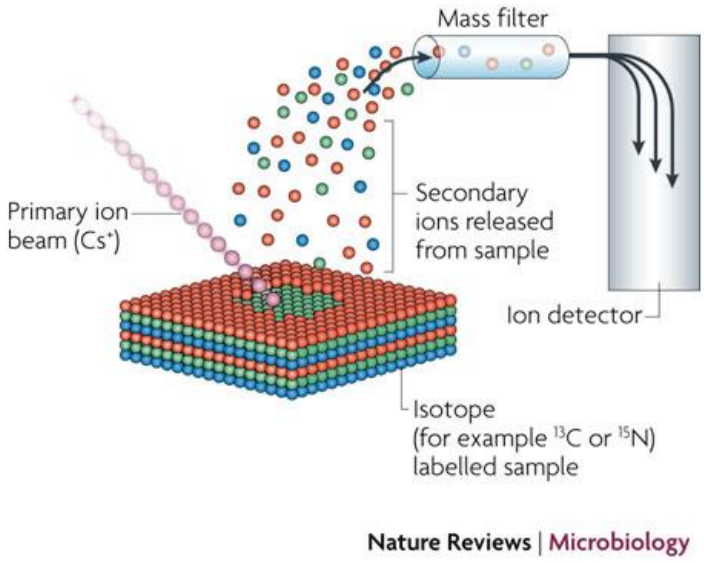

Figure 2.4 The schematic working principle of SIMS[10].

Secondary ion mass spectrometry (SIMS) is a specialized mass spectroscopy method used to quantitatively characterize film composition and to depth profile a film. Compared with regular surface characterization techniques such as AES, XPS, and EDX (with a detection limit of 10^{19}-10^{20} atoms/cm^3), SIMS shows orders of magnitude lower detection limit (10^{14}-10^{16} atoms/cm^3), thus it can quantify impurities present at much lower concentration, for example and probing the depth distribution of dopants. Moreover, SIMS is one of the most surface sensitive compositional analytical techniques with depth information as low as 0.2 nm at a surface. With the help of ion etching, a detailed depth profile can be obtained. In addition, when using the mass spectrometer as a secondary ion detector,

isotopic detection becomes one of its biggest advantages over other compositional characterization methods.

With regard to the SIMS instrumental setup as shown in **Figure 2.4**, the primary components include: the primary ion beam (e.g. O_2^+, Cs^+, Ar^+, Ga^+), the sample/sample holder, the mass analyzer (e.g. quadruple, time of flight, magnetic sector), and the ion detector. The simplified working principle starts by an incident primary ion bombardment on the sample surface, thus further producing secondary ions. These secondary ions can be collected and have their mass analyzed and counted by the ion detector.

However, there are still some limitations for SIMS. First of all, since all of the steps occur in a high vacuum chamber, the sample must be vacuum compatible. Secondly, the process producing secondary ions are not fully understood or controllable. Finally, some complicated molecules are hard to analyze by SIMS due to their complicated secondary ion cracking patterns.

2.6 Scanning Electron Microscope (SEM) and Helium Ion Microscope (HIM)

The scanning electron microscope was first invented in 1937 by Manfred Von Ardenne and became one of the most widely used high magnification (beyond optical limits) microscope. As shown in **Figure 2.5**, a beam of electrons, accelerated by a high voltage (~ kV), applied between the cathode and the anode, is emitted from the electron gun, which usually made of lanthanum hexaboride crystal. This enables high efficient electron emission and narrower electron energy distribution. After traveling through a series of lens, apertures, and coils, the electron beam will be focused, diameter-tailored, and deflected to a certain point on a sample surface, with the energy at the sample usually 10's of keV. Taking advantage of the interaction between the primary electron beam and the surface of the sample, one or more electron detectors can be used to collect electrons emitted from the sample to construct an image. The most common detector is called secondary electron detector, which collects the emitted low energy (<50 eV) secondary electrons, electrons that for the most part are created as the incident electrons lose energy as they scatter through the sample. Another powerful detector, the backscattered electron detector, collects the back scattered high energy primary electrons due to elastic scattering with the sample atoms. One of the biggest advantages of

backscattered electron detectors is that it provides contrast information based on the chemical composition of the sample, due to the fact that heavier atoms backscatter electrons more strongly.

In addition to the electron detectors, energy dispersive X-ray spectroscopy (EDS), as an elemental analytical technique, has become one of the most powerful accessories to microscopy. The EDS detectors collect the characteristic x-rays emitted via energy relaxation that results when outer electrons fall into core shell holes. Occasionally, the EDS spectra become ambiguous because of peak overlap, such as Mn K_β and Fe K_α.

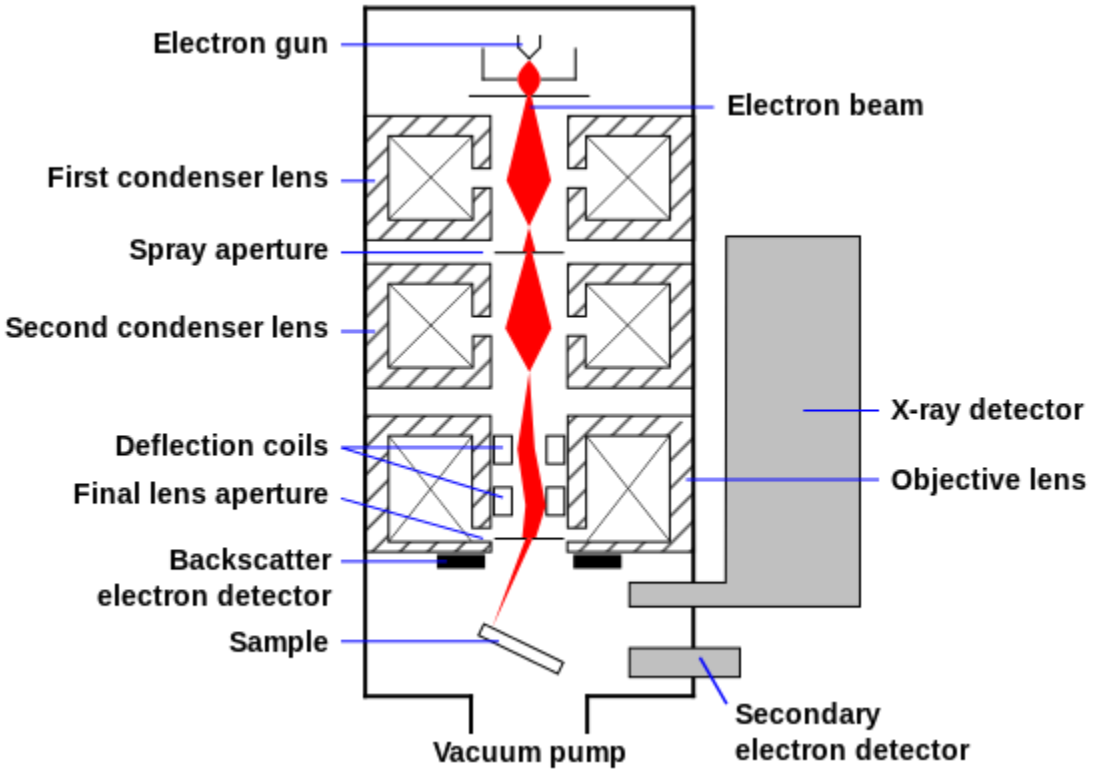

Figure 2.5 A scheme showing how a conventional SEM works[11].

Though SEM has been continuously developed since its invention, limitations (charging, high excitation volume, and mediocre beam resolution) still exist hindering its wider application. Among those limitations, sample charging, due to non-conductive biologically related samples such as organs and cells, severely blurs the image. To solve this problem, a thin conductive layer (i.e. Au/Ag/Pt/C) is usually deposited (i.e. sputtering) on the surface of the sample to increase surface conductivity. Although partially solving the charging issue, conductive layer deposition can also cause other unwanted issues, such as surface damage and topographical deformation.

Helium ion microscopy[12] (HIM) is one of the more excited new developments that helps circumvent the charging problem of SEM. Benefited from using heavier helium ions instead of electrons, the HIM displays some significant advantages. First, due to helium's shorter De Broglie wavelength, a highly confined helium ion beam with smaller diameter can be achieved. Second, because of the higher probability of scattering of helium ions relative to electrons at the same energy, helium beams have smaller excitation volumes, more concentrated at the surface,

thus yielding a better image resolution. Finally, since helium ions have much higher secondary electron yield, HIM has a much higher tolerance on the low conductivity of a sample and can be operated with an extremely low beam current. However, HIM suffers from its own disadvantages. With the heavier helium ion as the primary beam, ion beams usually damage to the surface faster than electrons of the same flux.

From an instrumental perspective, the ion source is one of the major differences. As the predominant ion source technique, a gas field ion source (GFIS) is a technique in which gas phase helium atoms become charged on the apex of a tip placed under a high voltage. They are then further extracted by the negative potential anode. This provides high brightness and small virtual source size. Additionally, as EDS completes SEM with an elemental analysis capacity, HIM has the same potential as well by detecting the energy of the backscattered helium ions, sharing the same working principle with RBS.

Finally, with regard to its patterning application, the helium ion beam can act both as a physical ion source, by milling into the sample with a pattern, and as a chemical activation ion source, which can be used to write

a pattern on a lithographic resists. In a later chapter, we will discuss this issue in detail.

2.7 Other Characterization Methods

Beside the instruments discussed above, other characterization techniques will be briefly mentioned here. Thermogravimetric analysis (TGA) records the mass change of a sample as a function of increasing temperature in a certain gas environment. In this thesis, TGA was employed to monitor the mass change of the $HfOCl_2$ solution, from which we can extract and calculate the accurate concentration information of the original solution. Reflection electron energy loss spectroscopy (REELS) is another tool to characterize some chemical and electronic properties of a material. Meanwhile, the low energy loss spectra shed some light on the possible electron-material interaction modes. We used REELS to look at the possible electron-HafSOx interactions. For the HafSOx film composition analysis, medium energy ion scattering (MEIS; ~100keV ions) was also used to offer depth profile information with higher depth resolution relative to high energy RBS (~1MeV).

References

1. X-ray photoelectron spectroscopy. In Wikipedia.
2. Gilbert, J. B.; Rubner, M. F.; Cohen, R. E., Depth-profiling X-ray photoelectron spectroscopy (XPS) analysis of interlayer diffusion in polyelectrolyte multilayers. *Proceedings of the National Academy of Sciences of the United States of America* **2013,** 110, (17), 6651-6656.
3. Hollander, A.; Haupt, M.; Oehr, C., On depth profiling of polymers by argon ion sputtering. *Plasma Processes and Polymers* **2007,** 4, (9), 773-776.
4. Cumpson, P. J., Angle-Resolved Xps and Aes - Depth-Resolution Limits and a General Comparison of Properties of Depth-Profile Reconstruction Methods. *Journal of Electron Spectroscopy and Related Phenomena* **1995,** 73, (1), 25-52.
5. Mayer, M., Rutherford Backscattering Spectrometry (RBS). In Workshop on Nuclear Data for Science and Technology: Materials Analysis, 2003.
6. Atomic force microscopy. https://en.wikipedia.org/wiki/Atomic_force_microscopy
7. Melitz, W.; Shen, J.; Kummel, A. C.; Lee, S., Kelvin probe force microscopy and its application. *Surface Science Reports* **2011,** 66, (1), 1-27.
8. Schrader, B., *Infrared and Raman spectroscopy: methods and applications*. John Wiley & Sons: 2008.
9. Kneipp, K.; Kneipp, H.; I, I.; Dasari, R. R.; Feld, M. S., Ultrasensitive chemical analysis by Raman spectroscopy. *Chemical Reviews* **1999,** 99, (10), 2957-+.
10. O'Donnell, A. G.; Young, I. M.; Rushton, S. P.; Shirley, M. D.; Crawford, J. W., Visualization, modelling and prediction in soil microbiology. *Nature Reviews Microbiology* **2007,** 5, (9), 689-699.
11. Scanning electron microscope. https://en.wikipedia.org/wiki/Scanning_electron_microscope
12. Hlawacek, G.; Veligura, V.; van Gastel, R.; Poelsema, B., Helium ion microscopy. *Journal of Vacuum Science & Technology B* **2014,** 32, (2).

Chapter 3 : HafSOx thin film characterization

3.1. Introduction

Solution processed hafnium oxide sulfate (HafSOx) was first reported[1] by J. T. Anderson *et al* in 2007 as a dielectric layer incorporated in a thin film transistor (TFT) device. This revealed an extraordinary 10^6 on-to-off ratio and ultra-low nA level gate leakage current compared with other solution processed oxide dielectric films. Moreover, it also was used to fabricate ultra-thin and extremely smooth nano-laminate structures, which demonstrates a super abrupt interface indicating low inter-diffusion between layers. In this paper, the HafSOx films were prepared by mixing sulfuric acid (H_2SO_4) and $HfOCl_2$ followed by a low temperature (135°C) baking and a high temperature (325°C) condensation process to evaporate off the solvent, water.

The use of a HafSOx film in patterning was patented and then published[2] in Microelectronic Engineering by J. Stowers and D.A. Keszler in 2009. In this paper, based on the original solution-processed dielectric HafSOx films, radiation (photons, electrons or ions) sensitive H_2O_2 was

added into the precursor solution (H_2SO_4 + $HfOCl_2$) and spin coated on the Si substrate followed by a soft bake. Patterned by e-beam lithography and developed by tetramethylammonium hydroxide (TMAH), the exposed part remains on the surface, thus HafSOx is a negative resist. HafSOx exhibited a $D_{0.8}$=21 μC/cm^2 (the dose at which the thickness of the developed structure is 0.8 of the fully activated and developed ones) with the contrast (a parameter measuring the resist sensitivity to dose changes) of 2.5, while ZirSOx (Zr replaces Hf) exhibited a $D_{0.8}$= 7.6 μC/cm^2 with a contrast of 2.6. In addition, a critical dimension of 15 nm lines was also achieved with a LWR (line wall roughness) of 1.9 nm.

Unlike conventional solutions such sodium chloride, the water solution of $HfOCl_2$, a component of the HafSOx precursor solution, under acidic conditions becomes a cluster-suspended solution in which the hafnium (IV) forms predominantly a tetra-nuclear cluster[3, 4] bridged by hydroxyl groups with a corresponding formula of $[Hf_4(OH)_8(H_2O)_{16}]^{8+}$. With the addition of H_2O_2 and H_2SO_4, the peroxo and sulfate group[5-7] will both strongly coordinate to the Hf atoms, which may change the cluster size and stoichiometry in solution and eventually film. More importantly, the nature

of the nanometer, or even sub-nanometer, sized central components enables very flat surface to be formed with deposited films.

In this chapter, we will discuss XPS, XPS depth profiling, and RBS, and their uses to probe the information of the HafSOx chemical composition and oxidation states of each element. Raman was employed to investigate the bonding conditions in the films.

3.2. Experimental Section

Precursor solution preparation

The $HfOCl_2 \cdot 8H_2O$ (98+% purity, Alfa Aesar) powder was dissolved in 18.2 MΩ purified water (Millipore) at approximately 1 M concentration followed by filtration to make a hafnium stock solution. TGA (Perkin Elmer TGA7 Thermogravimetric Analyzer) was used to determine the exact concentration. A 50 µl hafnium stock solution was placed inside a platinum crucible, which then was sealed in a quartz tube in an oxygen atmosphere. The heating process was programmed in three stages: (i) 90˚C for 2hr 30min, (ii) 500˚C for 30min, and (iii) 800˚C for 2hrs, with the heating rate kept at 10 °C/min. The accurate concentration was calculated based on the mass of the final fully oxidized hafnium dioxide. 1 M H_2SO_4 (Sigma Aldrich)

and 30 wt% H_2O_2 (Sigma Aldrich) was used as received. The conventional HafSOx precursor solution was prepared by mixing $HfOCl_2$, H_2O_2, and H_2SO_4 solutions, and diluting with 18.2 MΩ Millipore water to around 0.15 M. The HafSOx solution, analyzed by Raman spectroscopy, was finally mixed to a concentration of 0.45 M for the purpose of higher signal intensity from thicker films. A standard $HfOCl_2$:H_2O_2:H_2SO_4 ratio of 1:3:0.7 was used in all HafSOx films unless otherwise noted. All HafSOx solutions were made fresh within 1 hour before the consecutive film deposition.

Film deposition

For all general-purpose HafSOx films, single-side polished N-type As-doped Si<100> wafers (Resistance 0.001-0.005 ohm-cm) with native oxide were used as substrates. Prior to the HafSOx deposition, the Si wafers were cleaned by consecutive sonication in acetone, isopropanol (or methanol), and deionized water. Next, the wafers would be treated by an oxygen plasma for 10 minutes or UV/Ozone for 15 minutes to remove surface adventitious organic carbon and create more surface OH bonds, ensuring better wetting of the surface during the following deposition processes. The 0.15 M precursor solution was filtered by the 0.45μm PTFE

(Polytetrafluoroethylene) filter, then deposited by spin coating (Laurell Technologies) at 3000 rpm for 30s, with an acceleration rate of 3000 rpm/s, then moved onto a hotplate and soft baked at 80-300°C for 3 minutes. After cooling, the films are ready for characterization. For Raman spectroscopy, aluminum substrates (80 nm Al/200 nm thermal SiO_2/Si) treated by 15 minutes oxygen plasma, or 20 minutes UV/Ozone, and were spin coated with the 0.45M HafSOx solution.

XPS

XPS spectra were acquired with a Thermo Scientific K-alpha X-ray photoelectron spectrometer with an Al Kα (1486.6 eV) micro-focused monochromatic X-ray source and ultra-low energy (5-10 eV) electron flood gun to help with charge compensating for samples that charge. A pass energy of 50 eV was used for high-resolution element-specific XPS spectra, while 200 eV was used for low-resolution survey XPS spectra. All spectra were analyzed with the Avantage software package from Thermo Scientific. The binding energy scale was calibrated with the adventitious carbon 1s peak at 284.8 eV. The number of O peaks was set to two, and peak full width half maxima (FWHM) was constrained to be in the range of 1.7-1.8eV

for peak fitting of the oxygen 1s spectral range. Peak fitting was conducted with mixed Lorentzian and Gaussian peak shapes. To remove the "background" intensity enabling us to better focus on peak shape and position, we used a "Smart" Shirley method. For the XPS depth profile, an Argon ion gun was employed to sputter the surface at the energy of 1,000 eV.

RBS/MEIS

Rutgers has a Tandetron style RBS system equipped with a helium ion beam source that we typically operate at 2 MeV. During the measurement, the normal incidence (0°) was set for the primary beam. The backscattered He ions were collected at the exit angle of 17°. For the raw data fitting and analysis, the SIMNRA 6.06 software package was used. For the MEIS measurements, 200 keV He ions were typically chosen as the incident particle and energy.

Raman Spectroscopy

Raman spectra were collected from a Renishaw inVia Reflex Micro-Raman system, which includes three laser sources: 514 nm, 633 nm, and 786 nm. Prior to any measurement, the system calibration was conducted

using a standard pure Si wafer to check if the main Si Raman peak was located at ~ 520 cm^{-1}. The 633 nm laser was chosen as the primary laser for HafSOx film characterization with 100% laser power, exposure time 40 /s, spectra accumulation 15 times, and cosmic ray removal.

3.3. Results and Discussion

TGA was employed to dynamically monitor the mass loss of the $HfOCl_2$ stock solution; an example of a typical TGA curve is shown in **Figure 3.1**. Three mass-loss stages can be spotted in the curve. The drastic mass-loss stage 1, labeled in the figure and located at around 100°C, should be mostly attributed to the loss of solvent water. As the temperature continued to rise to around 200°C, the Stage 2 mass-loss happened largely due to the thermal decomposition[8, 9] of $HfOCl_2$ to hafnium oxide[10] and/or hydroxide. Although we have no direct evidence in our work, the chlorine in $HfOCl_2$ is believed to leave the solution in the form of Cl_2 gas. In the final stage, labeled Stage 3, starting from 400°C up to 800°C, a very gradual mass drop can be observed. In this temperature interval, the further condensation of hydroxyl groups is presumed to occur. Meanwhile, the thermal decomposition of sulfate groups, another possibility, also

contributes to the mass-loss and has been validated in other sulfate systems[11].

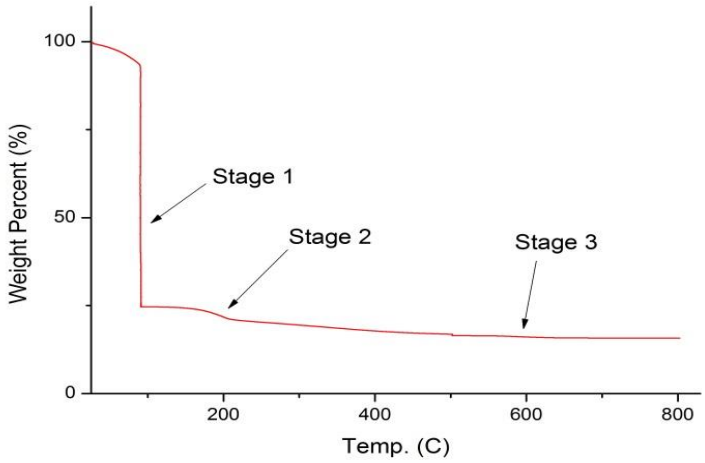

Figure 3.1 An Example of a TGA curve of the $HfOCl_2$ solution mass loss in three-stage heating process.

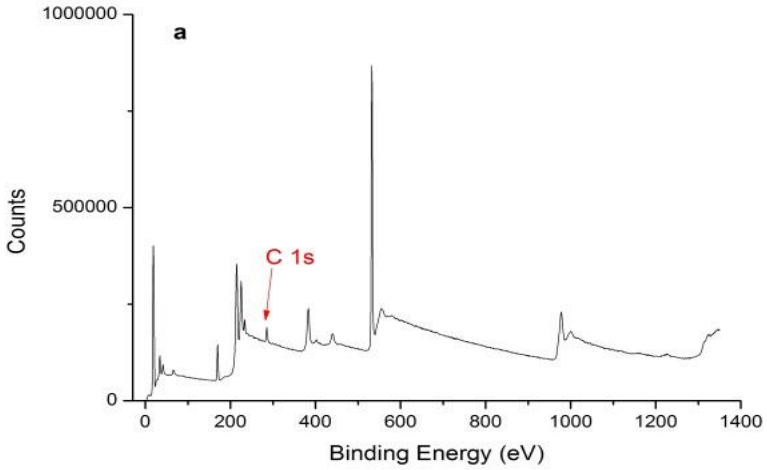
a
1000000
500000
0
Counts
C 1s
0
200
400
600
800
1000
1200
1400
Binding Energy (eV)

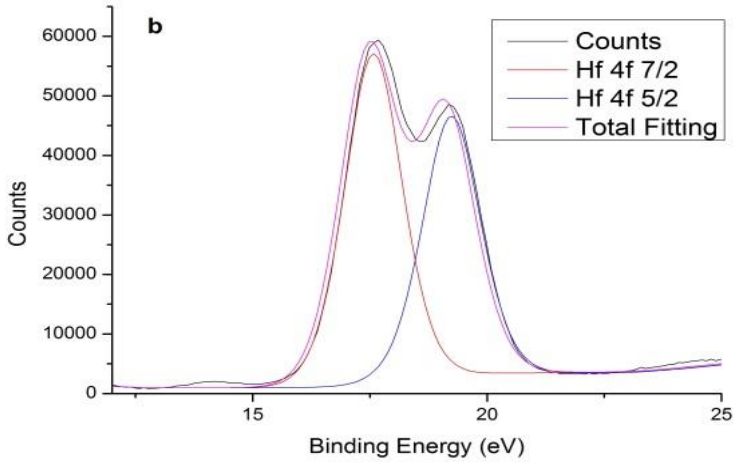
b
60000
50000
40000
30000
20000
10000
0
Counts
Counts
Hf 4f 7/2
Hf 4f 5/2
Total Fitting
15
20
25
Binding Energy (eV)

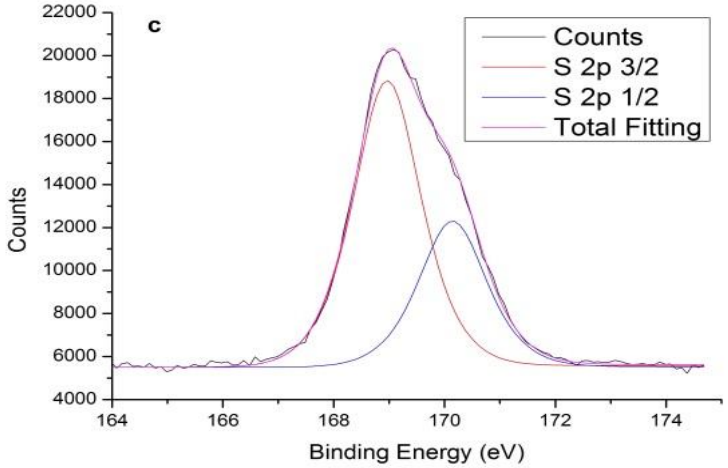
c
22000
20000
18000
16000
14000
12000
10000
8000
6000
4000
Counts
Counts
S 2p 3/2
S 2p 1/2
Total Fitting
164
166
168
170
172
174
Binding Energy (eV)

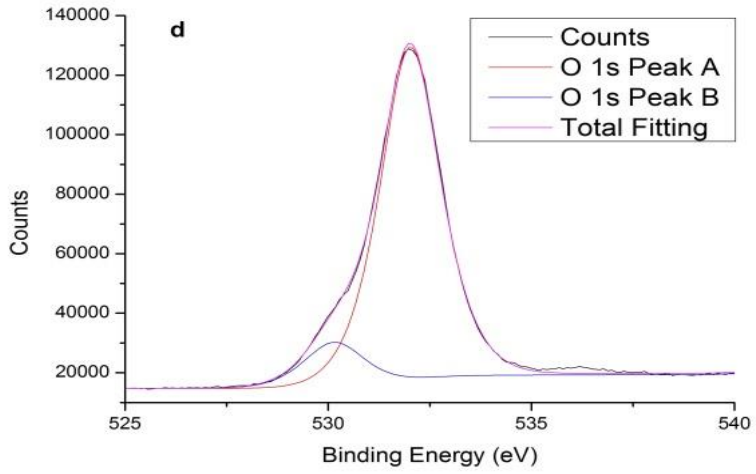

Figure 3.2 XPS data for an 80˚C annealed HafSOx film on a Si wafer: (a) the survey spectrum, (b) the Hf 4f spectrum, (c) the S 2p spectrum, and (d) the O 1s spectrum.

In order to obtain information of the film composition and oxidation states of each element, XPS was a powerful tool employed in this study. **Figure 3.2 (a)** exhibits an XPS survey (wide energy range) spectrum of an 80˚C annealed HafSOx film, from which all elements, Hf, O, and S can be observed. We found carbon as the main impurity. The adventitious carbon impurity mainly results from hydrocarbons absorbed on the film surface, presumably adsorbed from the atmosphere; the surface carbon is used as a

reference[12-15] (284.8 eV) energy (as is commonly done), to calibrate the binding energy of all elements. To carefully investigate each element, high resolution XPS spectra have to be collected with a smaller pass energy (50 eV). As shown in **Figure 3.2 (b)**, the Hf 4f peak was fit by a pair of coupled peaks, the Hf $4f_{7/2}$ and Hf $4f_{5/2}$ doublet at around 17.5 eV and 19.1 eV respectively. The locations of the doublets indicated the Hf (IV) oxidation states in accordance with literature[16-18]. No metallic hafnium, located below 16 eV, has been found. The small bump[19] at higher binding energy (23-25 eV) results from weak energy loss of core-level electrons. Although it has identifiable oxidation states, the detailed hafnium bonding condition is difficult to deconvolute from the limited information. In the S 2p spectrum (**Figure 3.2 (c)**), the main peak at 168.7 eV, fitting quite well with the spin-orbit S $2p_{3/2}$ (168.6 eV) and S $2p_{1/2}$ (170.1 eV) doublet, corresponds well with S in SO_4^{2-} in literature[20, 21]. In **Figure 3.2 (d)**, the O 1s peak with the small shoulder can be modelled with two singlet peaks: a higher binding energy O 1s peak A (532.0 eV) and a lower binding energy O 1s peak B (530.2 eV), which accounts for the small shoulder. The main peak A is attributed to hydroxyl and sulfate groups in the HafSOx film. As for the lower binding energy O 1s peak B, the published literature[22-24], with similar

metal peroxide systems, have attributed it to O in a metal-oxygen-metal frame. In our case, it is due to the formation of the Hf-O-Hf network during x-ray scanning across the surface. This will be discussed in the following chapter as to its importance of radiation chemistry indication of HafSOx resists.

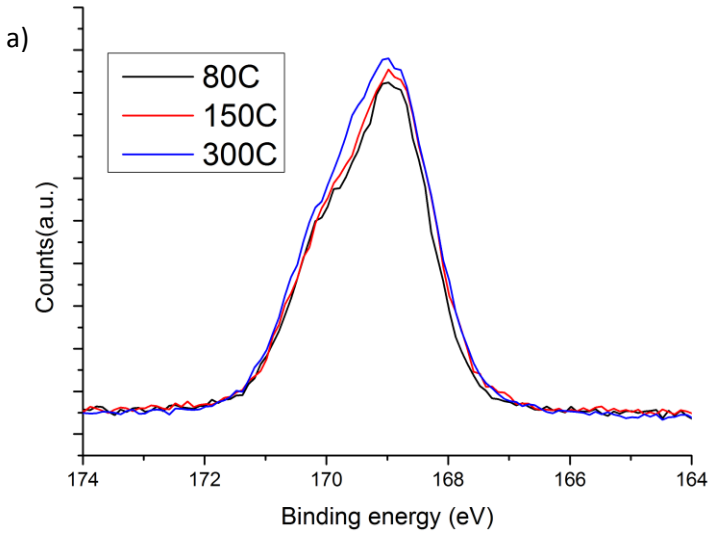

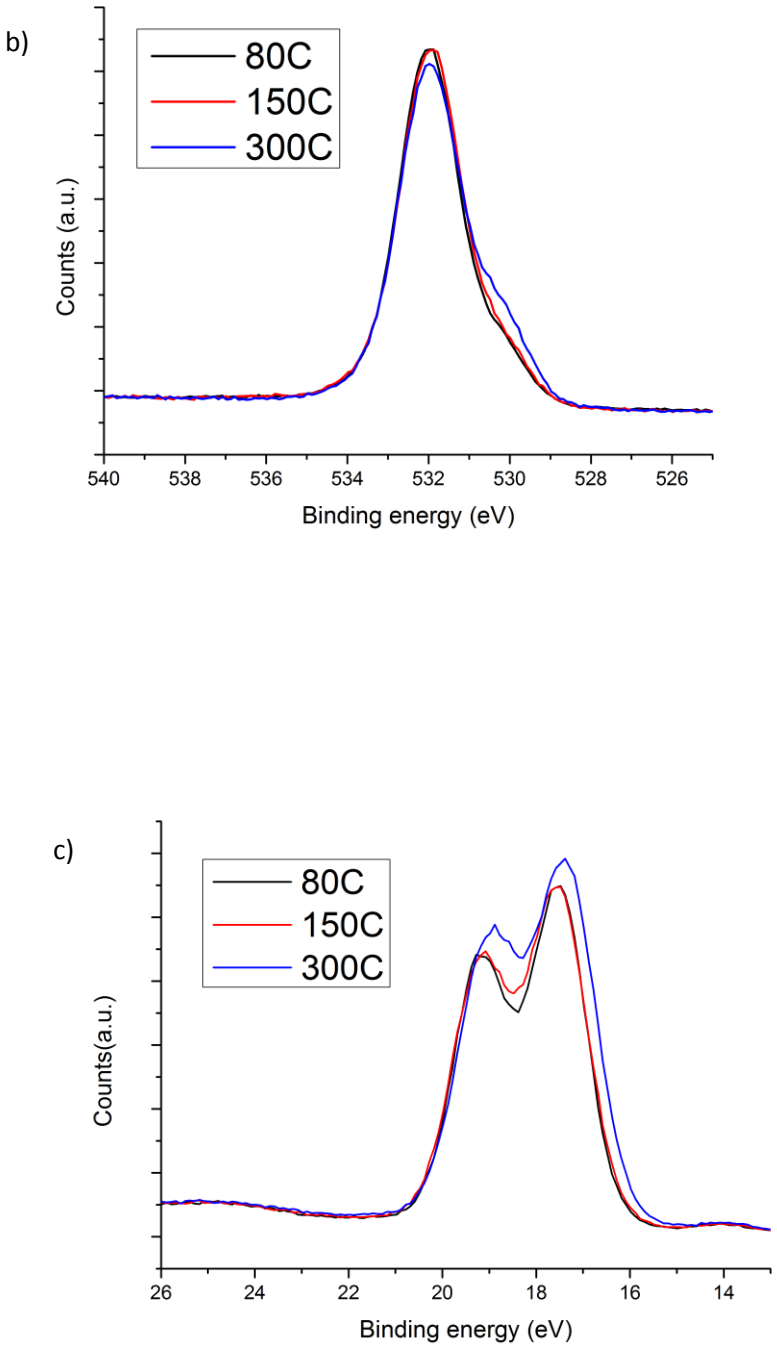

Figure 3.3 XPS peak comparison between various temperatures: (top, a) S, (middle, b) O and (bottom, c) Hf.

The high resolution elemental XPS spectra are plotted against temperature in **Figure 3.3**. The S peaks, in **Figure 3.3 (a)**, shows negligible shift in the position indicating no drastic chemical reaction happened during the temperature increase to 300°C. Supported by the literature[11], the sulfate kept a stable state with increasing temperature until 400-500°C. In **Figure 3.3(b)**, the O peak for 80°C and 150°C annealed samples exhibited no observable changes. However, given the temperature was continuously increasing, the lower binding energy shoulder started to grow. This expansion indicates the formation of more Hf-O-Hf network species due to possible thermal decomposition. Finally, the Hf peaks at various annealing temperatures were compared in **Figure 3.3(c)** and still the Hf peaks of the 80°C and 150°C annealed films showed almost the same peak energy and intensity. Overall, we can conclude from XPS that no drastic change has taken place inside the films when the temperature increases from 80°C to 150°C. However, in accordance with O, there is a noticeable change when annealed from 150°C to 300 °C; a difference on the peak binding energy can clearly be observed. We observed that the Hf peak shifts to lower binding energy by around 0.5 eV during the annealing temperature increase. Since hydroxyl dehydration was proposed to account for the low

binding energy shoulder expansion, it can also be used to explain why the Hf peak shifts to lower binding energy. Assuming the original Hf-OH_2 and Hf-OH bonds were broken and replaced by Hf-O-Hf in the dehydration process, the lower electronegativity Hf (1.3) can extract fewer electrons than the original higher electronegativity H (2.1), which will thus cause a higher density of electrons around the Hf in the Hf-O-Hf network. This will strengthen the electron screening for the positively charged Hf nucleus. The weakened screening effect will increase the kinetic energy of the collected core-shell electrons and, lead to a lower observed binding energy.

Element	80°C	150°C	300°C
Hf	12.7	12.8	13.6
S	13.0	13.3	13.8
O	74.3	73.9	72.6

Table 3.1 Atomic percentages of Hf, S and O in HafSOx annealed at various temperatures.

Other than the oxidation state information, we summarize the stoichiometry information of HafSOx films annealed at various temperatures and the results are exhibited in **Table 3.1**. The Hf-to-S ratio was kept at a relatively constant level, while Hf-to-O increased moderately with temperature, possibly a result of the evaporation of solvent water trapped in the films and further condensation of bound hydroxyl groups.

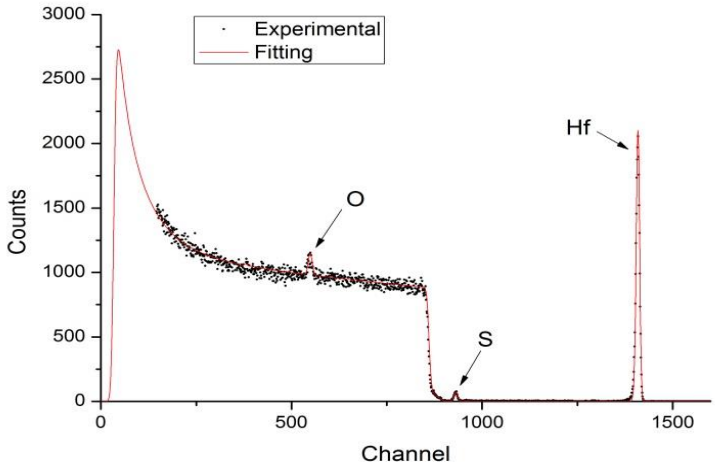

Figure 3.4 RBS data of an 80˚C annealed HafSOx sample

Due to the inelastic mean free path of electrons, XPS can only collect electrons emitted from around the top 5-10 nm of a film. In order to obtain stoichiometric information of the bulk material, other approaches have to be employed. In this study, , RBS, with a 2MeV helium ion source, has been used; **Figure 3.4** shows a conventional RBS spectrum of an 80°C annealed

HafSOx film deposited on Si with native SiO_2. O, S, and Hf are observed as sharp peaks in the spectrum. The plateau, starting from channel number 900, represented the signal from the Si substrate. The low atomic number C is difficult to observe and quantify due to its low cross section in RBS, its small signal to noise ratio, and its overlap with the Si plateau. Suffering from the same reason, the quantification of O is also challenging.

After modeling and peak fitting, the data collected from the normal incidence angle experiment was summarized in **Table 3.2**. Based on the areal density calculated from peak fitting, the film thickness can be determined. As shown in the table, the film thickness decreased from 23 nm to 12.9 nm when the annealing temperature increases from 80°C to 150°C. The film condensation at higher temperatures most likely results from water loss due to simple evaporation and then chemical dehydration, which is in agreement with the Hf:O ratio increase observed in the XPS experiment.

Annealing Temp.	**Areal density (Atom/cm^2)**	**Thickness (nm) by RBS**
80˚C	82.043	23.0

150˚C	77.887	16.2
300˚C	71.102	12.9

Table 3.2 Areal density and calculated thickness for different annealing temperatures.

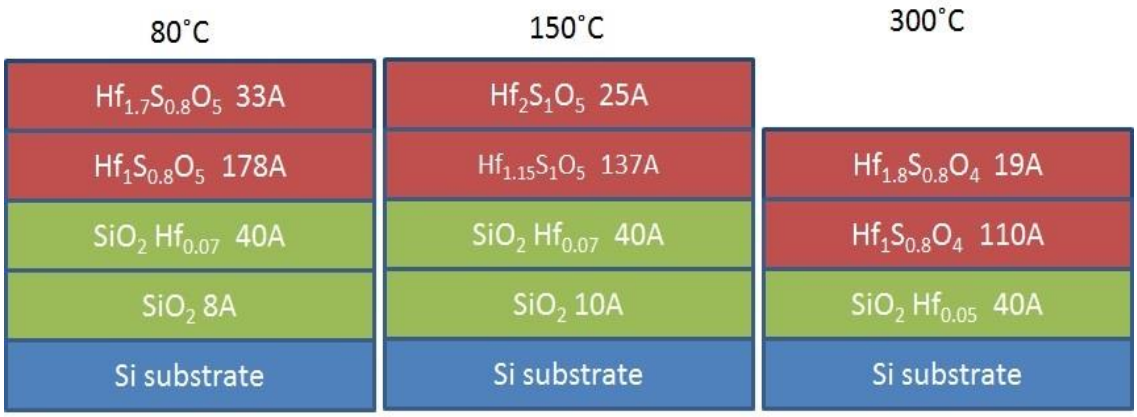

Figure 3.5 Depth profiles of HafSOx annealing at 80˚C, 150˚C and 300˚C from MEIS. Stoichiometries are estimated used simple modeling of the experimental data.

Other than near surface and bulk film composition, depth profiling is another interesting tool used to investigate our HafSOx films. Though our XPS was equipped with a sputtering gun that was capable of depth profiling by alternating between sputtering and XPS probing, sputter depth profiling results in preferential sputtering of some atoms relative to others (i.e.

sputtering rates are 1.5 atoms/ion for Hf and 5.5 atoms/ion for S for 1000 eV Ar ion sputtering). Moreover, surface roughing due to preferential sputtering also results in a sputtering topographical uniformity problem, which makes the depth profile less meaningful. RBS is also capable of depth profiling, but loses depth resolution caused by the high probing ion beam energy. To help resolve this problem, MEIS offers high depth resolution. MEIS spectra were collected, modeled, and finally summarized, as in the **Figure 3.5**. Fit with the similar models, the top HafSOx films annealed at 80°C, 150°C, and 300°C were all fit into a thin top layer (2-3 nm) and thicker bottom layer. Compared with the bottom layer, the top layer had a slightly higher Hf concentration in both cases, which might be caused by Hf atoms migration during annealing, or a change in stoichiometry during exposure to air or vacuum. In addition, in the native silicon oxide layer, a small amount of Hf atoms appear to be incorporated. In 80°C and 150°C annealed films, Hf atoms are not observed throughout the oxide, and there was still a bottom (~1 nm) pure silicon oxide layer. When the annealing temperature goes up to 300°C, the overall oxide layer was incorporated with migrated Hf atoms, which indicated that high annealing temperature favors Hf

migration. But the detailed mechanism of the Hf migration remains unknown for us.

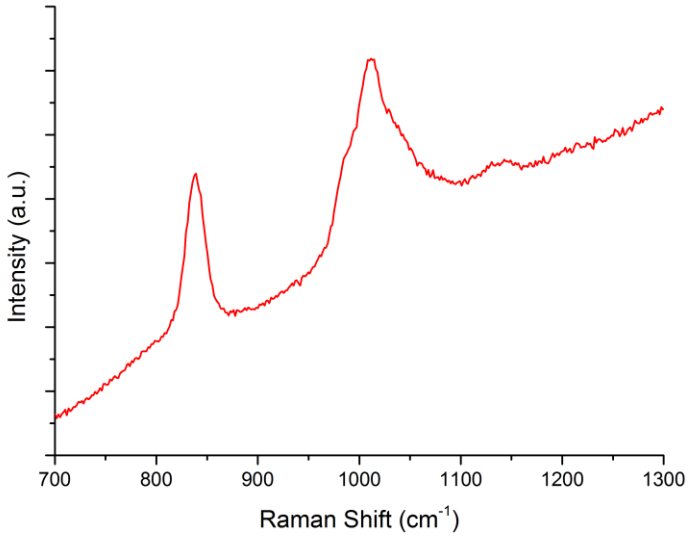

Figure 3.6 Raman spectrum of a HafSOx film annealed at 80 °C

With the help of electron spectrometry and ion scattering, we investigated the film chemical composition and the oxidation state of each element in the films. However, the subtle changes caused by slight changes in bonding were sometimes beyond the resolution of the techniques we have employed. In some cases, IR and Raman offered key complementary information, but careful observation of the vibrational modes of various species in the films. In this study, we used Raman spectroscopy equipped with a 633 nm laser. The spectrum collected from the 80°C annealed

HafSOx films are shown in **Figure 3.6**. Compared with the free ν(O-O) vibration peak at 860-870 cm^{-1} for pure H_2O_2[25-27], the ν(O-O) peak we found in 80°C annealed HafSOx located at 838 cm^{-1} represented a bound O-O bond, which had also been observed in other peroxo complexes[28, 29] of hafnium and zirconium. Similarly, two vibrational peaks of the free bisulfate have been reported at 1050 cm^{-1},[30] but in the film those peaks were shifted to 1009 cm^{-1} possibly due to the sulfate bonding to hafnium. Other systems were also reported with analogous shifts.[31, 32]

3.4. Summary

The HafSOx film characterization acted as a first step prior to the investigation of other film properties. In this chapter, various characterization techniques, including electron spectroscopy, photon spectroscopy and ion scattering, were employed to help us build a thorough understanding of the films prepared under different conditions. XPS enabled us to probe the surface chemical composition and the oxidation states of each element in the film. This sheds some light on the film chemistry as a function of temperature. The higher energy ion scattering, RBS, offered a “nondestructive” way to probe the bulk

composition (and to a limited extent depth profile), which challenging for other approaches. Medium energy ion scattering, MEIS, shares a similar working principle to RBS but provides much higher resolution for the depth profile. Raman spectrometry characterizes vibrational information about the films and is used as a fingerprint to identify the bonding condition in the film.

Even with our advanced film characterization tools, there remain some challenges that persist which limit a complete understanding of the HafSOx films. One of the biggest problems was the beam-induced reaction that happens in the film. For most of the techniques we used, either photons (i.e. x-ray) or ions (i.e. proton or He) with high energy were used as the primary beam to probe the film. This inevitably causes a radiation reaction due to the existence of the photon/ion/electron sensitive peroxides. Therefore, with those methods, it was quite difficult to characterize the very “original” state of film, as it is changing as soon as the first probe species arrives at the surface.

References

1. Anderson, J. T.; Munsee, C. L.; Hung, C. M.; Phung, T. M.; Herman, G. S.; Johnson, D. C.; Wager, J. F.; Keszler, D. A., Solution-processed HafSOx and ZircSOx inorganic thin-film dielectrics and nanolaminates. *Advanced Functional Materials* **2007,** 17, (13), 2117-2124.
2. Stowers, J.; Keszler, D. A., High resolution, high sensitivity inorganic resists. *Microelectronic Engineering* **2009,** 86, (4-6), 730-733.
3. Aaberg, M., An X-ray investigation of some aqueous zirconium (IV) halide, a hafnium (IV) chloride, and some zirconium (IV) perchlorate solutions. **1977**.
4. Muha, G. M.; Vaughan, P. A., Structure of the complex ion in aqueous solutions of zirconyl and hafnyl oxyhalides. *The Journal of Chemical Physics* **1960,** 33, (1), 194-199.
5. Connick, R. E.; McVey, W. H., The aqueous chemistry of zirconium. *Journal of the American Chemical Society* **1949,** 71, (9), 3182-3191.
6. Flynn, B.; Kim, D.; Clark, B. L.; Telecky, A.; Arnadottir, L.; Szanyi, J.; Keszler, D. A.; Herman, G. S., In-situ characterization of aqueous-based hafnium oxide hydroxide sulfate thin films. *Surface and Interface Analysis* **2014,** 46, (4), 210-215.
7. Kalaji, A.; Soderholm, L., A novel nonanuclear hafnium oxide-hydroxide-sulphate cluster crystallised from aqueous solution. *Chemical Communications* **2014,** 50, (8), 997-999.
8. Jiang, K.; Anderson, J. T.; Hoshino, K.; Li, D.; Wager, J. F.; Keszler, D. A., Low-Energy Path to Dense HfO2 Thin Films with Aqueous Precursor. *Chemistry of Materials* **2011,** 23, (4), 945-952.
9. Yoo, Y. B.; Park, J. H.; Lee, K. H.; Lee, H. W.; Song, K. M.; Lee, S. J.; Baik, H. K., Solution-processed high-k HfO2 gate dielectric processed under softening temperature of polymer substrates. *Journal of Materials Chemistry C* **2013,** 1, (8), 1651-1658.
10. Meskin, P. E.; Sharikov, F. Y.; Ivanov, V. K.; Churagulov, B. R.; Tretyakov, Y. D., Rapid formation of nanocrystalline HfO2 powders from amorphous hafnium hydroxide under ultrasonically assisted hydrothermal treatment. *Materials Chemistry and Physics* **2007,** 104, (2-3), 439-443.
11. Halle, J. C.; Stern, K. H., Vaporization and Decomposition of Na2so4 - Thermodynamics and Kinetics. *Journal of Physical Chemistry* **1980,** 84, (13), 1699-1704.
12. Seah, M. P.; Gilmore, L. S.; Beamson, G., XPS: Binding energy calibration of electron spectrometers 5 - Re-evaluation of the reference energies. *Surface and Interface Analysis* **1998,** 26, (9), 642-649.
13. Seah, M. P.; Gilmore, I. S.; Spencer, S. J., XPS: Binding energy calibration of electron spectrometers 4 - Assessment of effects for different x-ray sources, analyser resolutions, angles of emission and overall uncertainties. *Surface and Interface Analysis* **1998,** 26, (9), 617-641.
14. Anthony, M. T.; Seah, M. P., Xps - Energy Calibration of Electron Spectrometers .1. An Absolute, Traceable Energy Calibration and the Provision of Atomic Reference Line Energies. *Surface and Interface Analysis* **1984,** 6, (3), 95-106.
15. Anthony, M. T.; Seah, M. P., Xps - Energy Calibration of Electron Spectrometers .2. Results of an Interlaboratory Comparison. *Surface and Interface Analysis* **1984,** 6, (3), 107-115.
16. Xie, H. W.; Liu, Q.; Li, Y. T.; Lv, H. B.; Wang, M.; Liu, X. Y.; Sun, H. T.; Yang, X. Y.; Long, S. B.; Liu, S.; Liu, M., Nitrogen-induced improvement of resistive switching uniformity in a HfO2-based RRAM device. *Semiconductor Science and Technology* **2012,** 27, (12).
17. Lee, S.; Kim, W. G.; Rhee, S. W.; Yong, K., Resistance switching behaviors of hafnium oxide films grown by MOCVD for nonvolatile memory applications. *Journal of the Electrochemical Society* **2008,** 155, (2), H92-H96.

18. Cao, D.; Cheng, X. H.; Xie, Y. H.; Li, X. L.; Wang, Z. J.; Xia, C.; Zheng, L.; Xu, D. W.; Shen, L. Y.; Yu, Y. H., Properties of HfO2/La2O3 nanolaminate films grown on an AlGaN/GaN heterostructure by plasma enhanced atomic layer deposition. *Rsc Advances* **2014,** 4, (69), 36828-36833.
19. Scientific, T. XPS Reference. http://xpssimplified.com/elements/hafnium.php
20. Sumboja, A.; Foo, C. Y.; Yan, J.; Yan, C. Y.; Gupta, R. K.; Lee, P. S., Significant electrochemical stability of manganese dioxide/polyaniline coaxial nanowires by self-terminated double surfactant polymerization for pseudocapacitor electrode. *Journal of Materials Chemistry* **2012,** 22, (45), 23921-23928.
21. Gao, H. Y.; Wang, G.; Luan, Y.; Chaikittikul, K.; Zhang, X. W.; Yang, M.; Dong, W. J.; Shi, Z., A fast synthesis of hierarchical yolk-shell copper hydroxysulfates at room temperature with adjustable sizes. *Crystengcomm* **2014,** 16, (12), 2520-2526.
22. Yang, W.; Song, K.; Jung, Y.; Jeong, S.; Moon, J., Solution-deposited Zr-doped AlOx gate dielectrics enabling high-performance flexible transparent thin film transistors. *Journal of Materials Chemistry C* **2013,** 1, (27), 4275-4282.
23. Nayak, P. K.; Wang, Z. W.; Anjum, D. H.; Hedhili, M. N.; Alshareef, H. N., Highly stable thin film transistors using multilayer channel structure. *Applied Physics Letters* **2015,** 106, (10).
24. Nayak, P. K.; Caraveo-Frescas, J. A.; Wang, Z. W.; Hedhili, M. N.; Wang, Q. X.; Alshareef, H. N., Thin Film Complementary Metal Oxide Semiconductor (CMOS) Device Using a Single-Step Deposition of the Channel Layer. *Scientific Reports* **2014,** 4.
25. Giguere, P.; Srinivasan, T., A Raman study of H2O2 and D2O2 vapor. *Journal of Raman Spectroscopy* **1974,** 2, (2), 125-132.
26. Giguère, P. A.; Chen, H., Hydrogen bonding in hydrogen peroxide and water. A raman study of the liquid state. *Journal of Raman spectroscopy* **1984,** 15, (3), 199-204.
27. Venkateswaran, S., Raman Spectrum of Hydrogen Peroxide. *Nature* **1931,** 127, 406.
28. Tarafder, M.; Bhattacharjee, P.; Sarkar, A., Peroxo complexes of chromium (VI), molybdenum (VI), tungsten (VI) and zirconium (IV) ions containing tridentate and quadridentate neutral ligands. *Polyhedron* **1992,** 11, (7), 795-798.
29. Tarafder, M. T. H.; Miah, M. A. L., Novel Peroxo Complexes of Zirconium Containing Organic-Ligands. *Inorganic Chemistry* **1986,** 25, (13), 2265-2268.
30. Malinowski, E. R.; Cox, R. A.; Haldna, U. L., Factor-Analysis for Isolation of the Raman-Spectra of Aqueous Sulfuric-Acid Components. *Analytical Chemistry* **1984,** 56, (4), 778-781.
31. Szilagyi, I.; Konigsberger, E.; May, P. M., Characterization of Chemical Speciation of Titanyl Sulfate Solutions for Production of Titanium Dioxide Precipitates. *Inorganic Chemistry* **2009,** 48, (5), 2200-2204.
32. Rudolph, W. W.; Brooker, M. H.; Tremaine, P. R., Raman spectroscopy of aqueous ZnSO4 solutions under hydrothermal conditions: Solubility, hydrolysis, and sulfate ion pairing. *Journal of Solution Chemistry* **1999,** 28, (5), 621-630.

Chapter 4: Radiation chemistry of HafSOx as a lithographic resist

4.1 Introduction

As discussed in Chapter 1, the positive-tone resists (e.g. PHEMS[1], PMMA[2] and t-BOC[3]) usually undergo a scission mechanism during exposure, thus creating a solubility difference between the exposed region and the unexposed region. This eventually made the pattern show up on the surface. On the contrary, to achieve a similar solubility disparity, a mechanism akin to the polymerization or cross-linking has been proposed and validated as one of the most predominant paths for negative-tone resists (e.g. HSQ[4], COP[5], SU-8[6]). To investigate the radiation chemistry of HafSOx, the nature of the films had to first be considered.

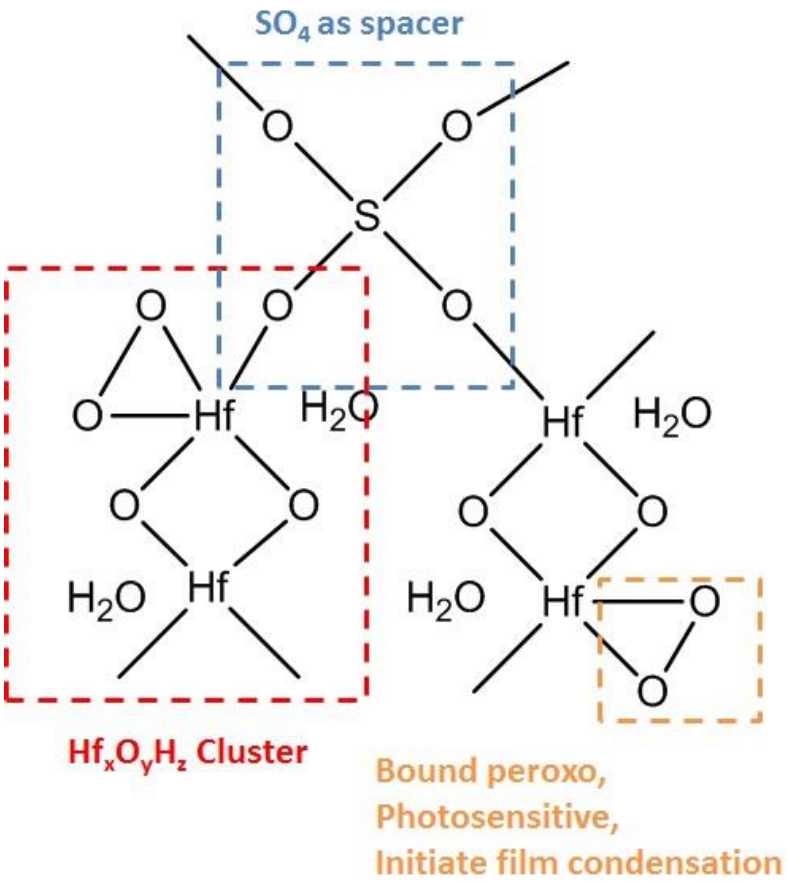

Figure 4.1 The scheme of the cluster composed HafSOx films.

As shown in **Figure 4.1**, three major components exist in the HafSOx films. The monomer of the films is nanometer, or sub-nanometer, sized Hf oxide/hydroxide cluster which provides sufficient chelating sites and contributes to the atomic level smoothness of the film. The peroxo (-O-O-) group, bound to Hf atoms, act as the radiation sensitive sites to initiate the radiation chemistry that results in a film solubility change. The sulfate (SO_4^{2-})

group, another indispensable component, works as a spacer to prevent two adjacent clusters from approaching too close to each other; it appears to limit cluster aggregation and film degradation.

Based on the above model, a radiation-induced cluster networking mechanism, as shown in **Figure 4.2.**, was proposed for the HafSOx film as a negative resist. The radiation sensitive peroxo groups, initiated by the electrons, photons, and ions, can decompose, breaking the -O-O- bond and forming Hf-O-Hf bonds between two adjacent clusters. Zooming out to a larger scope, the individually-separated clusters formed a large cluster network upon radiation.

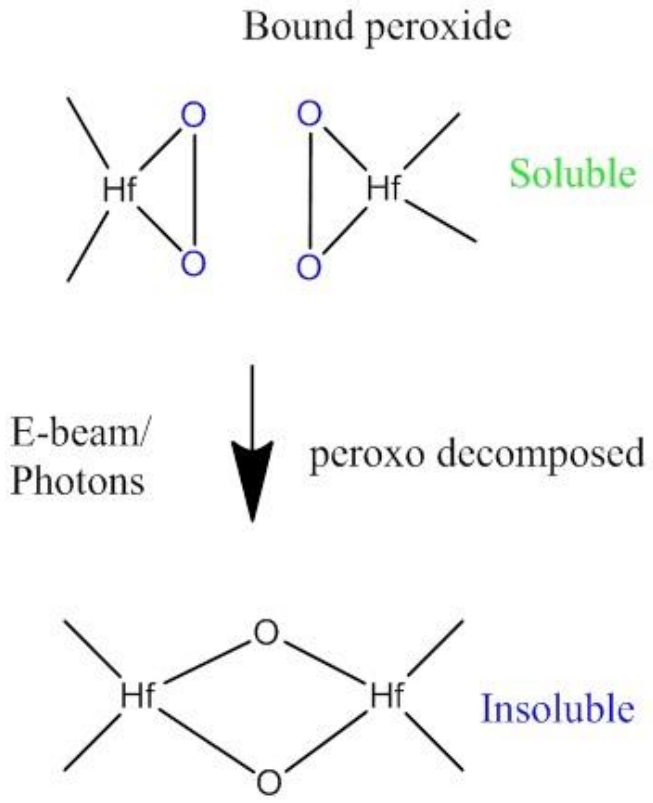

Figure 4.2 Proposed bond breaking and bond formation induced by photons/electrons with the sufficient energy

From a larger scale perspective, the solubility of the films changes according to the behavior of the nanoclusters as shown in **Figure 4.3**. Without energy deposition via radiation, the as-deposit films, with individually separated clusters, fully dissolve in the development solution (e.g. tetramethylammonium hydroxide (TMAH)) due to its small size. However, given enough radiation with sufficient energy, the cluster will

aggregate and form a large hafnium oxide/hydroxide network, which becomes insoluble in the development solution. Therefore, for a radiation exposed patterned film, after development, the exposed part remains while the unexposed part is totally dissolved making HafSOx a negative-tone resist.

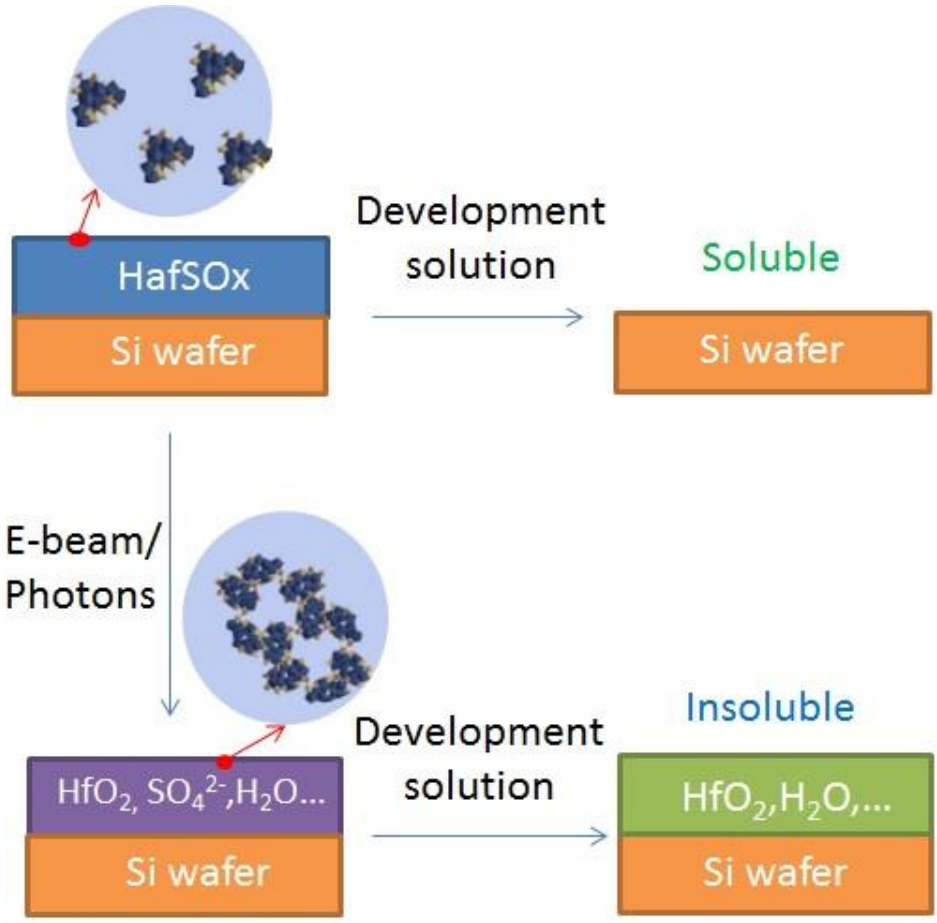

Figure 4.3 Film solubility change in different stages of the lithography process

To validate and explore the detailed mechanism, XPS is employed to investigate the film's composition at different stages of its lithographic process. Meanwhile, the x-ray source equipped in XPS emits 1200-1400 eV x-rays acting as the radiation source to chemically activate the film, and provides us an in-situ way to dynamically monitor the film change during radiation exposure. The structure of the film is extremely challenging since the film itself is amorphous and all of the analytical tools, such as XRD[7], do not work for our films. In this study, we choose isotopic labeling and time-of-flight (TOF) SIMS techniques[8] aimed at extracting some information to complement our limited knowledge of the clusters in the solid films.

4.2 Experimental

Film exposure and development

The HafSOx precursor solution and solid films were prepared by the methods mentioned in Chapter 3. The HafSOx solution, without H_2O_2, was prepared with the pre-selected Hf-to-sulfate ratio and hafnium final concentration by simply replacing H_2O_2 with distilled water with the same volume. The films for the patterning purpose were annealed at 80°C for 3 min using a soft bake procedure. A ZEISS Ultra-55 scanning electron

microscope installed with a J.C. Nability pattern generation system was employed for pattern operation at a 30kV accelerating voltage at a dose of 800μC/cm^2. The post-exposure films were developed in a TMAH water solution (25 wt%, Sigma Aldrich) for 60s followed by a thorough water rinse and a consecutive hard bake on a hotplate at 300°C for 3-5 minutes.

XPS

XPS was operated under the same conditions mentioned in the previous chapters. For in-situ monitoring of the peak evolution of each element, XPS spectra were collected and saved after each scan at the same point using a low pass energy (50 eV).

Isotope labeling and SIMS

The ^{18}O labeled $H_2{}^{18}O_2$ (Icon Services Inc., 1.12% ^{18}O) was chosen to prepare the HafSOx precursor solution but the deposition method and conditions remained unchanged. All TOF-SIMS testing was performed at the Evans Analytical Group (East Windsor, NJ) using a Ga^+ primary beam.

4.3 Results and Discussion

For general purposes, the accumulation of a number of scans helped to obtain a spectrum with a better signal-to-noise ratio, as shown in **Figure 4.4(c)**. Unfortunately, we lose some extremely significant information by extended scanning. High energy x-rays continuously shine on the photon-sensitive HafSOx during the XPS measurement. In other words, the radiation chemistry can occur inside the film from the very first moment when x-rays hit the sample surface. Therefore, by consecutively collecting every XPS spectrum with time, instead of accumulation in the default data collection mode, we were able to dynamically trace the radiation chemistry and film composition change, in-situ, that was induced by x-ray during XPS exposure and measurement.

Figure 4.4 exhibits the XPS O1s peak at the 1^{st}, 5^{th} and 20^{th} scan and, as we described in the previous chapter, we can fit the peaks with two O1s singlets: the higher binding energy peak A (~532 eV) and the lower binding energy peak B (~530 eV). Peak A represents O in sulfate and hydroxyl groups while peak B stands for O in the oxide structure---the Hf-O-Hf network. As soon as we completed the peak fitting for them, we found something quite interesting. Without significant peak shifting, the intensity of peak B with lower binding energy increased significantly. The scan

numbers went up from the 1st scan and 5th scan to 20th scan, indicating the formation of Hf-O-Hf network species during the XPS measurement. And furthermore the radiation chemistry happened in a relatively large and measurable time scale.

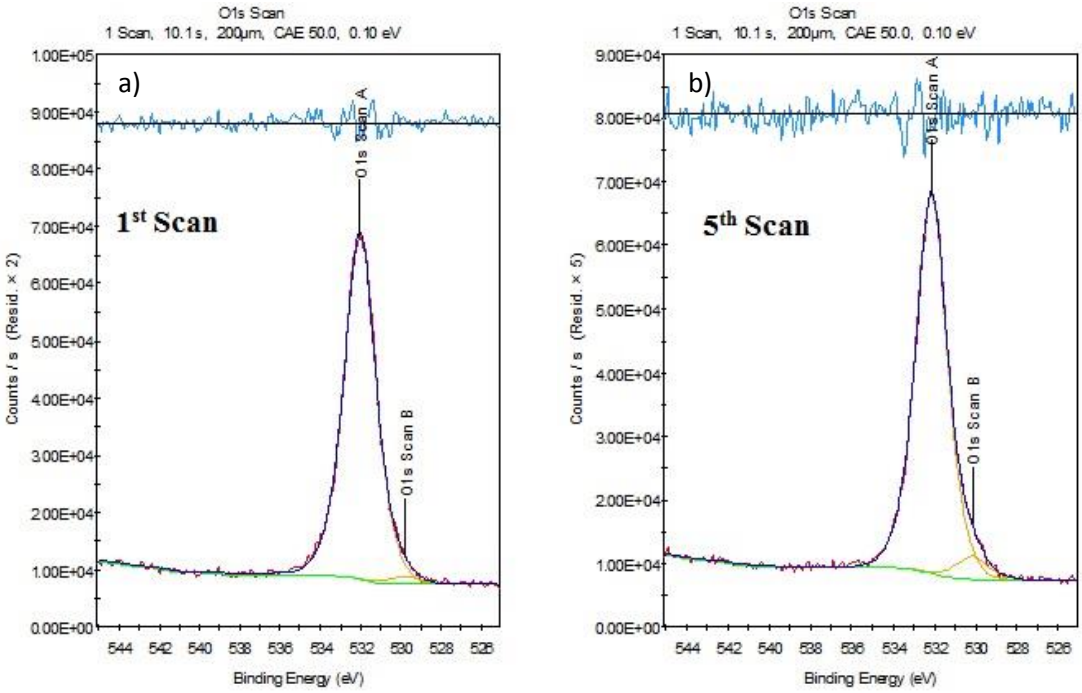

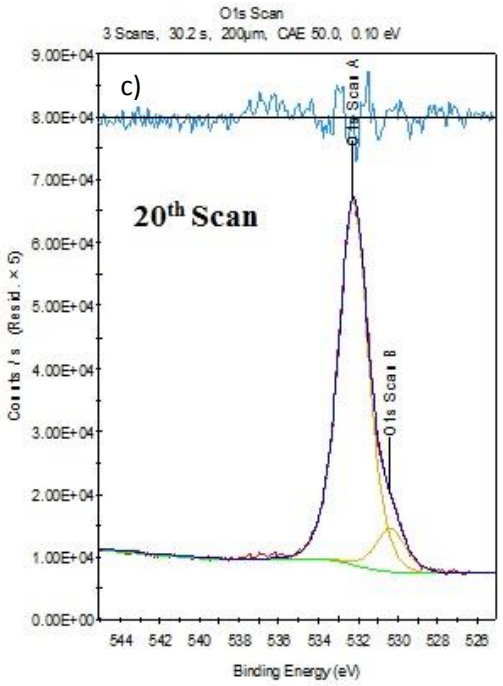

Figure 4.4 The O XPS peak evolvement with x-ray exposure: (top left, a) 1stscan, (top right, b) 5thscan and (bottom, c) 20th scan.

After observing this interesting peak evolve, we reorganized the data by calculating the percentage of the O1s peak B area out of the overall O1s peak area. Then, as you can see in **Figure 4.5**, we plotted a curve of peak B relative intensity (as a percentage of total O1s peak intensity) against the number of scans (in effect time) for HafSOx films annealed at different temperatures.

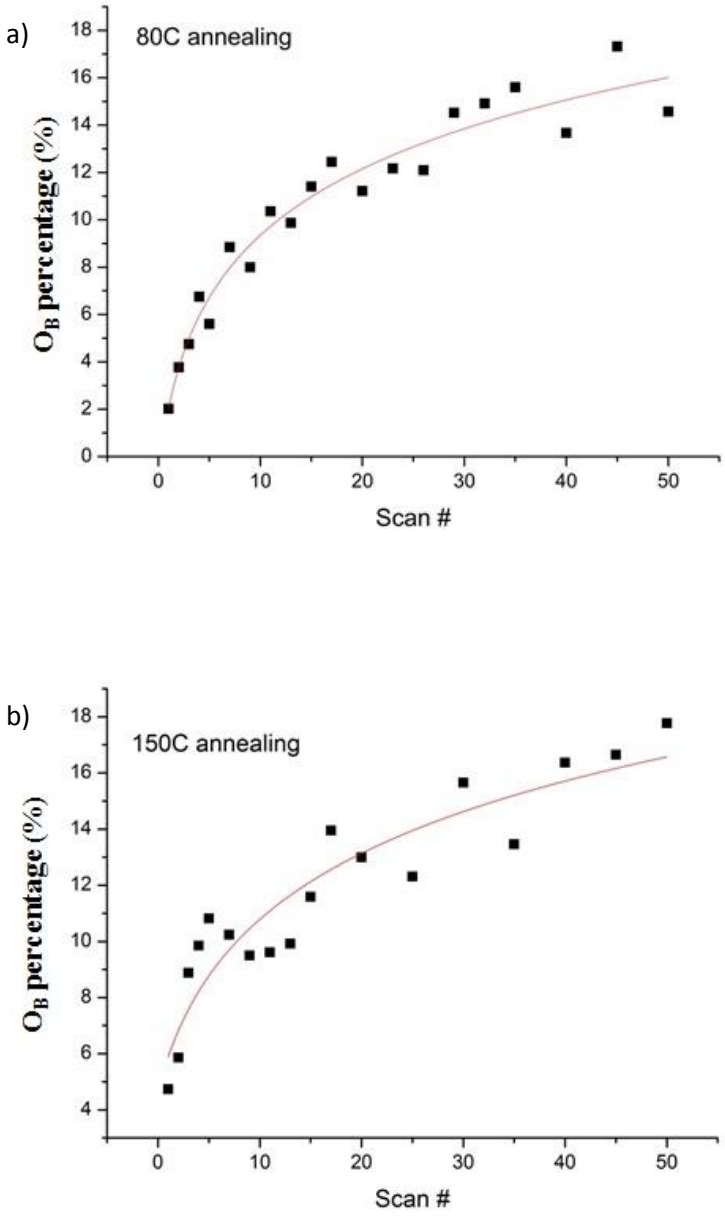

Figure 4.5 O1s peak B percentage change with number of scans for films annealed at various temperature: (top, a) 80°C and 150 °C

In both cases, the curves start at a very low percentage of O1s peak B in the first scan, then they followed a path akin to a logarithmic increment and finally they become almost saturated after 50 scans, which also depicts the dynamics of Hf-O-Hf formation upon x-ray activation. Before the x-ray exposure, the clusters are bound and protected with peroxo groups. It appears that at room temperature, there is a low probability for two adjacent clusters to react with each other to form the Hf-O-Hf network thus showing almost no O1s peak B in XPS at the first scan. But as soon as the XPS exposure begins, x-rays appear to initiate the chemistry that breaks the bound peroxo (-O-O-) species and producing reactive O species (e.g. $O\cdot$, O^+, O^-, O_2^-…) that react with adjacent clusters to grow the Hf-O-Hf network. Eventually this process saturates, and the amount of Hf-O-Hf species that is produced and detected stops. At this point, the O1s peak B reaches a plateau.

A number of other differences in the spectra can also be found by comparing the 80°C and 150°C annealed films. The higher annealing temperature leads to a slightly higher O1s peak percentage for the first scan (2% at 80 °C vs 5% 150°C) but in the end they share a similar level. Trying to understand this, we think the higher annealing temperature will

lead to a thermally-induced bond breakage for some of the less tightly bound peroxo groups, which will form a small portion of Hf-O-Hf network in advance, before the x-ray exposure. However, because the total amount of available peroxo groups are limited and are the same between these two samples, we end up obtaining same total amount of Hf-O-Hf species after x-ray exposure for a certain length of time.

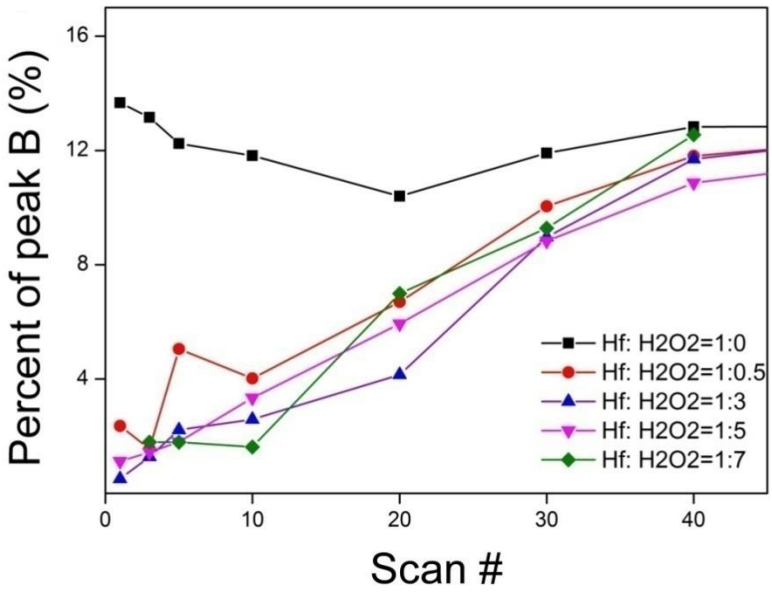

Figure 4.6 The O1s peak B percentage change vs number of scans for HafSOx films with various Hf-to-peroxo ratios

Motivated by this result, we prepared HafSOx films with various Hf-to-peroxo ratios, starting with no H_2O_2 added, repeating the same experiment and finally plotting the percent of O1s peak B as a function of the scan number, as shown in **Figure 4.6**. With various Hf-to-peroxo ratios, the films basically showed only two different behaviors in the graph. The film without H_2O_2 exhibited almost a constant level of O1s peak B percentage. And furthermore, the level of its O1s peak B stayed around 13%, the level at which the films with H_2O_2 eventually display a saturated O1s peak B percentage. With the proposed mechanism in mind, it's not difficult to understand this phenomenon. Without the addition of H_2O_2, the available bonding sites, where the peroxo groups are supposed to attach, will be occupied by the hydroxyl groups since the precursor solution was a water solution. We therefore assume that when a soft bake is applied without H_2O_2, it induced the dehydration of hydroxyl groups between two adjacent nanoclusters and forms a large scale Hf-O-Hf network. Therefore, substantial O1s peak B intensity appears at the first scan. Because almost all of the available –OH reacted to form the Hf-O-Hf network, further x-ray exposure did not produce the oxide network anymore and that is why the peak B percentage always stays at a constant level.

Another interesting response observed is that, independent of the Hf-to-peroxo ratio, the films with H_2O_2 all shared a similar behavior as a function of exposure (time, scan#) in the graph; this was somewhat puzzling until we discussed it with our collaborators in Oregon State University. Raman data had been obtained for analogous HafSOx precursor solutions prepared at different Hf-to-peroxo ratios shown in **Figure 4.7** (Credit to Jennie Amador). In this figure, two types of peroxide bonding modes were found and investigated, as discussed in the previous chapter: bound peroxide at a wavelength of 834 cm^{-1} and free peroxide at 876cm^{-1}. We found that when H_2O_2 was added in the precursor solution, the bound peroxide Raman peak was the first to be observed before the free peroxide was observed, which provided a clear proof that the bound peroxide was the thermodynamically more stable one (under our conditions). Moreover, the bound peroxide intensity became saturated when the peroxo-to-Hf ratio reached 0.5, at which point free peroxide mode peaks began to be exhibited in the Raman spectra. In other words, the Hf clusters could only accept a certain number of peroxo groups, limited by the number of available bonding sites, and excess peroxide will stay in solution as free non-bonding species. More importantly, as discussed in the previous

chapter and was demonstrated by our collaborators, no free peroxide Raman peak was ever found in the soft-baked HafSOx films no matter how much excess peroxide had been added. This tells us that all excess free peroxo groups in the precursor solution are thermally decomposed during the soft bake, and the bound ones, due to stabilization of the chemical bonding, survived the annealing process. Therefore, all HafSOx films with over 0.5 peroxo-to-Hf ratio will all end up with the same amount of bound peroxo groups through the annealing process. That is why all of our films with H_2O_2 in **Figure 4.6** exhibit similar fingerprint curves.

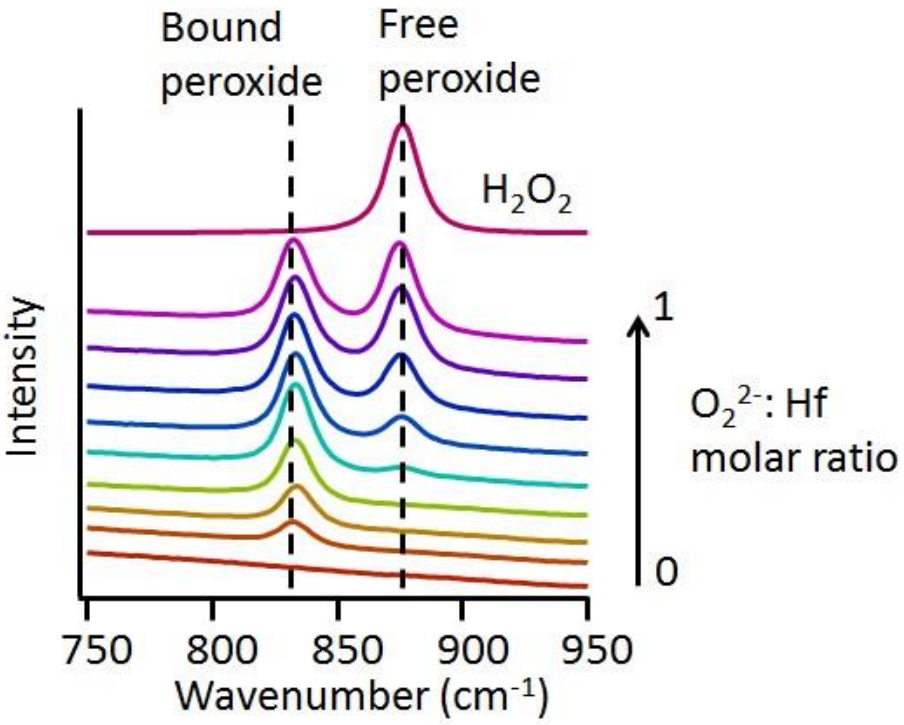

Figure 4.7 Raman spectra comparison among HafSOx precursor solutions with various Hf-to-peroxo ratios

Subsequently, we investigated the O1s peak B behavior for HafSOx films prepared with various Hf-to-sulfate ratios. Three informative facts have been found in this graph. First, after comparing the initial O1s peak B percentages of those films, we found that less sulfate in the film contributed to a higher initial O1s peak B percentage which implies more initial Hf-O-Hf network. Sulfate groups act as spacers between clusters to prevent them from further reaction. The lack of sulfates leads to cluster instability. On one hand, more hydroxyl groups bond to the Hf sites where sulfate groups, when present, can stabilize the system. One the other hand, not enough sulfate exists to prevent possible cluster aggregation. Both of those effects resulted in a significant formation of Hf-O-Hf network species. Therefore, less sulfate ended up with more initial Hf-O-Hf network. Second, the HfSOx film with a 1:2 Hf-to-sulfate ratio exhibited no Hf-O-Hf network species. Since Hf in the film is in its 4+ state, its maximum bonding capacity to sulfate groups is 2 sulfates per hafnium. In this case, we reached its maximum ability to chelate with sulfate groups. And we find no Hf-O-Hf

network forming during either the soft bake process and x-ray exposure, which is evidence that for the HafSOx films, the sulfate groups likely have a higher bonding strength to Hf than peroxo or hydroxyl groups. Finally, the films with low Hf-to-sulfate ratio, ranging from 0.1 to 0.4, all exhibit almost the same shape curves with only a difference in the relative intensity. This indicates that in when insufficient sulfate is present, the peroxo groups occupy their original chelating sites and do not bond more to the original sulfate bonding sites, which are occupied by the hydroxyl groups in the solvent.

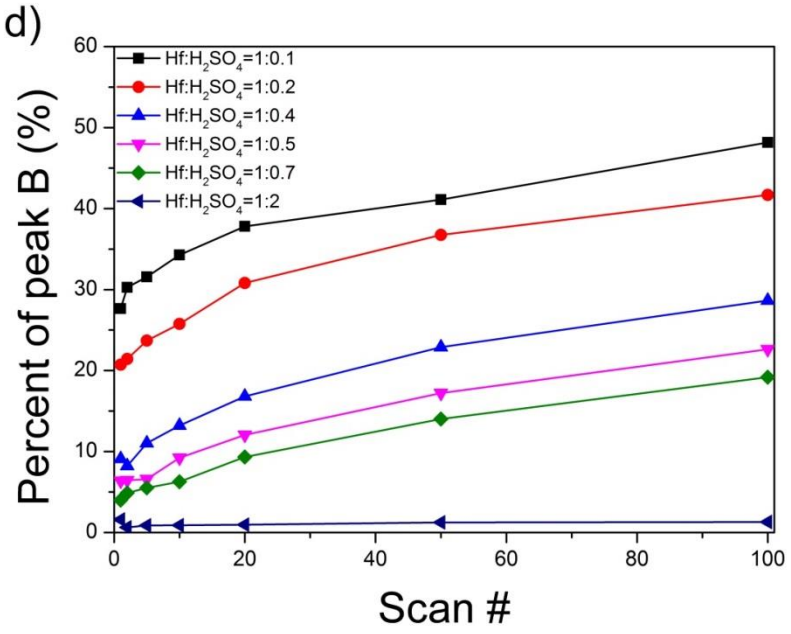

Figure 4.8 The O1s peak B percentage change vs number of scans for HafSOx films with various Hf-to-sulfate ratios

In addition to in-situ monitoring of each element's evolution during x-ray exposure, we also explored compositional changes at different stages of a typical lithographical process. As shown in **Figure 4.9**, four different samples were investigated based on an 80°C annealed HafSOx film with H_2O_2: the as-deposit film, the directly developed film, the film exposed (with a 30 keV e-beam exposing tool at a dose of 800 μC/cm^2 in this experiment), and the exposed & developed sample.

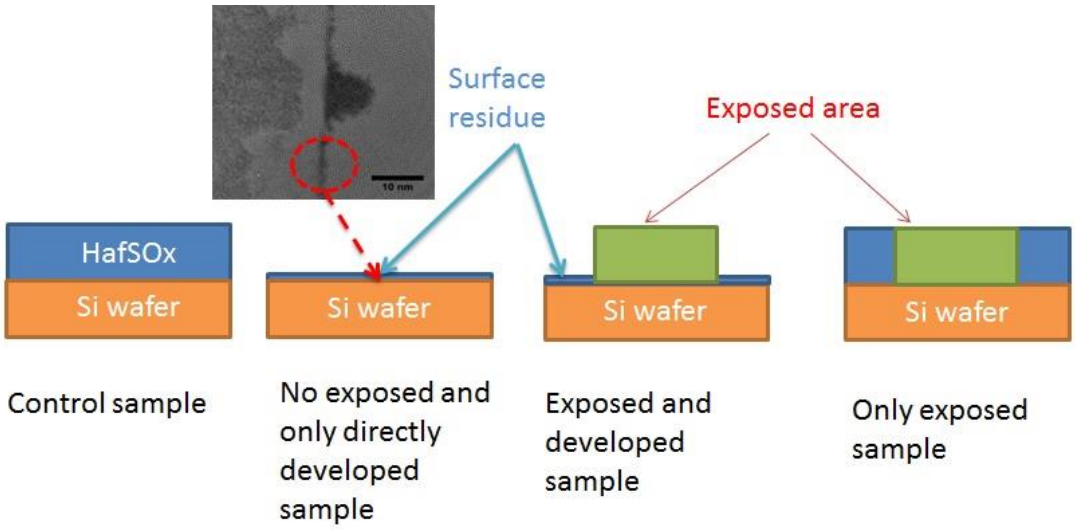

Figure 4.9 The scheme of the tested HafSOx films at different stages of a typical lithographic process

The XPS data of each sample is summarized in **Table 4.1**. First, comparing the control as-deposit film and the developed (but not exposed) one, we found that there was still a small amount of Hf remaining on the surface with all S removed, although theoretically we should have dissolved the whole film in the TMAH development solution. This trace Hf residue on the surface has been spotted in TEM[9] as well. Nevertheless, the chemical composition of the Hf residue and the reason how it is produced on the surface remained currently unknown. One of the possible reasons is that the clusters at the interface react and dehydrate with the hydroxyl group at the SiO_2 surface (due to the oxygen plasma or UV/ozone treated Si wafer that we need to obtain a hydrophilic surface) during the soft bake process, thus a thin layer hafnium oxide/hydroxide might form at the interface.

Second, by comparison between the inside (or exposed) area of an exposed & developed film with the original as-deposited film, we found all S is gone and we only have Hf and O left with a ratio around 1:3. Therefore, we know that sulfate groups left the film during the development process, possibly by a sulfate ion exchange with OH^- from TMAH.[10, 11] Furthermore,

the 1:3 Hf-to-O ratio indicated that the exposed & developed HafSOx films became hafnium oxide hydroxide, not a traditional 1:2 HfO_2 film. In addition, no observable difference has been spotted between the as-deposit films and exposed only films, which resulted from the activation of x-ray during the XPS measurement. Therefore XPS does not really probe the compositional information of the "true" as-deposit films due to the fact that the x-rays begin activating the film as soon as they are turned on.

Element	**Control sample**	**Developed only**	**Exposed & developed**		**Exposed only**	
			Inside	**Outside**	**Inside**	**Outside**
Hf	12.3%	Trace Hf	25.9%	Trace Hf	12.6%	12.4%
S	13.4%	No S peak	N.A.	No S peak	13.6%	13.2%
O	74.3%	Mainly from SiO2	74.1%	Mainly from SiO2	73.8%	74.4%

Table 4.1 Atomic percentages of each element in HafSOx films at various lithographical stages.

Other than the stoichiometric information, we also investigated the XPS peak shift at the various stages during the lithography process. The main clearly evident peak shift observed was the Hf 4f peak, which was compared between the as-deposit films and exposed & developed films. As shown in **Figure 4.10**, the XPS Hf 4f peak shifted to a lower binding energy by ~ 1 eV after exposure and development; this can be explained by changes in electron screening. During development, the sulfate groups bonding to Hf are replaced by hydroxyl groups. Though both of these two functional groups bound to Hf via O, the secondary atoms bonding to the primary O are different: S in sulfate (-O-SO_3) case and H in hydroxyl group (-O-H). Because S (2.5) has a higher electronegativity than H (2.1),[12] the OH will lead to a more electron abundant Hf atom, which will screen its center positive nucleus, increase the kinetic energy of ejected electrons, resulting in a smaller binding energy.

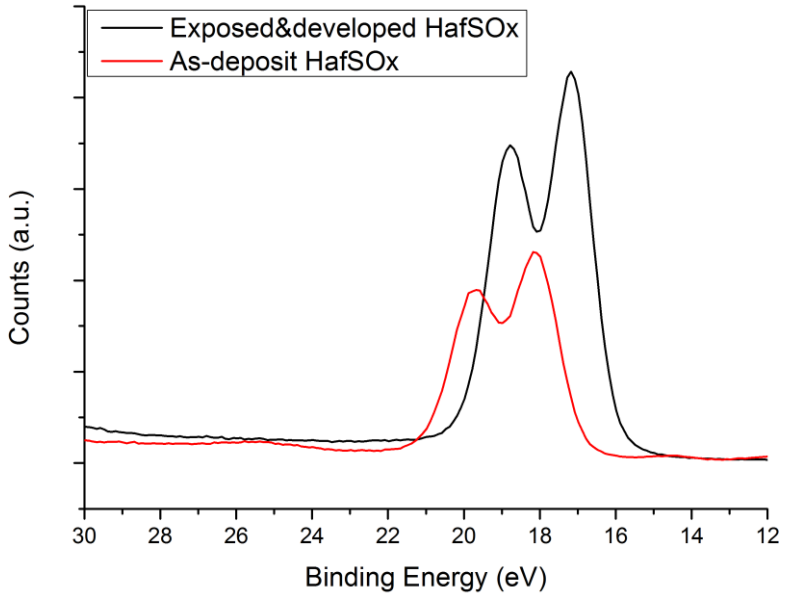

Figure 4.10 The comparison of Hf 4f XPS spectra between as-deposit and exposed & developed films

In addition to the significant Hf 4f peak change, the O1s peak change, as shown in **Figure 4.11**, was more on a peak-shape level change as opposed to the binding energy level. As discussed above, the O1s peak of as-deposit HafSOx films can be fit with a high binding energy (BE) peak related to the sulfate and hydroxyl groups and a low BE peak related to the oxide network. However, after exposure & development, we found a fairly different O1s peak, which can be fitted with three singlets: a low BE peak

(at ~530 eV), a medium BE peak (at ~532 eV), and high BE peak (at ~533eV). The low BE peak represents the hafnium oxide network and the medium BE peak was primary due to the hydroxyl groups since all sulfate groups were removed in development. The very small amount of high BE peak might be caused by water being absorbed during the development in TMAH water solution. For the exposed & developed film, by calculating the atomic ratio between Hf and low BE (~530 eV) peaks, a value around 1:2 can be obtained, indicating the HfO_2 stoichiometry.

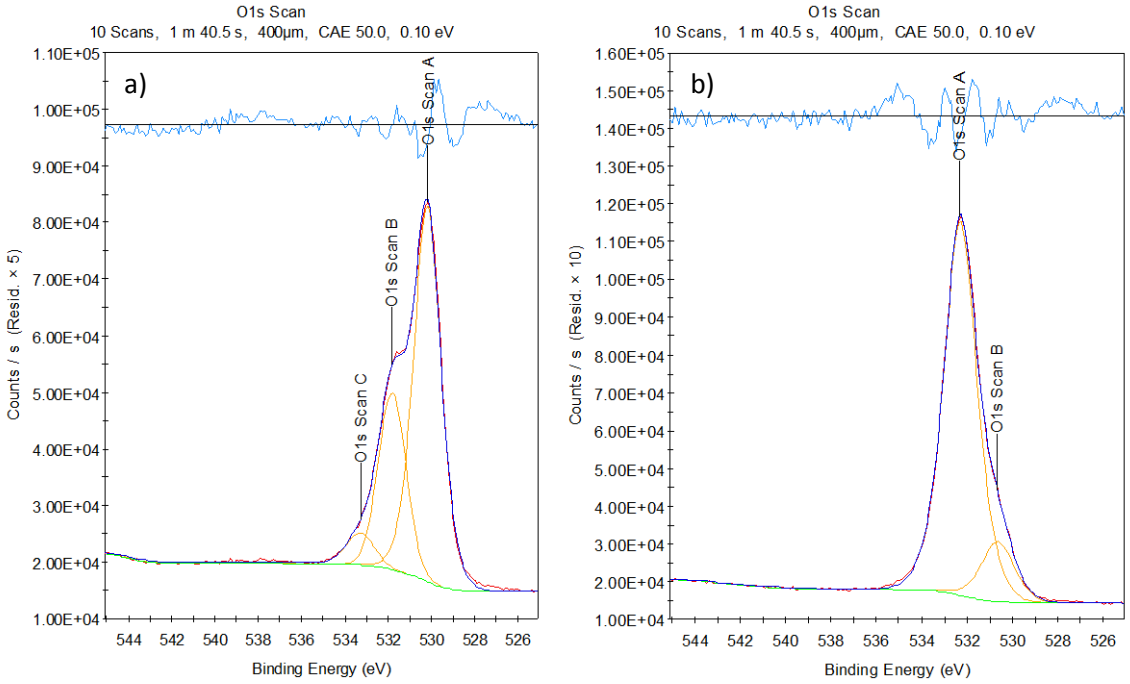

Figure 4.11 The comparison of O1s XPS spectra between (left, a) exposed & developed films, and (right, b) as-deposit films

Knowing the peroxo group worked as a radiation sensitive species in the resist films, we made films with and without H_2O_2 and characterized those films at different lithographic stages with XPS. **Table 4.2** exhibits a compositional difference between HafSOx films with and without H_2O_2. In general, no drastic compositional difference was found except a slightly higher O1s low BE peak ratio. However, after we developed those two films with TMAH and characterized with XPS, we found more differences. One of the differences was found by comparing their Hf 4f peaks as shown in **Figure 4.12**. For the HafSOx films with H_2O_2, almost all of the Hf was washed away by TMAH and only a small amount of Hf remained, with the possible reasons we have previously discussed. Whereas the Hf signal in HafSOx without H_2O_2 in the film didn't change significantly resulting from cluster aggregation aided by hydroxyl bonding during the soft bake process.

	HafSOx w/ H2O2	**HafSOx w/o H2O2**
Hf (at %)	13.5 %	14.0 %
S (at %)	12.2 %	12.2 %

O (at %)	69.3 %	65.8 %
C (at %)	5.0 %	8.0 %
Hf: S: O	1: 0.9: 5.1	1: 0.9: 4.7
O(low BE)/ O (total) %	11.6 %	16.8 %

Table 4.2 Atomic percentage comparison between HafSOx w/ H_2O_2 and HafSOx w/o H_2O_2

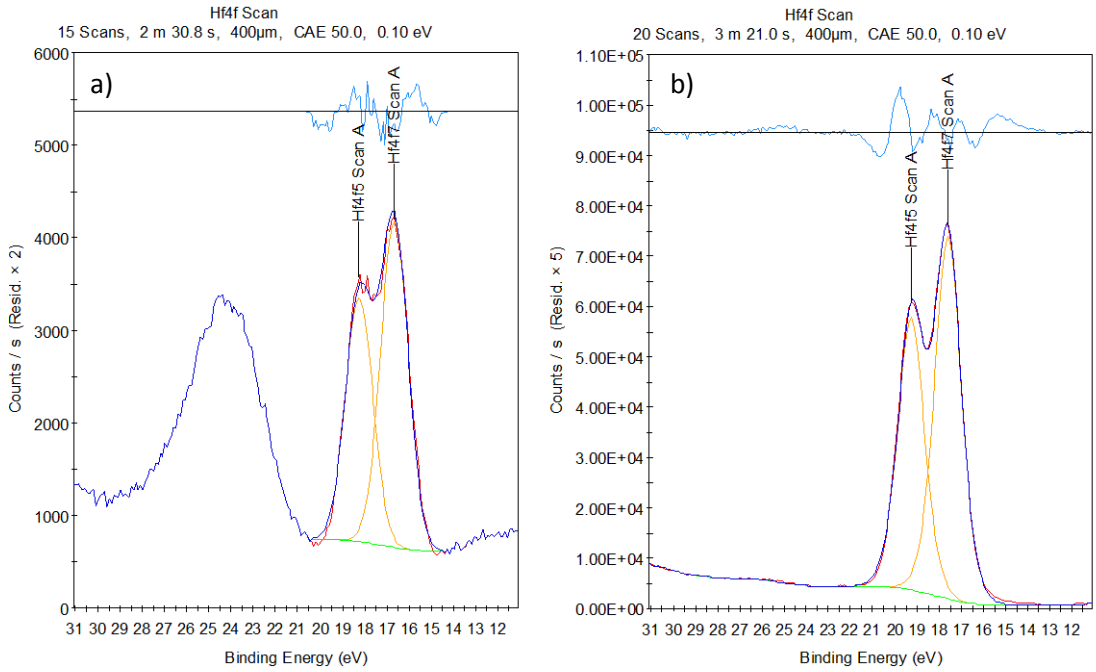

Figure 4.12 The XPS Hf 4f peaks for the HafSOx films (left, a) w/ H_2O_2 and (right, b) after direct development.

Moreover, similar to the HafSOx with H_2O_2 films, the Hf 4f peak shifting to lower binding energy, as shown in **Table 4.3**, was also observed due to the sulfates leaving during the development process. Therefore, no matter whether H_2O_2 was added, the developed process seemed to not be disturbed significantly and the sulfate groups would be dissolved away from the films.

w/o H_2O_2	**Control**	**Developed only**
Hf 4f 7/2	**18.08 eV**	**17.16 eV**
Hf 4f 5/2	**19.74 eV**	**18.81 eV**

Table 4.3 The XPS Hf 4f peak binding energy shift for HafSOx w/o H_2O_2after direct development.

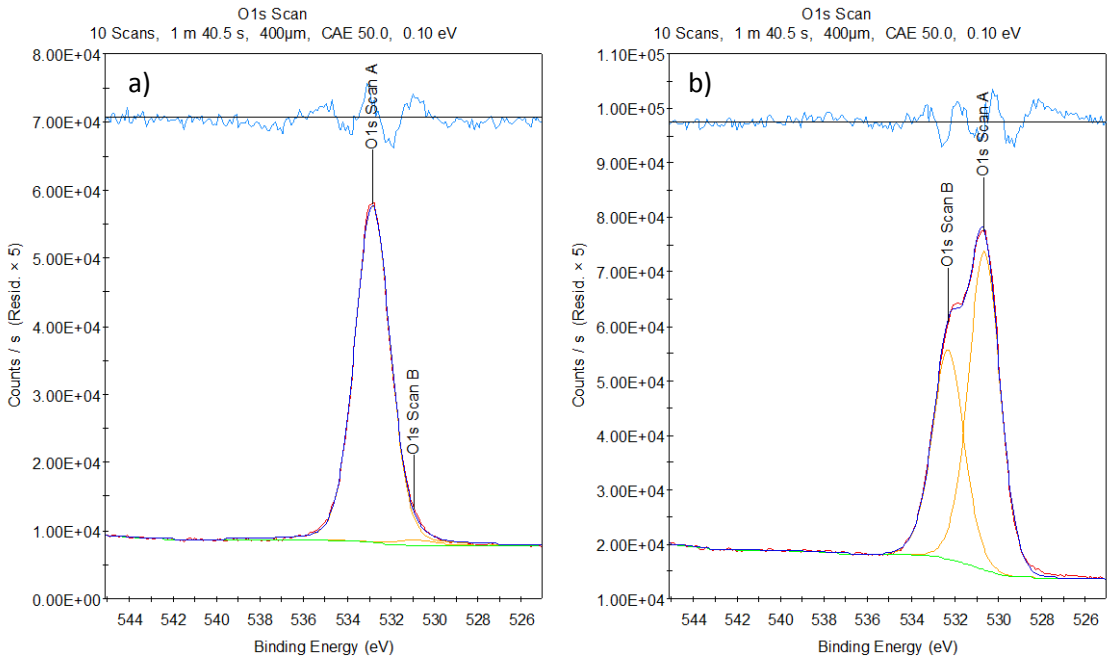

Figure 4.13 The XPS O1s peak binding energy comparison for HafSOx films made (left, a) w/ H_2O_2 and (right, b) w/o H_2O_2 after direct development

In addition, the XPS O1s peaks were compared between the films with and without H_2O_2 after the direct development. In **Figure 4.13**, we can see that the film with peroxide exhibited a high intensity representing the O below th silicon oxide layers because all of the HafSOx layer was removed. But the O1s peak, fit with low BE peak related to the oxide and a high BE peak accounting for hydroxyl groups, in the film with peroxide indicated that the large scale of Hf-O-Hf network and some bound hydroxyl groups remained on the surface.

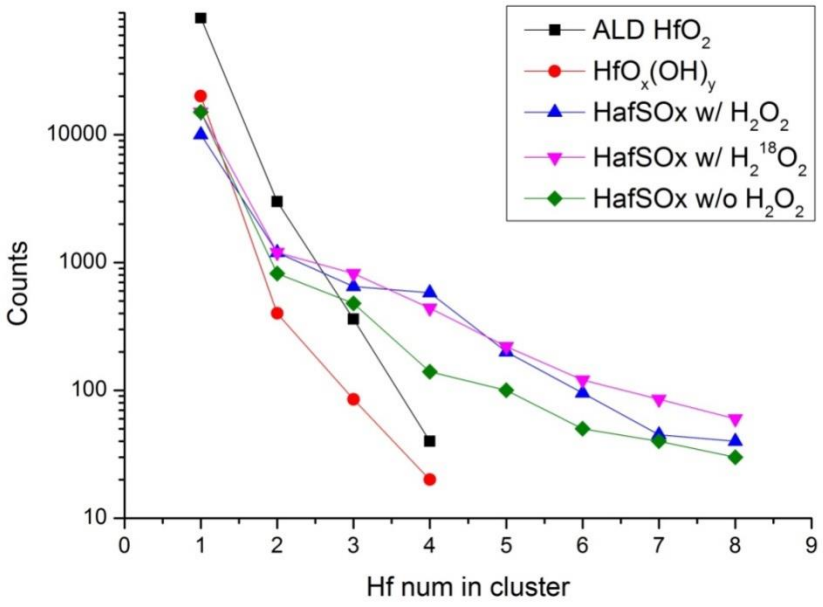

Figure 4.14 The number of Hf in a cluster made from different HafSOx and Hf oxide/hydroxide films.

Limited by the film's amorphous nature and sub-nm size, the film structure characterization on the cluster level was extremely challenging. SIMS was used with the hope that the primary ion sputtering may dissociate some monomer clusters to be collected and characterized by the time-of-flight detectors. What's more, aided by isotopic labeling approach, $H_2{}^{18}O_2$ used in this study, we expected to find more details about how the peroxo groups change the structure of the small clusters. In this study, we

prepared 5 films within two categories. An ALD made HfO_2 film and an $HfO_x(OH)_y$ film, made from exposing and developing an HafSOx film. Three HafSOx films with $H_2{}^{16}O_2$, with $H_2{}^{18}O_2$, and without H_2O_2, respectively, represented the cluster composed films. The SIMS data are summarized and plotted in **Figure 4.14** in a manner that attempts to quantify the cluster size. Clearly, we can see that for all normal films, the maximum cluster included 4 Hf atoms while all of the cluster composed films had a maximum cluster of 8 Hf atoms; this is quite intriguing although not understood.

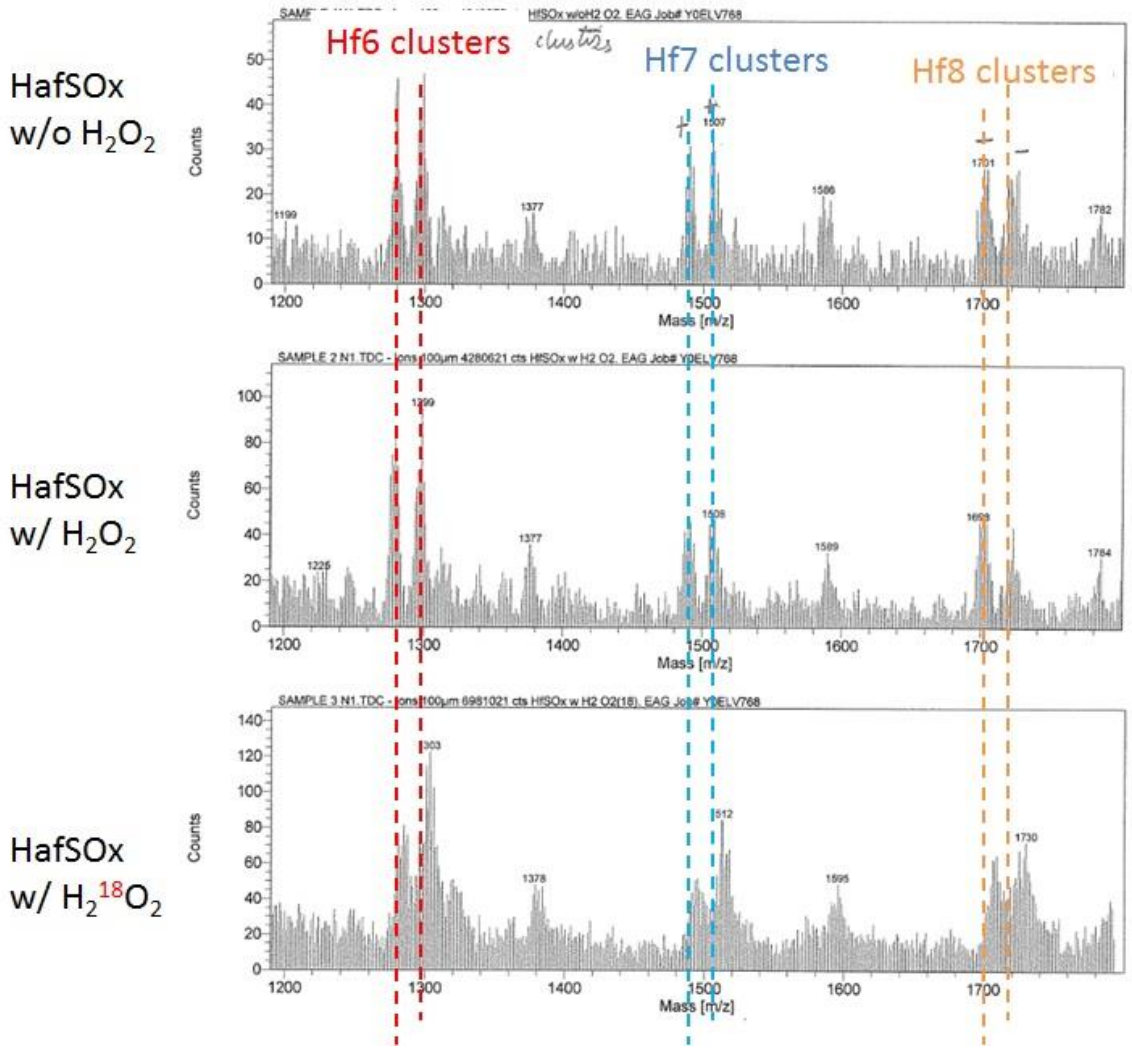

Figure 4.15 The SIMS spectra comparison among different HafSOx films.

Moreover, we also compared the mass spectra among the cluster composed films. As shown in **Figure 4.15**, comparing films with and without peroxide, we found that the cluster size fingerprints resembled each other, which indicated the existence of H_2O_2 only benefits the cluster networking but does not necessarily change the size of the cluster. In addition, in the comparison between films with regular peroxide and ^{18}O labeled peroxide,

we found that the isotopically labeled peroxo was incorporated in clusters with various sizes. Nevertheless, it is nearly impossible to determine how many peroxo groups were incorporated in each kind of cluster due to the limited resolution.

4.4 Summary

In this chapter, we explored the proposed radiation chemistry at three different levels. At the first level, we focused on the in-situ dynamic monitoring of the chemistry of the peroxo breaking and the Hf-O-Hf network formation upon radiation, with the help of in-situ XPS. On the next level, we tried to probe the film transformation, from the atomic to the cluster level, by adopting SIMS and isotopic labeling technique. On the final level, we focused on the results of the radiation chemistry and the whole process of a complete lithography process by comparing the different processing stages aided by XPS.

Although we now know some detailed information about the mechanism, there remain a few challenges not fully understood. For example, in spite of some cluster speciation information obtained from SIMS, we still do not know how the clusters aggregate after the peroxo bond breaking and how preferential speciation occurs during this process.

More advanced techniques with the capability of charactering amorphous films and sub-nm clusters may help us achieve a deeper understanding of the above issues.

References

1. Vasilopoulou, M.; Boyatzis, S.; Raptis, I.; Dimotikalli, D.; Argitis, P., Evaluation of poly(hydroxyethyl methacrylate) imaging chemistries for micropatterning applications. *Journal of Materials Chemistry* **2004,** 14, (22), 3312-3320.
2. Lee, E. H.; Rao, G. R.; Mansur, L. K., LET effect on cross-linking and scission mechanisms of PMMA during irradiation. *Radiation Physics and Chemistry* **1999,** 55, (3), 293-305.
3. Zhao, M., Exploration of non-chemically amplified resists based on chain-scission mechanism for 193 nm lithography. **2010**.
4. Caster, A. G.; Kowarik, S.; Schwartzberg, A. M.; Nicolet, O.; Lim, S. H.; Leone, S. R., Observing hydrogen silsesquioxane cross-linking with broadband CARS. *Journal of Raman Spectroscopy* **2009,** 40, (7), 770-774.
5. Thompson, L.; Ballantyne, J.; Feit, E., Molecular parameters and lithographic performance of poly (glycidyl methacrylate ‐ co ‐ ethyl acrylate): A negative electron resist. *Journal of Vacuum Science & Technology* **1975,** 12, (6), 1280-1283.
6. Barber, R. L.; Ghantasala, M. K.; Divan, R.; Mancini, D. C.; Harvey, E. C., Study of stress and adhesion strength in SU-8 resist layers on silicon substrate with different seed layers. *Journal of Micro-Nanolithography Mems and Moems* **2007,** 6, (3).
7. Warren, B. E., *X-ray Diffraction*. Courier Corporation: 1969.
8. Benninghoven, A., Chemical-Analysis of Inorganic and Organic-Surfaces and Thin-Films by Static Time-of-Flight Secondary-Ion Mass-Spectrometry (Tof-Sims). *Angewandte Chemie-International Edition in English* **1994,** 33, (10), 1023-1043.
9. Oleksak, R. P.; Ruther, R. E.; Luo, F. X.; Fairley, K. C.; Decker, S. R.; Stickle, W. F.; Johnson, D. W.; Garfunkel, E. L.; Herman, G. S.; Keszler, D. A., Chemical and Structural Investigation of High-Resolution Patterning with HafSOx. *Acs Applied Materials & Interfaces* **2014,** 6, (4), 2917-2921.
10. Kim, J.; Chao, W. L.; Griedel, B.; Liang, X. G.; Lewis, M.; Hilken, D.; Olynick, D., Understanding the base development mechanism of hydrogen silsesquioxane. *Journal of Vacuum Science & Technology B* **2009,** 27, (6), 2628-2634.
11. Nam, S. W.; Rooks, M. J.; Yang, J. K. W.; Berggren, K. K.; Kim, H. M.; Lee, M. H.; Kim, K. B.; Sim, J. H.; Yoon, D. Y., Contrast enhancement behavior of hydrogen silsesquioxane in a salty developer. *Journal of Vacuum Science & Technology B* **2009,** 27, (6), 2635-2639.
12. Vu, M. Allred-Rochow Electronegativity. http://chemwiki.ucdavis.edu/Physical_Chemistry/Physical_Properties_of_Matter/Atomic_and_Molecular_Properties/Electronegativity/Allred-Rochow_Electronegativity

Chapter 5：Low energy electron exposure on HafSOx resists

5.1 Introduction

As discussed in Chapter 1, EUV lithography is currently the most promising lithographic technique available to be used in the upcoming sub-10nm device fabrication. Finding the optimal resists compatible with EUV lithography and subsequent processing remains a major challenge. **Figure 5.1** overviews three possible resists (organic CARs, HSQ and HafSOx) and compares them based on a few key operational parameters: LER, sensitivity, and resolution.

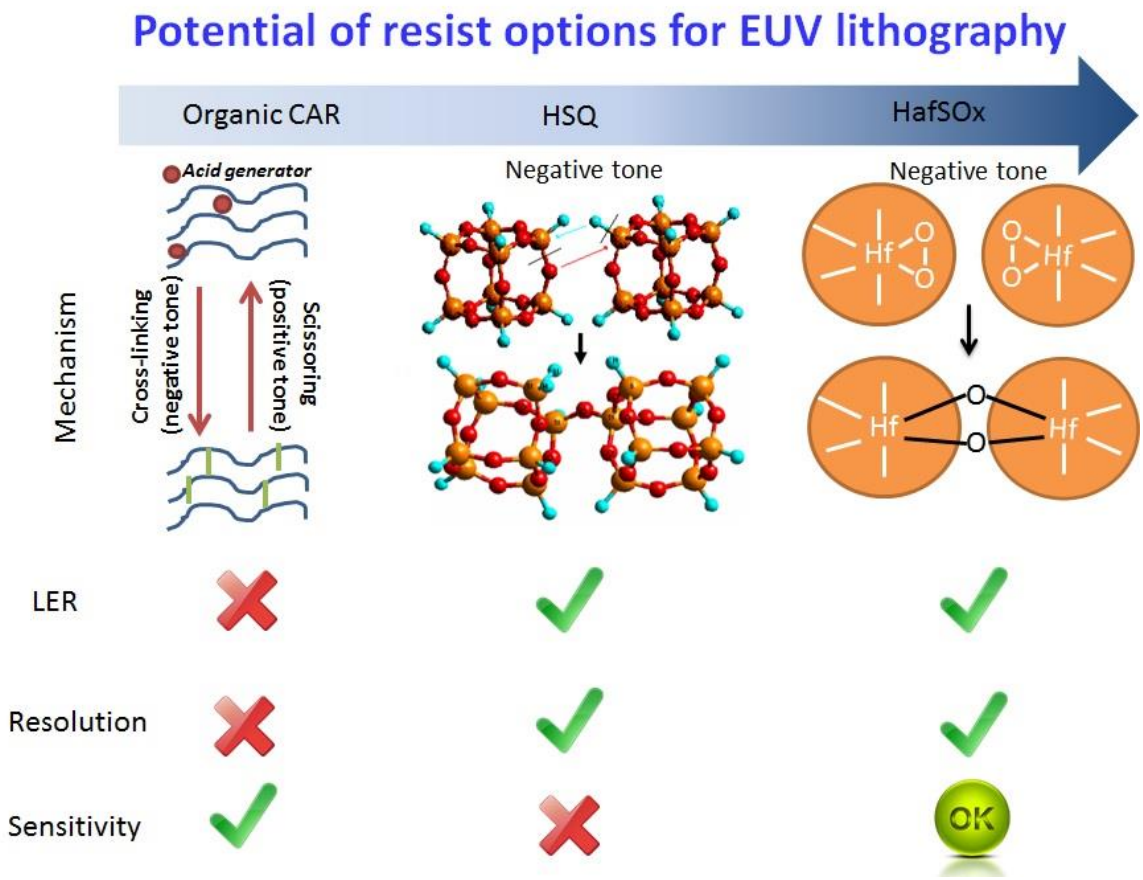

Figure 5.1 An overview the potential of various resists applied in the EUV lithography

HafSOx and other related metal-cluster-based (e.g. Sn-organic resist[1]) resists stand as a genre of promising EUV resists. This unique resist design benefits from the small size of the monomer nanoclusters compared with the bulky organic polymers, which leads to a better LER and resolution, and the incorporation of photon sensitive species (e.g. peroxide, carboxylate) increase the sensitivity. To fully optimize their performance in EUV

lithography, the detailed mechanisms ranging from EUV photon absorption, ionization, secondary electron production, molecular excitation (and possibly chemistry), and finally thermalization should be investigated and understood. **Figure 5.2** offers a schematic mechanism of the process. A 13.4 nm (~93 eV) EUV photon came into the HafSOx film and is first absorbed by the Hf atoms in the clusters followed by ionization, which produces a primary electron carrying most of the energy (~80-90 eV) of the EUV photon. The high energy primary electron then loses its energy as it scatters, during which more secondary electrons with lower energy (<15 eV) are produced. We believe is that the low energy secondary electrons finally interact with the system in a number of ways (including auto-detachment, associative attachment, or dissociative attachment following the electron attachment)[2] with peroxo bonds chelated with Hf atoms, and initiates the chemistry that results in a change in bonding and system solubility.

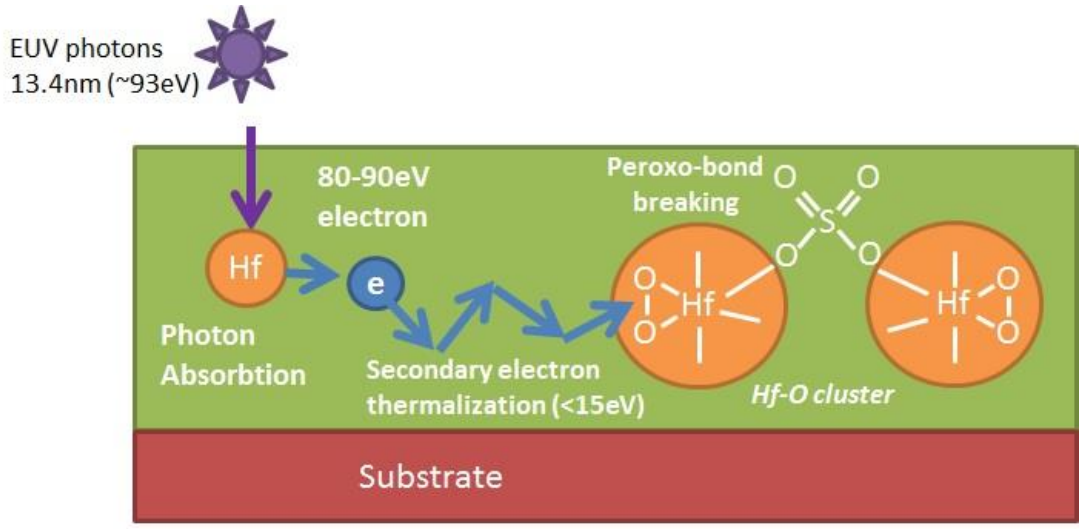

Figure 5.2 A model of EUV photon absorption, secondary electron production, and interaction of secondary electronics with the HafSOx film.

Traditional organic resists, still used in current DUV lithography when modified by the addition of photo acid generators, has lost its old advantage in terms of sensitivity because of the order of magnitude lower EUV photon absorption cross section, as exhibited in the **Figure 5.3**, in the photon induced ionization step. Moreover, based on this figure, tin cluster based resists, by taking advantage of one of the largest EUV photon absorption cross sections, may eventually exhibit excellent sensitivity, above that of other metal oxide resists, after proper optimization.

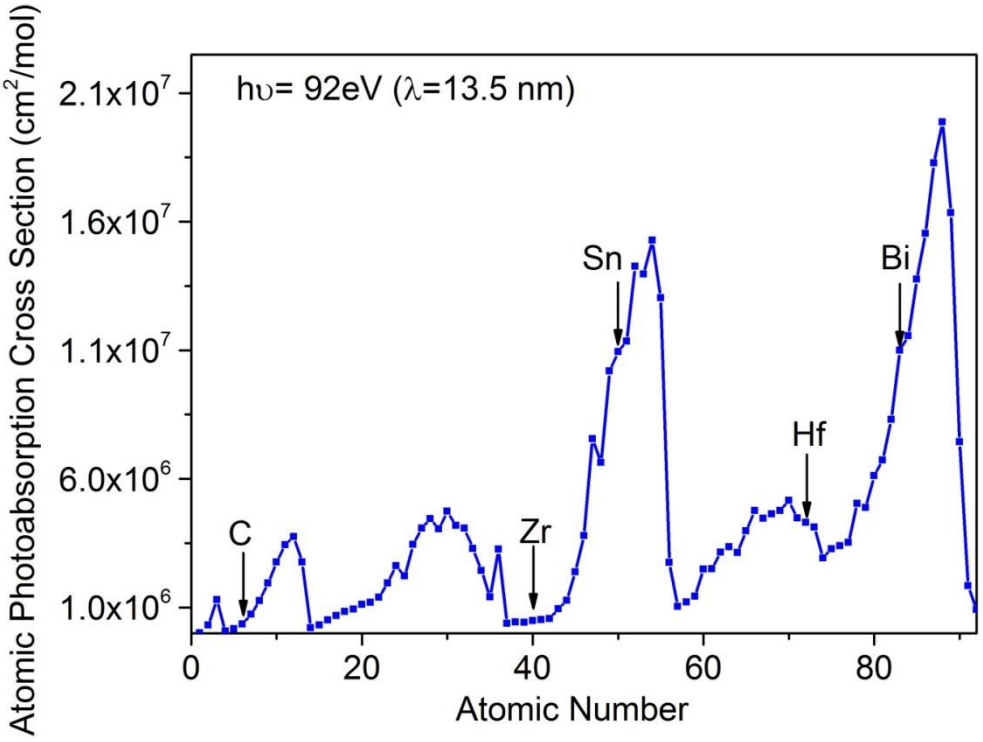

Figure 5.3 A chart of the EUV photon-absorption cross section for various elements[3].

In this study, we mainly focused on one particular mechanistic step in which the low energy electrons diffuse and interact with the clusters and activate the region presumably close to the place they are formed. **Figure 5.4** exhibits a chart of the inelastic mean free path, a parameter of the distance an electron can travel on average in a solid film before scattering and losing energy, of electrons with various energies. We note that the total path travelled is more complex than the mean free path, as scattering

and diffusion of electrons as they lower their energy is a complex process. In the high energy (>50 eV) range, electrons with a higher energy travel farther at a moderate slope. However, when the energy of an electron is below the threshold value (of ~50 eV), its mean free path increases drastically given a continuing decrease in energy. And the electrons start to diffuse to a distance of more than 1 nm with <15 eV energy[4]. Therefore, the large number of low energy secondary electrons, with relatively large inelastic mean free paths, are likely the main species in the film that are responsible to activate the region of the resist under the mask upon EUV absorption.

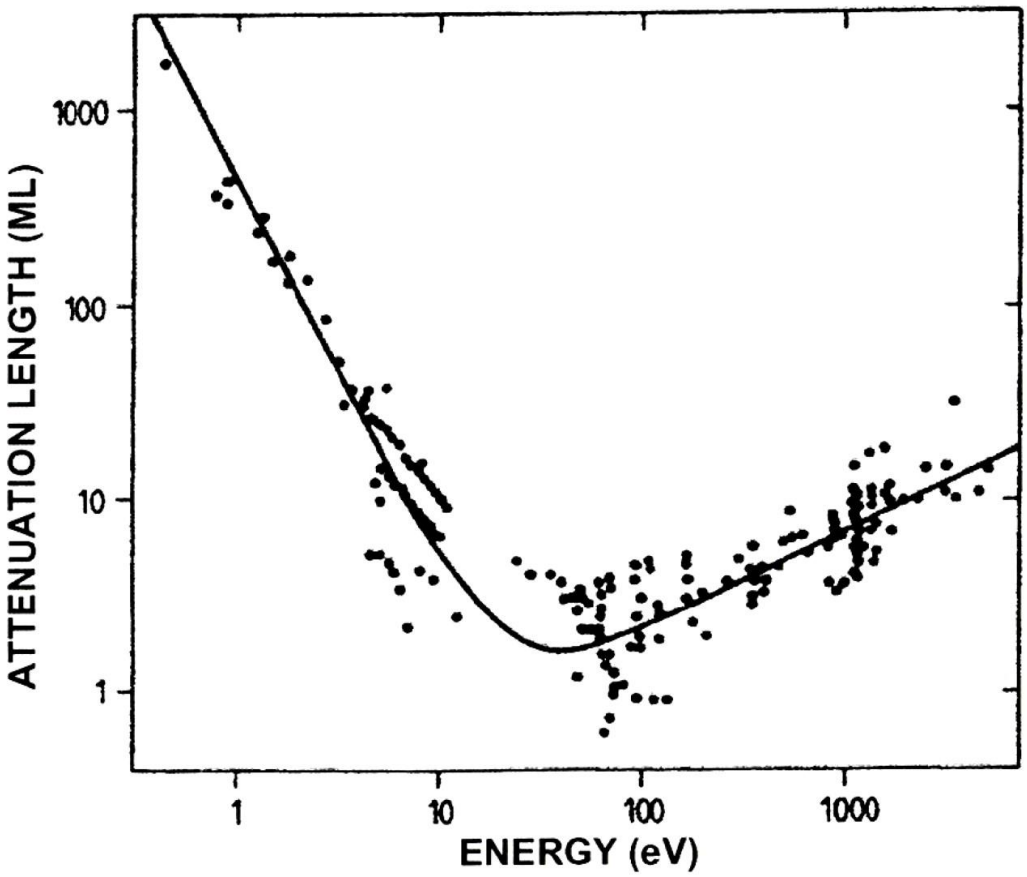

Figure 5.4 The inelastic mean free path for electrons with different energies[5]

In this study, to investigate the role that low energy electrons play in the EUV photochemistry process, we designed and set up a chamber equipped with a low energy electron gun to shoot the HafSOx sample with low energy electrons to mimic the process of electron-material interaction that happens after EUV photon ionization in the film. Moreover, some theoretical simulation work was done to help us achieve a better understanding of the experimental data.

5.2 Experimental Section

Chamber setup

A vacuum chamber was designed and assembled according to **Figure 5.5**. It has five main components: the vacuum system, the ion gauge, the sample holder, a low energy electron gun, and a voltage control system. The main chamber was pumped by a turbomolecular pump backed by a regular mechanical pump. The chamber pressure was controlled below $2*10^{-6}$ torr for the electron exposure. The sample holder was made from stainless steel and double side tape was usually used between the sample holder and the sample to achieve strong mechanical connectivity and electrical conductivity. A hot filament ionization gauge was used to monitor the pressure change (10^{-3}-10^{-9} Torr) inside the chamber during the conventional operation with a working turbomolecular pump. Finally, for the low energy electron gun, a few filaments were tried and thoriated iridium was chosen for higher electron emitting efficiency, less outgassing, and lower electron energy distribution as compared with the conventional tungsten filament[6-9]. Other than the choice of the filament material, a metallic cap with a center hole, was biased positively to help extract and

focus the electrons. The pictures of the real parts of the chamber are exhibited in **Figure 5.6**.

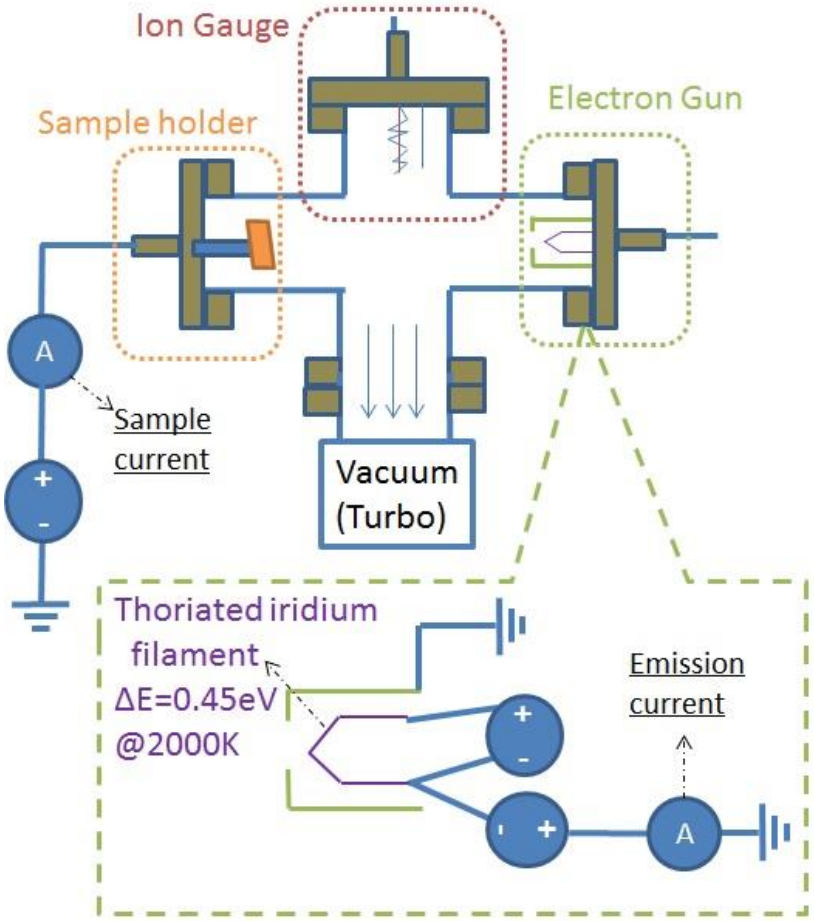

Figure 5.5 The scheme of the low energy electron exposure system setup

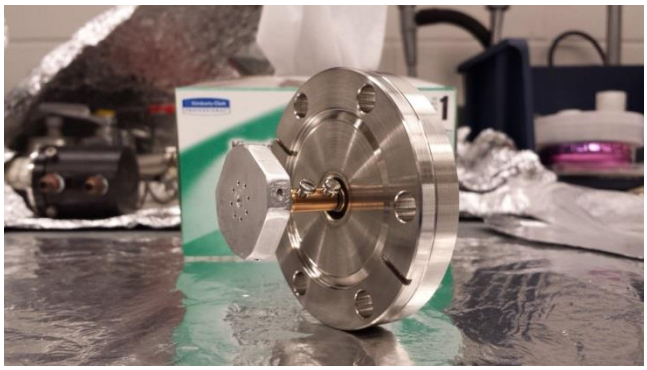

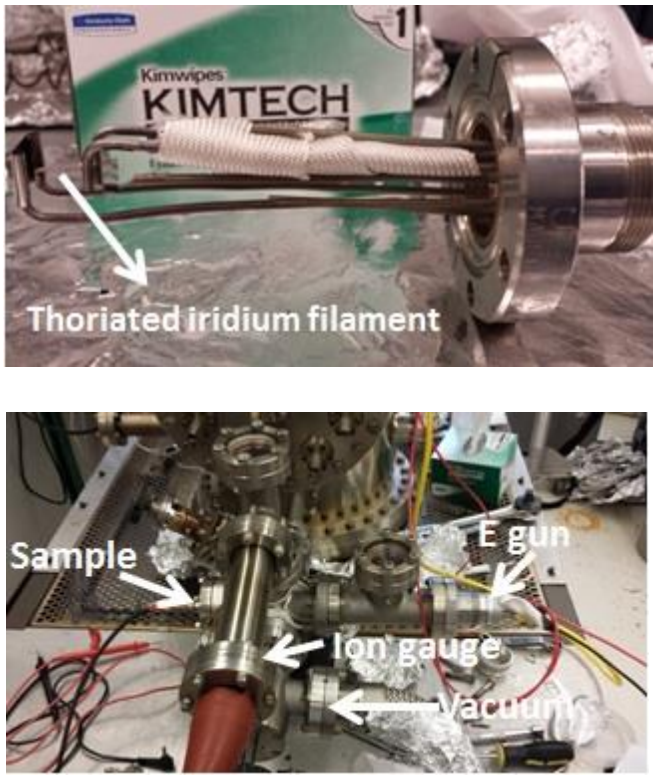

Figure 5.6 Images of the real (top) sample holder, (middle) electron gun and (bottom) the chamber.

CASINO Software

The simulation software CASINO[10-12] **(**monte *CA*rlo *SI*mulation of electro*N*trajectory in s*O*lids), coded by a group of scientists at the Université de Sherbrooke, was employed to perform the simulation of low energy electron trajectories in the HafSOx film. For the simulation purpose, a film structure of 10 nm HafSOx, 2 nm native silicon oxide and a Si substrate was modeled. A normal incident beam of 2000 electrons with a

diameter of 10 nanometers was simulated with a primary electron energy ranging from 10 eV to 100 eV and a minimum detectable energy ranging from 2 eV to 10 eV when setting up the microscope and simulation properties. Finally, a few physical models were selected prior to the beginning of the simulation. The Mott[13] elastic following the Browning[14-16] or Drouin and Gauvin[17, 18] methods. An empirical approach proposed by Casnati[19] for the effective ionization cross-section and the energy loss implementation is based on Joy and Luo's formula[20, 21].

5.3 Results and Discussion

Once completing the chamber assembly, we started our low energy electron mechanistic study by attempting to figure out what was the minimum energy required to activate the HafSOx since a large amount of low energy secondary electrons, with various energies, would be produced once initiated by 93 eV EUV photons and what efficiency, in terms of electron dose, is needed in order to fully activate the film.

However, to achieve electrons with a certain energy is not as easy as simply applying a voltage equal to the target energy, in V, between the sample holder and filament. Given an energy diagram as shown in **Figure 5.7**, even with the same potential at both ends, the electrons emitted off

from the filament will still have an energy spread of ΔE, and a non-zero energy, because of work function difference between the sample surface and the filament. Therefore, the energy of the electrons impinging upon the sample surface has to be properly calibrated.

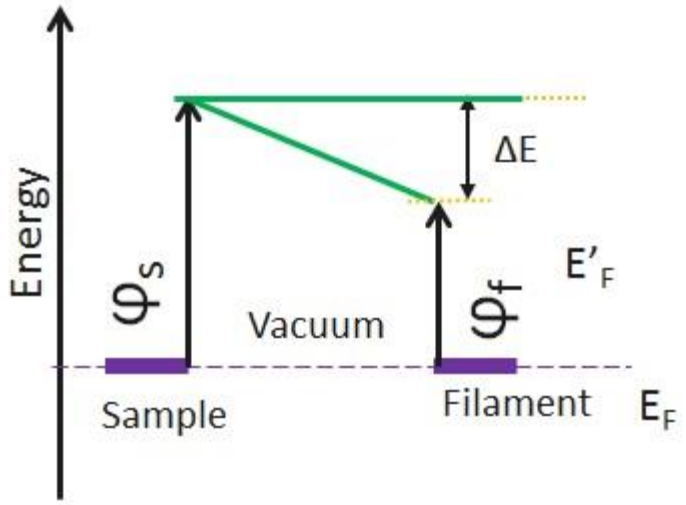

Figure 5.7 An example of an energy diagram between the sample and filament**.**

As exhibited in **Figure 5.8**, the energy calibration was conducted by consecutively changing the potential difference between sample and the filament at various emission currents. The collected sample current was plotted against the potential difference between two ends. After overlaying the sample current curves on various emission currents, we found those curves generally can be divided into two regions: the nearly zero sample

current region and emission-current-dependent sample current region. In the first region, the emitted electrons were blocked by the sample-filament work function difference thus, no matter how much emission electrons there were, no electron can finally reach the sample surface. However, in the second region, because the applied potential helped the emitted electrons to overcome the original unfavorable work function difference, the electrons can eventually get to the surface of the sample. Therefore, a higher emission current will lead to higher collected sample current at the same potential difference. Finally, by extrapolating two fitted lines of those two regions, we would get a roughly consistent intersection point, at which we determined the electrons we collected are with the energy of 0 eV and all other energies would be accordingly calibrated based on this point.

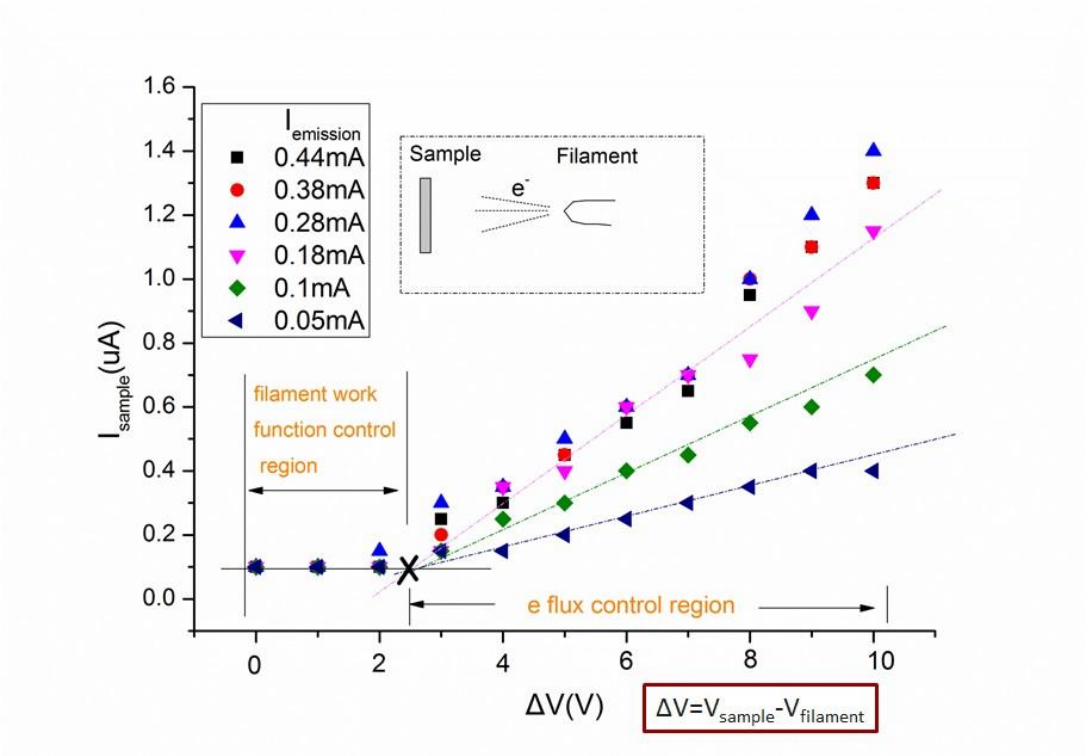

Figure 5.8 The electron energy calibration: experimental design and data analysis

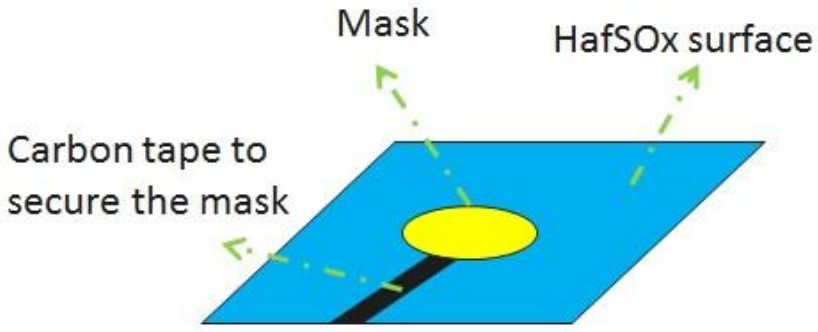

Figure 5.9 A scheme of the sample design for the experiment exploring the minimum HafSOx activation energy by electrons

Other than the energy calibration, the minimum activation energy experiment was conducted with an additional sample design like what was exhibited in **Figure 5.9**. A round metal disk was placed on the surface of the HafSOx film in order to provide a good contrast between the exposed and unexposed area. The electron conductive carbon tape will not only physically fix the metal mask but also get rid of the possibility of trapped surface charges produced during the low energy electron bombarding in the experiment.

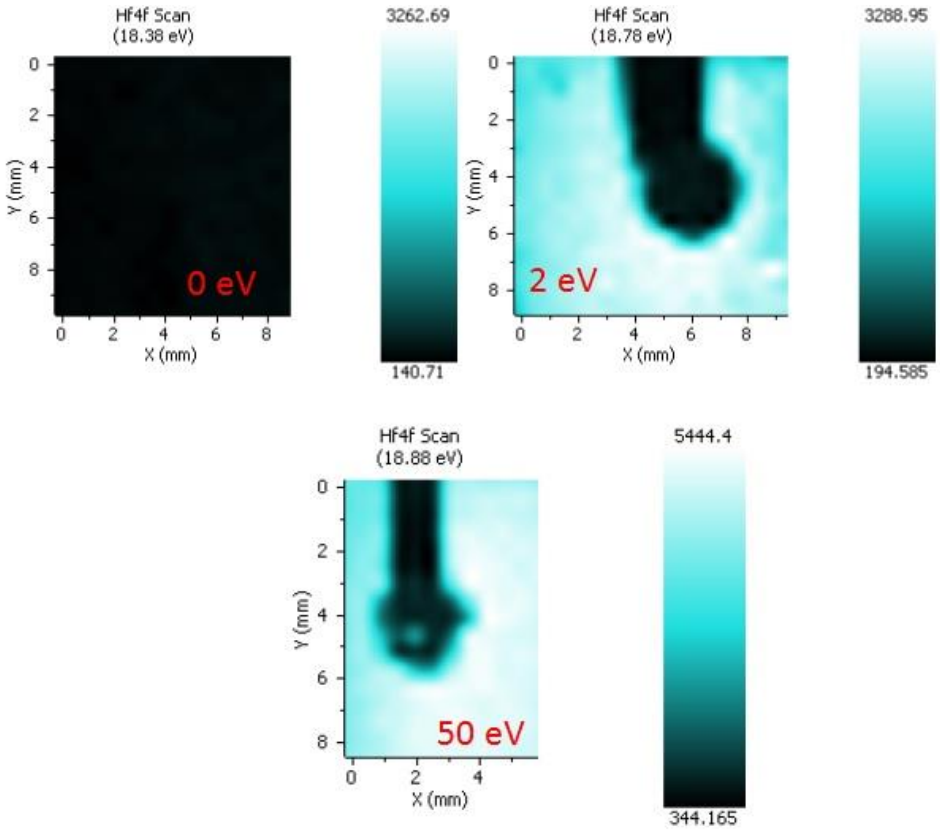

Figure 5.10 The XPS Hf mapping of (top, left) the no electron control film, (top, right) 2 eV electrons exposed film and (bottom) 50 eV electrons exposed film after 25% TMAH development.

After the low energy electron exposure, all of the films were developed in a 25% TMAH solution followed by XPS mapping of the different elements. **Figure 5.10** exhibits the Hf mapping data on various samples. The image labeled as 0 eV was obtained from the control film receiving no electron exposure but had the same filament current as the other samples. We found basically there was no Hf remained on the exposed area of the control sample, which indicated that, without electrons, the photons and thermal energy emitted from the filament would not chemically activate the film. Then, a series of samples were tested to be exposed with electrons with various energies, ranging from 2 eV to 100 eV, and the XPS Hf mapping data of 2 eV and 50 eV electron exposed film was shown in this figure. On both samples, we found the exposed area revealed a large amount of Hf whereas the mask covered region had no Hf, implying that even electrons with energy as low as 2 eV activated the HafSOx resist.

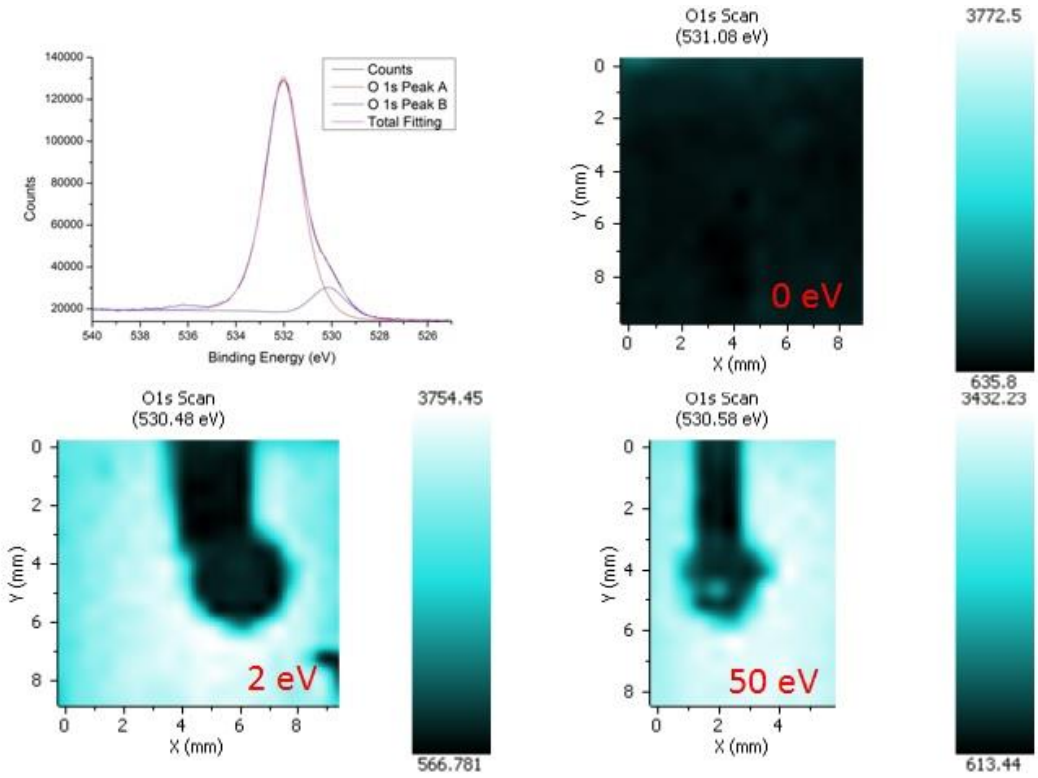

Figure 5.11 (top left) An example of a XPS O1s peak fitting and XPS O component, at lower binding energy, mapping of (top, right) the no electron control film, (bottom left) 2 eV electrons exposed film and (bottom, right) 50 eV electrons exposed film after 25% TMAH development.

Other than the XPS Hf 4f mapping, the O1s mapping was conducted as well to monitor the film O changed upon electron exposure. As discussed in the previous chapters and in the **Figure 5.11**, we assigned the O1s component at the lower binding energy (~ 530-531 eV) to the O in the Hf-

O-Hf network formed after radiation activation. In **Figure 5.11**, we can see that the Hf-O-Hf network was formed on the same place, the low energy electron exposed area where the Hf remained.

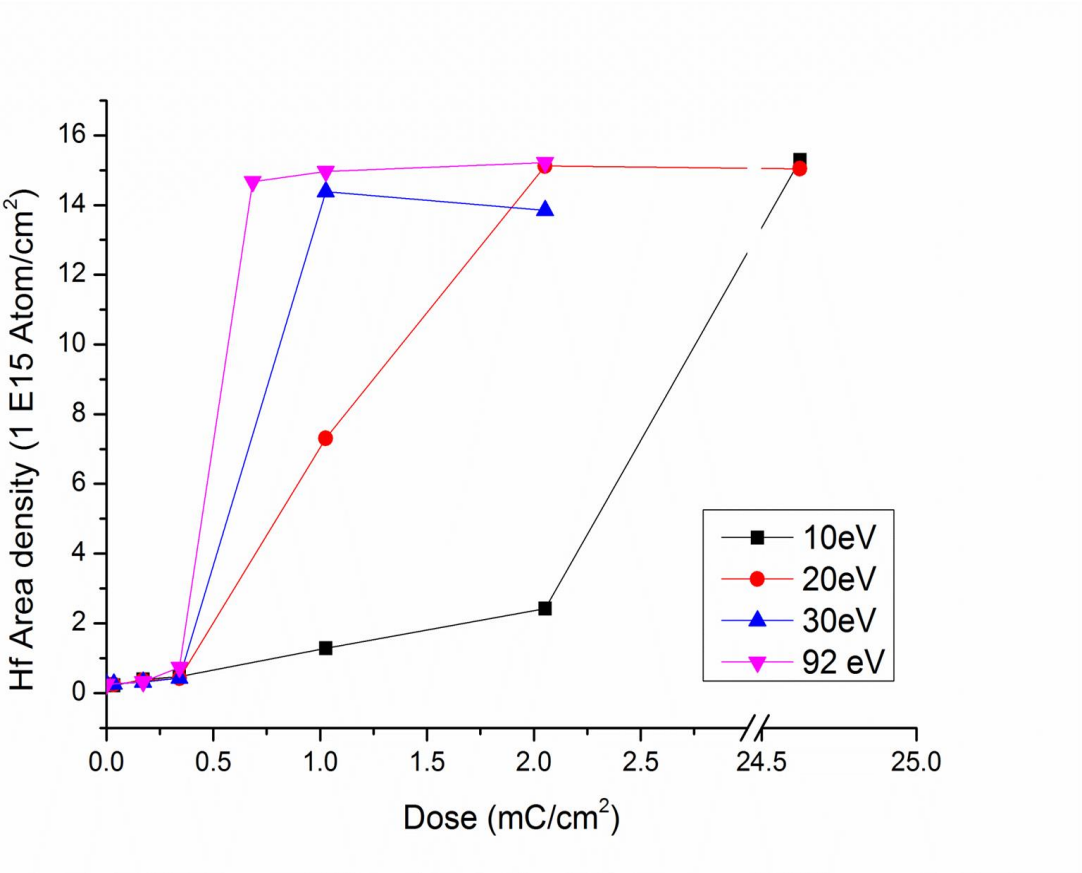

Figure 5.12 The contrast curves for HafSOx films exposed by electrons with various energies.

Knowing the minimum activation energy, we also tried to figure out how efficient those low energy electrons were, in terms of the HafSOx activation. Therefore, for various electron energies, we changes the dose of

the electrons, by accordingly changing the exposure time at the same sample current, and tested the film thicknesses at various doses characterized by RBS.

As shown in **Figure 5.12**, we found that in the low energy region (<100 eV), higher energy electrons would lead to a higher sensitivity, which probably caused by a different amount of secondary electrons, a key role in activating resists, produced by primary electrons with different energies. As shown in **Figure 5.13**, a typical secondary electron yield curve will achieve a maximum yield at certain primary incident energy. Beyond and below that specific maximum yield energy, a lower yield will be expected. In addition, in the region below the energy threshold, the secondary electron yield usually dropped more dramatically against primary incident energy than what happened in the region beyond the threshold.

Knowing above secondary electron yield properties and looking back to our data, we deduced that all those energies below 100 eV have a property that higher primary incident energy leads to higher sensitivity, thus more secondary electrons. So 100 eV is below the E_m of the HafSOx system. The drastic sensitivity between 10 eV and 20 eV may be cause by

the sharp drop of secondary electron yield when the primary incident energy is too low, such as below the E_I.

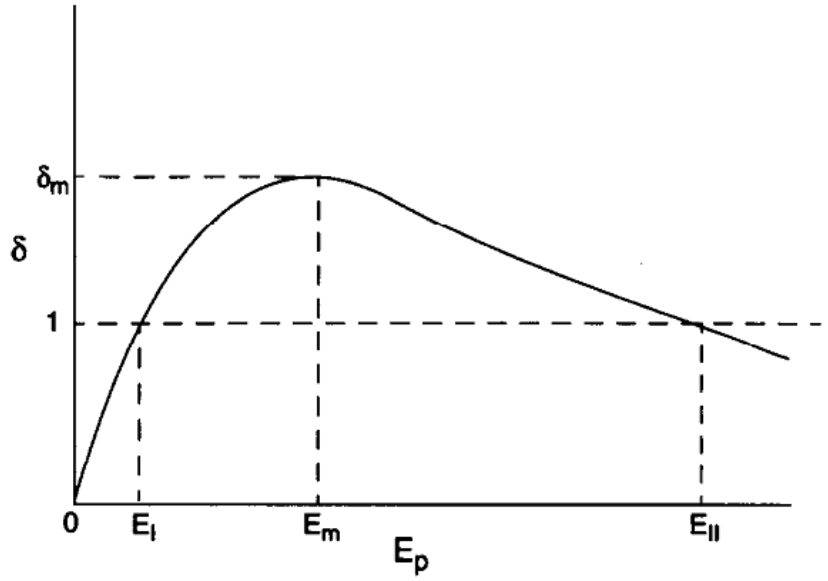

Figure 5.13 A typical example of secondary electron yield against the primary incident energy (E_p). E.g. for Mg, the usually reported E_I=20 eV, E_m=950 eV and E_{II}= 10 keV.[22]

Besides the contrast curve comparison among those low energy electrons, we also attempted to compare them with the conventional high energy electron sources used in the e-beam lithography exposure. As exhibited in **Figure 5.14**, we found the 30 keV electrons have a higher sensitivity in terms of the HafSOx resist activation possibly due to the production of more secondary electrons. However, their contrast curves did

not differentiate with each other as much as their primary incident energies did. This may be inferred from the secondary electron yield curve in which two totally different primary incident energies may lead to very similar secondary electron yields.

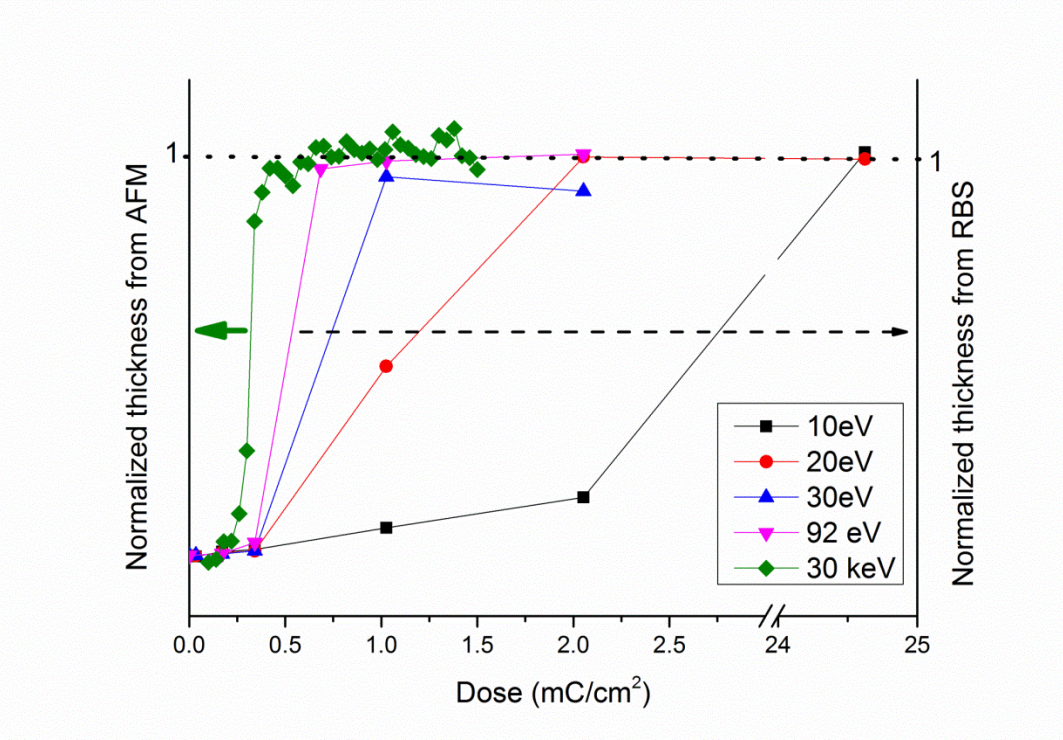

Figure 5.14 The contrast curve comparison between high energy (30 keV) and low energy (<100 eV) electron exposed films with the thickness characterized by AFM and RBS respectively.

In addition, we also conducted XPS measurement on every exposed and developed samples. As shown in **Figure 5.15**, we surprisingly found that all the HafSOx films with 100% activation, at which the thickness of the film

after exposure and development equals the original one, by the low energy electrons had a substantial S residue in the film, which had never been observed before in the high energy electron and photon exposed films.

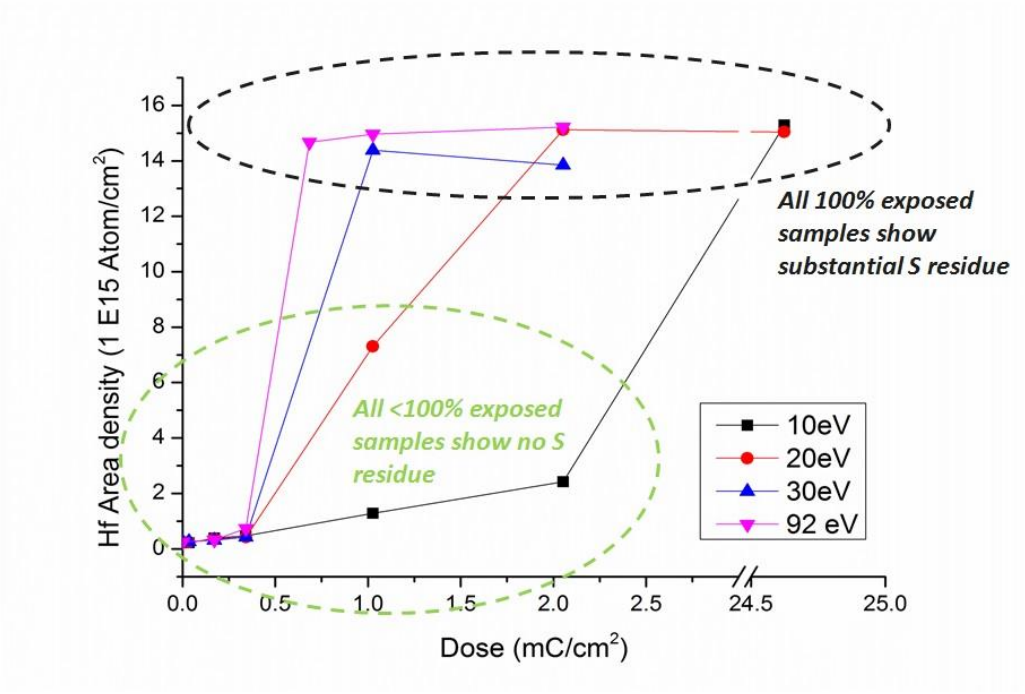

Figure 5.15 The substantial S residue was found for all 100% exposed samples by the low energy electron exposure

To investigate the S residue, the XPS S2p peaks of samples exposed by electrons with various energies were compared and the data was summarized in **Figure 5.16**. We found that compared with the as-deposit films, the S from the exposed and developed films didn't experience a noticeable peak shift indicating its oxidation states did not changed during this process. The possible reason may be that the subtle film structure

change happened during low energy electron exposure trapped a number of sulfate tightly, which therefore cannot escaped from the film in the development solution. But we do not have solid evidence for this currently.

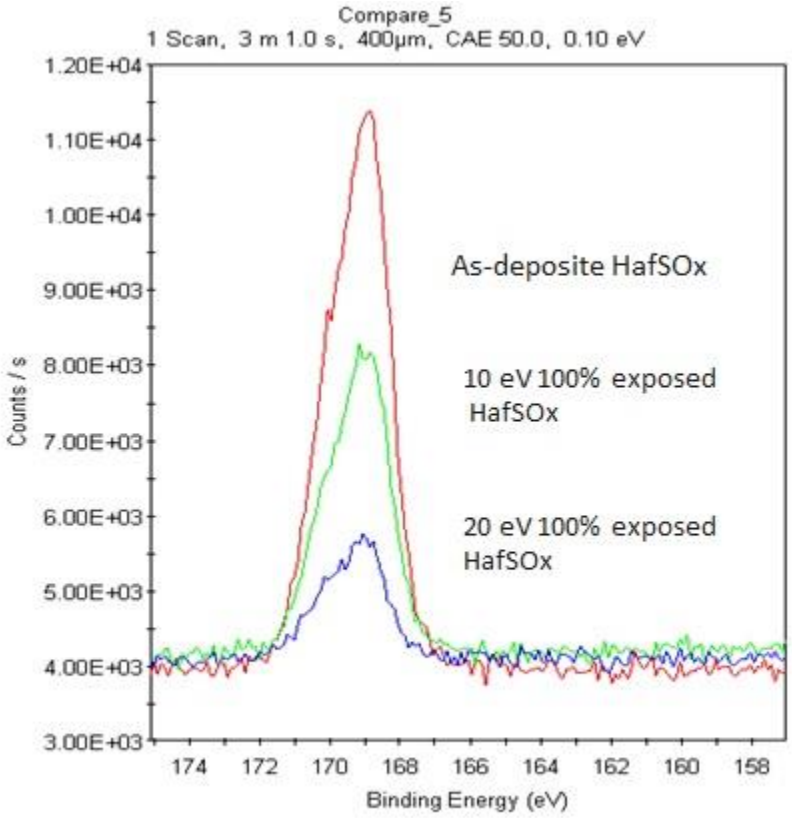

Figure 5.16 The XPS S2p peak comparison for as-deposit and low energy electron exposed and developed HafSOx films

As a supplement to the experimental section and in order to have a better understanding, we conducted some Monte Carlo simulation of low energy electron trajectories in the HafSOx films with the help of the CASINO software. As exhibited in **Figure 5.17**, we set up a three layer model and

simulated first, with 2000 electrons, the energy of 100 eV. If we set the minimum simulation energy as 5 eV, which meant only electrons with energy above 5eV would be simulated and shown in the graph, we found that those electrons above 5 eV only penetrated inside the films with the maximum depth of 3 nm. Nevertheless, in the experiment, all of our films had a thickness between 10 to 20 nm. The 2eV-92 eV electrons activated the whole film with no problem. Therefore the simulation cannot match what we saw in the experiment.

Then we changed the minimum simulation energy to a lower energy to 2eV also shown in **Figure 5.17**. We found the electrons with the energy ranging from 2eV to 5eV eventually penetrated through the 10 nm HafSOx film and even into the underneath SiO_2 and Si layers. This resulted from their high mean free path at the very low energy region, which, from another perspective, emphasized the key role of the low energy secondary electrons that played in the radiation chemistry and the film solubility change during the lithography process.

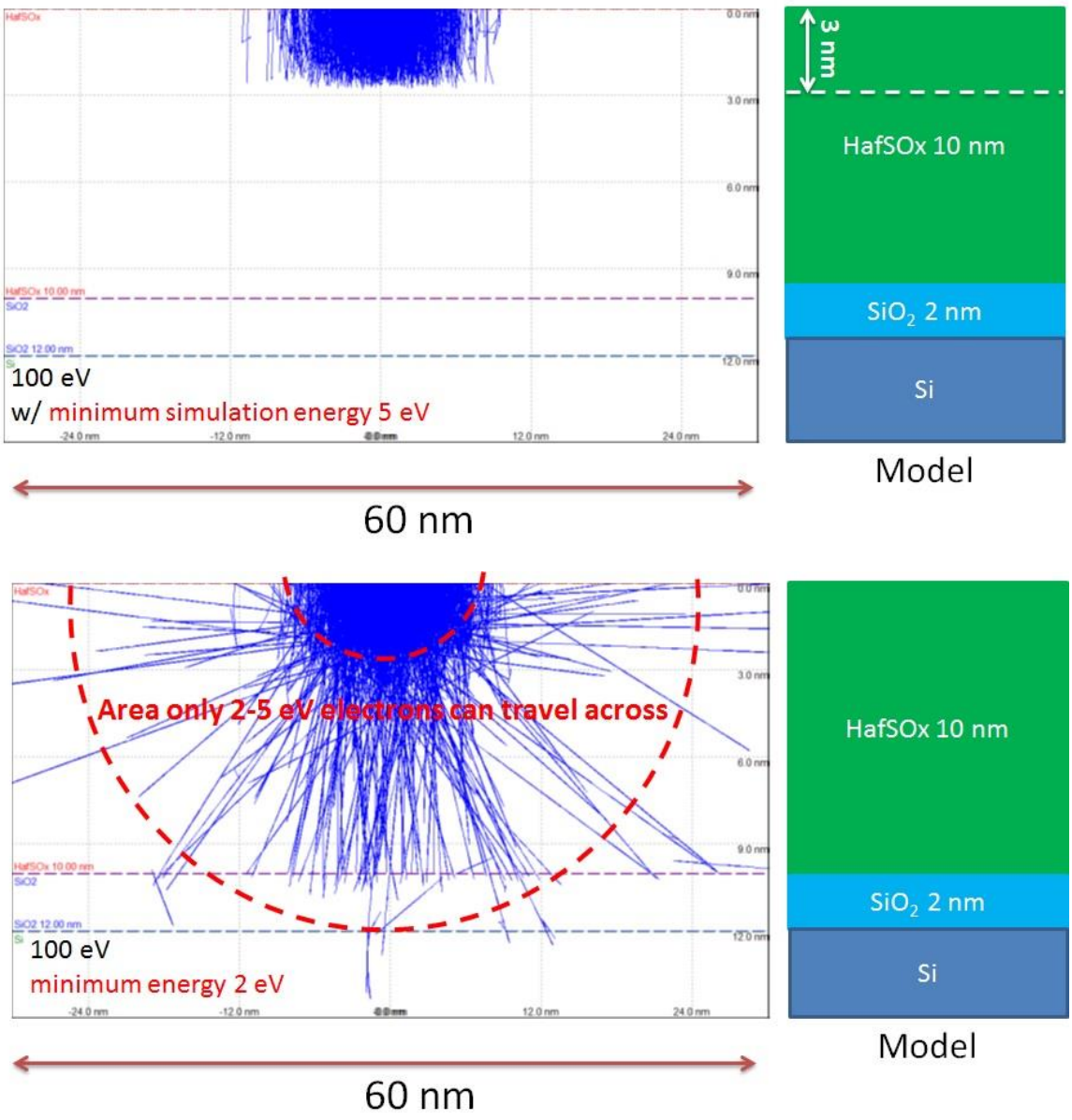

Figure 5.17 The CASINO simulation on HafSOx film exposed by 100 eV electrons with minimum simulation energy 5 eV (top) and 2 eV (bottom)

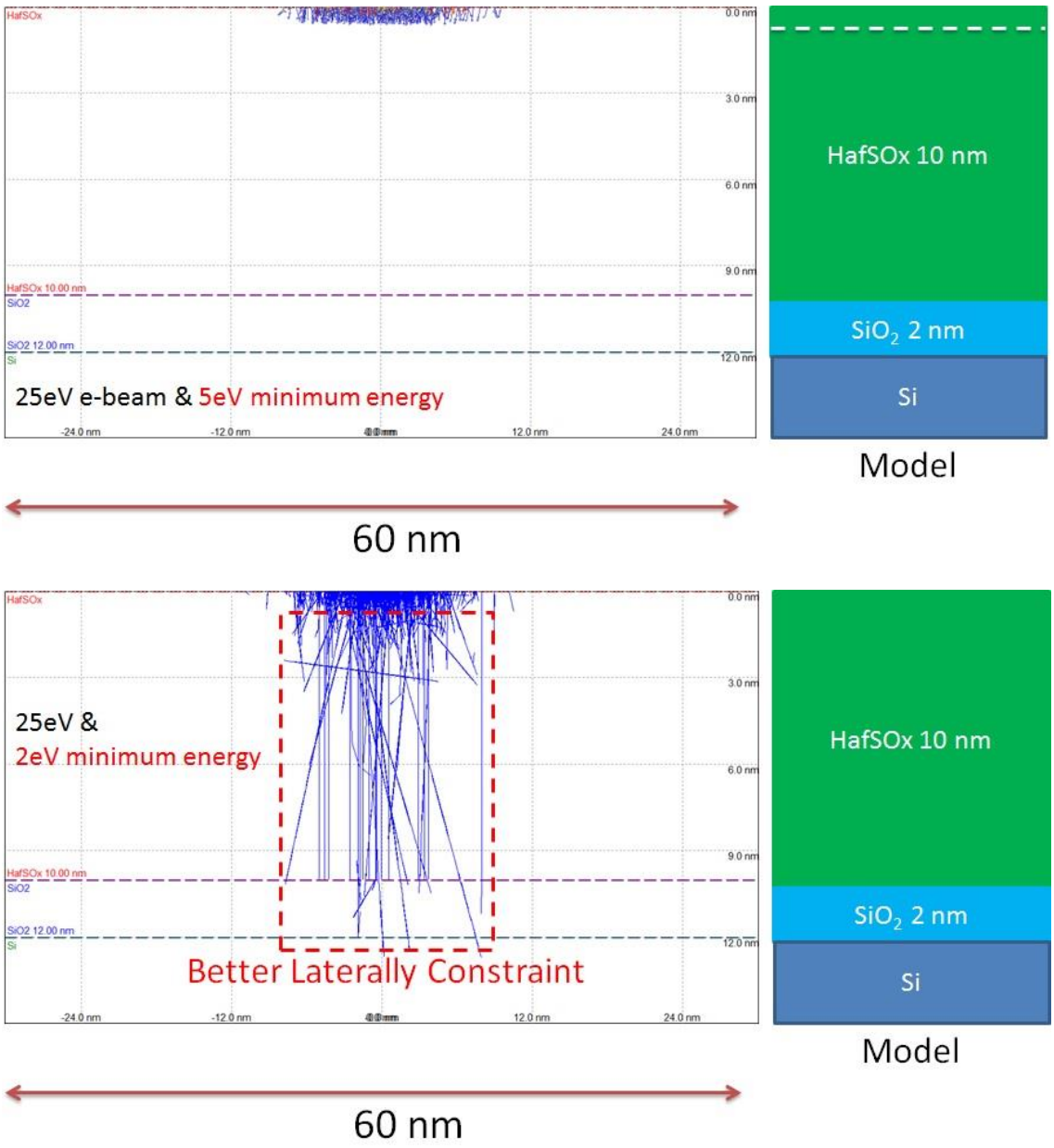

Figure 5.18 The CASINO simulation on HafSOx film exposed by 100 eV electrons with minimum simulation energy 5 eV (top) and 2 eV (bottom)

With the 100 eV electrons simulated, we also tried a lower energy simulation such as 25 eV electrons, exhibited in **Figure 5.18**. Similarly, we can also see that the low energy electrons (2-5eV) were the main species traveling through the HafSOx film that to activate most of the exposed part. A subtle difference spotted is that 2-5 eV secondary electrons originated from the 25 eV electrons had a better lateral constraint compared with 100 eV electrons, which further caused a better LER and smaller critical dimension, if we patterned the films on nanometer scale with 25 eV electrons. But in reality it is hard to implement this proposed experiment in our home-built system due to the lack of lens to well focus the electron beam.

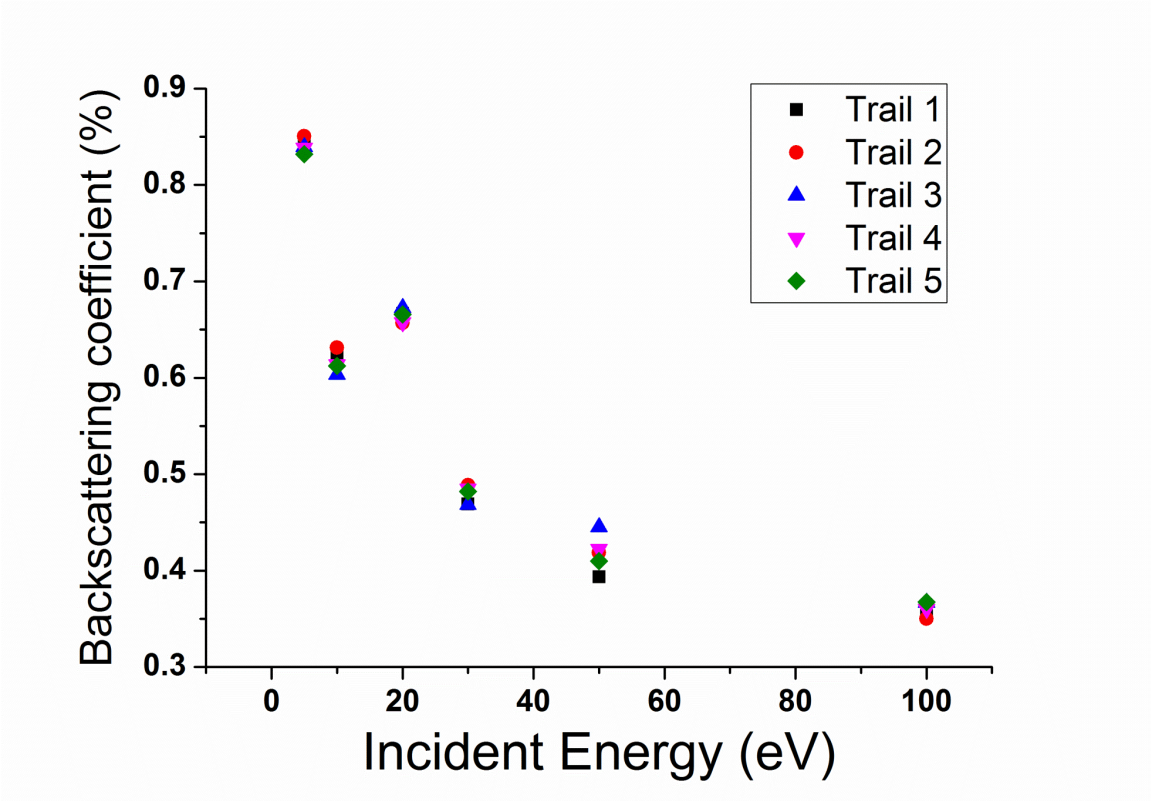

Figure 5.19 The electron backscattering coefficient variance according to different incident energy

Additionally, during the simulation, another important parameter we obtained was the electron backscattering coefficient, summarized in **Figure 5.19**. We found in the low energy regime (<100 eV), the simulated backscattering coefficient skyrocketed with the decrease of the primary incident energy, which had also been reported in literature[23, 24] for the low energy electrons.

5.4 Summary

In summary, after designing and building a low energy electron exposure system, we obtained the capability to mechanistically investigate the role of low energy electrons in the activation of HafSOx films. On one hand, we tested the minimum energy needed for film activation and it turned out that, surprisingly, low energy electrons (~ 2eV) did the job well, which proved that the low energy secondary electrons produced after EUV photon exposure have the ability to initiate the radiation chemistry. On the other hand, we tested the patterning sensitivity of the HafSOx films to the electrons with various energies, which may result from a different amount of low energy secondary electrons (<15 eV) produced for different primary incident energies. Finally, a Monte Carlo simulation was conducted. We found another important role of low energy secondary electrons (2-5 eV), which enabled the resist bulk activation benefiting from their large mean free path.

In conclusion, through this study, we achieved a better understanding, with both experimental and theoretical methods, of the role that low energy secondary electrons played in the resist activation process.

References

1. Cardineau, B.; Del Re, R.; Al-Mashat, H.; Marnell, M.; Vockenhuber, M.; Ekinci, Y.; Sarma, C.; Neisser, M.; Freedman, D. A.; Brainard, R. L., EUV Resists based on Tin-Oxo Clusters. *Advances in Patterning Materials and Processes Xxxi* **2014,** 9051.
2. Arumainayagam, C. R.; Lee, H. L.; Nelson, R. B.; Haines, D. R.; Gunawardane, R. P., Low-energy electron-induced reactions in condensed matter. *Surface Science Reports* **2010,** 65, (1), 1-44.
3. Stowers, J., Imageable Oxides: New Solutions for Resist. In rev3.pptx, S.-I. E. S., Ed. 2010 International Symposium on Extreme Ultraviolet Lithography, 2010.
4. Seah, M.; Dench, W., Quantitative electron spectroscopy of surfaces. *Surface and interface analysis* **1979,** 1, (1), 2-11.
5. Duke, C. B., The birth and evolution of surface science: Child of the union of science and technology. *Proceedings of the National Academy of Sciences of the United States of America* **2003,** 100, (7), 3858-3864.
6. Samsonov, G., Handbook of thermionic properties. In Plenum Data Division, New York: 1966.
7. Gear, P., The choice of cathode material in a hot cathode ionization gauge. *Vacuum* **1976,** 26, (1), 3-10.
8. Jenkins, R., A review of thermionic cathodes. *Vacuum* **1969,** 19, (8), 353-359.
9. Bayard-Alpert Gauge Filaments: Tungsten or Thoria? . http://www.thinksrs.com/downloads/PDFs/ApplicationNotes/IG1filamentsapp.pdf
10. Drouin, D.; Couture, A. R.; Joly, D.; Tastet, X.; Aimez, V.; Gauvin, R., CASINO V2. 42-A fast and easy-to-use modeling tool for scanning electron microscopy and microanalysis users. *Scanning* **2007,** 29, (3), 92-101.
11. Demers, H.; Poirier-Demers, N.; Couture, A. R.; Joly, D.; Guilmain, M.; de Jonge, N.; Drouin, D., Three-Dimensional Electron Microscopy Simulation with the CASINO Monte Carlo Software. *Scanning* **2011,** 33, (3), 135-146.
12. Casino: monte carlo simulation of electron trajectory in solids. http://www.gel.usherbrooke.ca/casino/index.html
13. Mott, N. F., The exclusion principle and aperiodic systems. *Proceedings of the Royal Society of London. Series A, Containing Papers of a Mathematical and Physical Character* **1929**, 222-230.
14. Browning, R.; Li, T. Z.; Chui, B.; Ye, J.; Pease, R. F. W.; Czyzewski, Z.; Joy, D. C., Low-Energy-Electron Atom Elastic-Scattering Cross-Sections from 0.1-30 Kev. *Scanning* **1995,** 17, (4), 250-253.
15. Browning, R.; Li, T. Z.; Chui, B.; Ye, J.; Pease, R. F. W.; Czyzewski, Z.; Joy, D. C., Empirical Forms for the Electron-Atom Elastic-Scattering Cross-Sections from 0.1 to 30 Kev. *Journal of Applied Physics* **1994,** 76, (4), 2016-2022.
16. Browning, R.; Eimori, T.; Traut, E. P.; Chui, B.; Pease, R. F. W., An Elastic Cross-Section Model for Use with Monte-Carlo Simulations of Low-Energy Electron-Scattering from High Atomic-Number Targets. *Journal of Vacuum Science & Technology B* **1991,** 9, (6), 3578-3581.
17. Drouin, D.; Gauvin, R.; Joy, D. C., Computation of Polar Angle of Collisions from Partial Elastic Mott Cross-Sections. *Scanning* **1994,** 16, (2), 67-77.
18. Drouin, Computation of Polar Angle of Collisions from Partial Elastic Mott Cross-Sections (Vol 16, Pg 67, 1994). *Scanning* **1995,** 17, (3), U8-U8.

19. Casnati, E.; Tartari, A.; Baraldi, C., An Empirical-Approach to K-Shell Ionization Cross-Section by Electrons. *Journal of Physics B-Atomic Molecular and Optical Physics* **1982,** 15, (1), 155-167.
20. Villarrubia, J. S.; Ritchie, N. W. M.; Lowney, J. R., Monte Carlo modeling of secondary electron imaging in three dimensions - art. no. 65180K. *Metrology, Inspection, and Process Control for Microlithography XXI, Pts 1-3* **2007,** 6518, K5180-K5180.
21. Joy, D. C.; Luo, S., An Empirical Stopping Power Relationship for Low-Energy Electrons. *Scanning* **1989,** 11, (4), 176-180.
22. Scholtz, J. J.; Dijkkamp, D.; Schmitz, R. W. A., Secondary electron emission properties. *Philips Journal of Research* **1996,** 50, (3-4), 375-389.
23. Nikzad, S.; Smith, A. L.; Elliott, S. T.; Jones, T. J.; Tombrello, T. A.; Yu, Q., Low-energy electron detection with delta-doped CCDs. *Solid State Sensor Arrays: Development and Applications* **1997,** 3019, 241-248.
24. Dapor, M., Transport of energetic electrons in solids. *Springer Tracts in Modern Physics* **2014,** 257.

Chapter 6 : Helium Ion Beam Lithography on HafSOx films

This chapter is a modified version of a 2016 SPIE advanced lithography conference paper. The manuscript was published in the 2016 Proceedings of SPIE (doi:10.1117/12.2219239).[1]

6.1 Introduction

Semiconductor lithography, in its attempt to follow Moore's law, has proceeded through g-, h- and i-line Hg sources and deep ultraviolet (DUV) excimer lasers (e.g. KrF and ArF). It is now trying to transition to extreme ultraviolet lithography (EUVL)[2]. EUVL offers the promise of significant improvements in critical dimensions (CD) relative to current optical projection techniques and has become the most exciting technique for next generation lithographies (NGL). Unfortunately, EUVL is still facing challenges including inadequate source power, reflective photomasks issues, optical quality and durability, and resist optimization. Ion beam lithography, especially fast light ions (e.g. protons and helium ions), has received some attention due to its negligible proximity effect [3], attributed

to low lateral and back scattering relative to e-beam lithography EBL. Moreover, due to the much larger stopping power of ions [4] compared with light electrons, more energy might be expected to be deposited in the top tens of nanometers of the resist film, which may result in a significant improvement in sensitivity [5]. In 2007, Carl Zeiss SMT released the first commercial scanning helium ion microscope (SHIM) [6] making helium ion beam lithography (HIBL), in addition to SHIM, accessible to general users.

In this study, we worked on a Carl Zeiss ORION PLUS SHIM system and investigated the lithographic performance of HafSOx as a resist with HIBL. Moreover, Monte Carlo simulations have been conducted to model the helium ion interaction with the HafSOx film and to compare its behavior with what is observed in the electron beam case.

6.2 Experimental Section

Characterization techniques: Rutherford backscattering spectrometry (RBS) was performed using a2MeV He^{2+} beam source from a 1.7 MV tandem accelerator with an ion current of 2-3 nA. During the RBS measurement, the incident beam was normal to the surface, and the backscattered He ions were collected by two silicon surface barrier detectors (at ~100° and ~160° scattering angles for glancing and backscattering). Data fitting and

modeling were accomplished using the SIMNRA 6.06 software package. Films were also characterized by atomic force microscopy (AFM) using Park Systems NX-10. Measurements were done in the non-contact mode with a PPP-NCHR tip (Nanosensors, tip radius <10 nm).

Helium ion beam lithography and microscopy A Carl Zeiss ORION PLUS SHIM system, operated at 30 kV, was used for patterning and imaging. The ion beam current was usually kept below 1 pA. For the sensitivity test, 10 nm was selected as the pixel spacing while, for thin line patterns, the pixel spacing was selected in the range of 0.2 nm to 10 nm. After the helium ion exposure, the exposed films were developed in a tetramethylammonium hydroxide solution (TMAH, 25 wt. % in water) for 1 min followed by a 300 °C hard-bake for 5 mins.

Pattern analysis The LER, line width roughness (LWR), and CD were calculated from high-resolution, top-down secondary electron images of sets of five patterned lines acquired using the SHIM and following the methods recommended by the ITRS[7]. The LER was calculated as three times the standard deviation in the line edge position (average from top and bottom line edges), the LWR was calculated as three times the standard deviation in the line width, and CD was the average line width. The LER,

LWR, and CD values were calculated for each line in each set, then averaged to describe the set as a whole. The uncertainty in each measurement comes from the standard deviation of the five average measurements. Due to resolution constraints, approximately 450 nm lengths of each line were used for the calculations. The images were processed using the freely available image processing software ImageJ. The images were smoothed and converted to an 8-bit binary image format such that the patterned lines were completely black (greyscale value 255), and the background was completely white (greyscale value 0). Line widths and line edge positions for each line were determined using 450 nm long rectangular boxes that completely encompassed each line or line edge. The box provided a column-averaged greyscale profile that was then converted to either a width or edge position profile using the height of the box, from which the average width, width standard deviation, and edge position standard deviation could be extracted.

Monte Carlo simulation The commercial software SRIM (the stopping and range of ions in matter) and CASINO (Monte Carlo simulation of electron trajectory in solids) were used to simulate trajectories of helium ions and electrons respectively. Both simulations were performed based on 1000, 30

keV particles using the same film model derived from RBS and AFM data. In CASINO (electrons), a 0.1 nm beam size was set to have a comparable beam size with helium ions (atom size beam as default) simulated in SRIM.

6.3 Results and Discussion

6.3.1 HafSOx resist sensitivity test with HIBL and EBL

Resist sensitivity was explored with 30 keV helium ions and compared to electronics at the same energy; their contrast curves are shown in Figure 6.1(a). In the case of 30 keV heliumions, D_{100} (the dose at which the developed features start to have 100% of as-deposit resist thickness) occurred at approximately 4 $\mu C/cm^2$. In comparison with 30 keV electrons (D_{100} = 420 $\mu C/cm^2$), the helium ions exhibited ~100 times higher sensitivity. This has been reported in other resist systems as well.[5, 8] Considering the drastic difference in stopping power between helium ions and electrons, we think the stopping power, most of which occurred from secondary electron generation to activate the resist films, was the main contributor to the significant sensitivity improvement. Though the specific stopping power data of 30 keV He^+ ions interacting with HafSOx has not been reported, we summarized of stopping power ratios of He^{2+} ions to e^- in various organic and inorganic materials [4]. As shown in **Figure 6.1(b)** for a list

of common material, the helium ion to electron stopping power ratio are in the 50-100 range among tested resists [5] are in agreement with our results of 50-100 times sensitivity improvement.

Due to the limited availability of helium ion patterning, only a few resists has been tested with HIBL and we summarized their reported sensitivity data, in terms of D_{50}, in the **Table 1** and compared their results with the best sensitivity we have achieved on HafSOx resists. Surprisingly, we found the HafSOx outperformed most common resists with regard to sensitivity and almost shares the best sensitivity with CAR, though, in the EBL case, HafSOx is not quite as good as CAR.

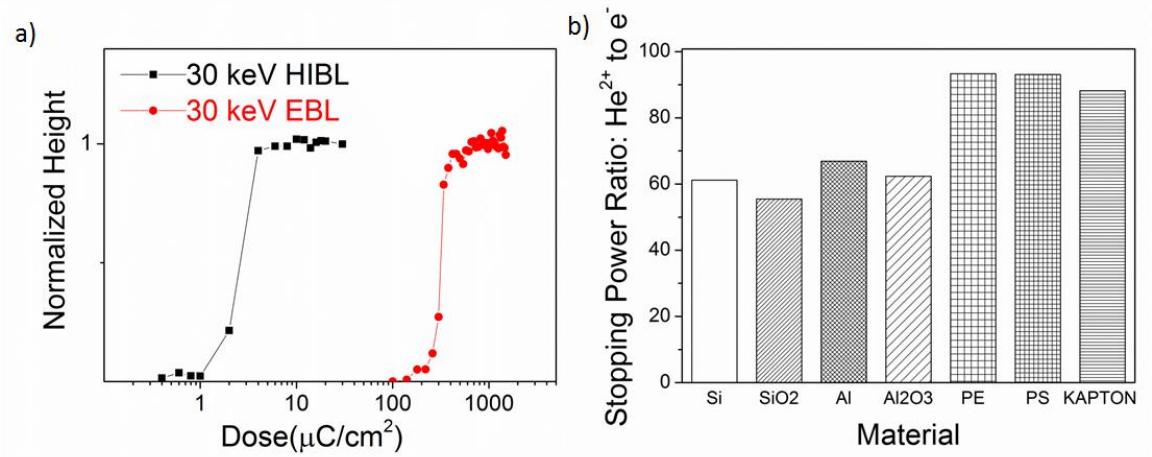

Figure 6.1(a) The contrast curve comparison between HIBL and EBL with a 30 kV acceleration voltage, and (b) the stopping power ratio between He^{2+} and e^- in a few common materials.

Resist	Tone	Sensitivity ($^{*}D_{50}$, μC/cm^2)
PMMA	Negative	68[5]
PMMA	Positive	2[5]
HSQ	Negative	1.7[5], 31[8]
CAR	Positive	0.93[9]
HafSOx	Negative	**1.0

Table 6.1 Resists sensitivity comparison using helium ion beam as incident particles. Acronyms: poly (methyl methacrylate) = PMMA; hydrogen silsesquioxane = HSQ; chemically amplified resist = CAR

*D50 is defined as the dose at which the developed features have half of the thickness of the original resist (positive tone) or of a fully-exposed and developed resist (negative tone).

** The best sensitivity we have achieved.

6.3.2 Study of CD and LER on HafSOx resist

Following the sensitivity investigation, resolution tests of HafSOx with HIBL were conducted by making line patterns with various input line widths at various doses. In particular, the effective line width value we

input into the patterning software was controlled in part by changing the value of pixel spacing and the number of single-pixel-wide lines. **Figure 6.2(a)** is a SHIM image of a line-pattern example exhibiting one of the smallest average line width (9.3 nm) and LER (2.9 nm, 3σ) values we achieved at the dose of 40 μC/cm^2 with 2 nm as the nominal input line width.

We present data in **Figures 6.2(b) and 6.2(c)** that explore the dependence of average line width and LER on doses and input line width. As shown in **Figure 6.2(b)**, for all cases, the measured line widths were always larger than its original input value at high doses and tended to reduce when doses were lowered. For some cases (e.g. 20 nm input width), the measured line width does reach the initial input value. However, for smaller desired features (e.g. 2 nm and 5 nm input widths), the measured line width can only be lowered to ~9-10 nm (under our currently explored system and conditions) by lowering the dose. Further dose reduction led to intermittent "dot" features. To achieve patterns with line width less than 9 nm, we plan to focus on the optimization of resist properties (such as film thickness and composition) and development chemistries, instead of merely changing exposure parameters.

As shown in **Figure 6.2(c)**, we found a larger LER was observed at a larger dose in the tested dose region, which was different from some reported simulations and experimental results[10, 11] (using EBL and EUVL). However, considering the very low turn-on dose (D_{100}, ~ 4μC/cm^2), the doses in the tested region all had more than sufficient ion flux. As indicated by the helium ion expansion issues discussed below (and shown in **Figure 6.3**), we think the excess helium ions may form helium bubbles near the surface, leading to a higher LER at high ion dose. Doses below 10 μC/cm^2 is not meaningful as it is beyond the capability of the current patterning software.

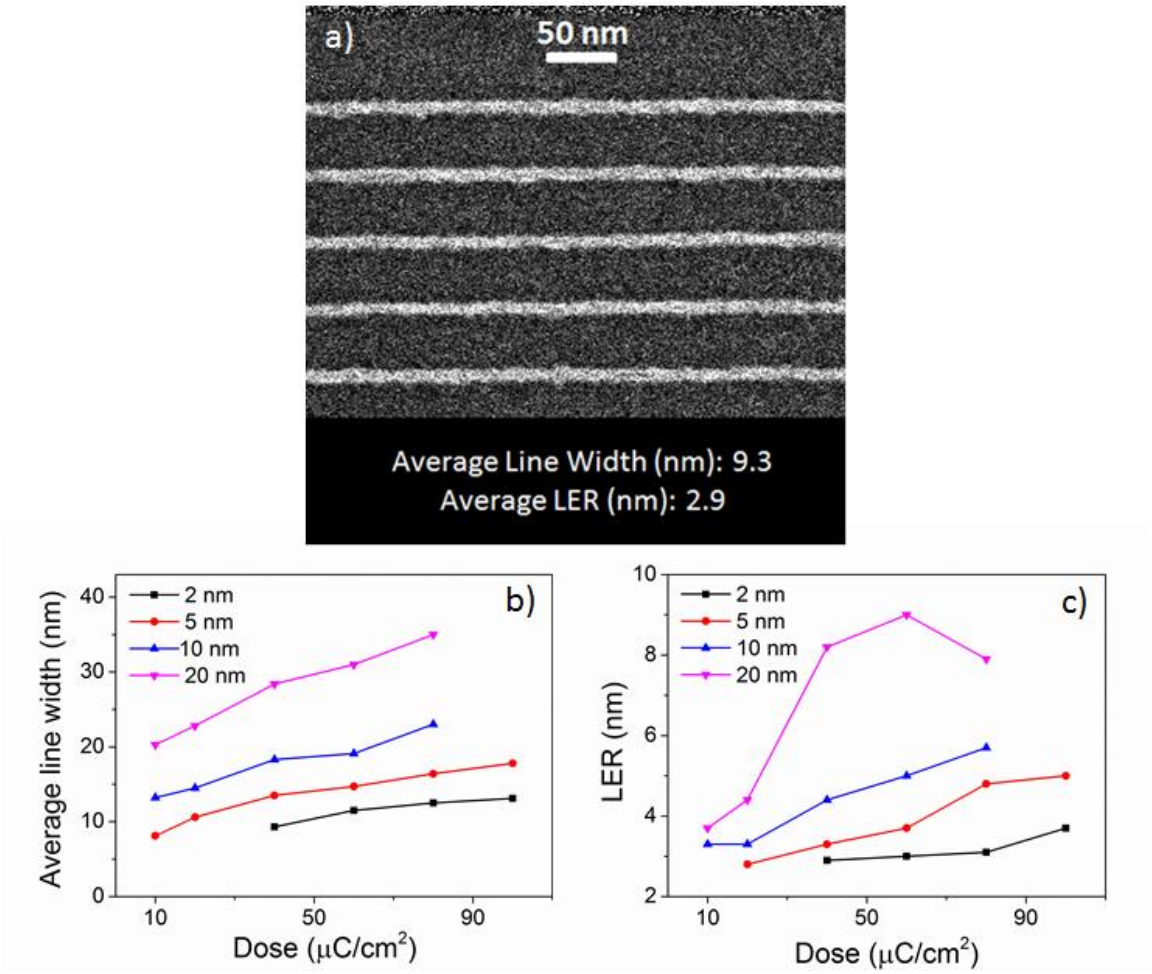

Figure 6.2 (a) A line pattern showing below-10 nm average line width and LER (3σ) 2.9 nm and the dependence of (b) average line width and (c) LER on doses. 2, 5, 10, 20 nm are the input line width values we set in the software during exposure, not the measured real line widths.

6.3.3 High dose feature inflation issues

When we attempted to expose the HafSOx resist with much higher He^+ ion doses, as indicated in **Figure 6.3 (a)**, we find a significant expansion of the resist after development and post-development hard bake. **Figure**

6.3(b) is a 3D AFM image of the developed and hard-baked features of a HafSOx film exposed as in **Figure 6.3(a)**. We found, at a relatively low dose of 0.2 mC/cm^2, that a complete and clear "square" feature was observed. When the dose was increased to 1.6 mC/cm^2, the "square" features became difficult to distinguish due to the growth of the surrounding film in effect forming a large "pad". The pad might result from excess helium ion diffusion or scattering. However, given even higher helium ion dose (>1.8 mC/cm^2), the film started to further build up based on the "pad" feature but only at the exposed area. High dose helium ion implantation (10^{16}-10^{18} ions/cm^2) has been reported[12] to result in the substantial film damage in the form of helium balloons (bulbs). Under our conditions, the most significant inflation happened at doses larger than 10 mC/cm^2, equivalent to 10^{16}-10^{17} ions/cm^2. **Figure 6.3(c)** more clearly compares the height of exposed area features with the "pad" thickness (~10.3 nm) and the as-deposit film thickness (~10.2 nm) after hard-bake.

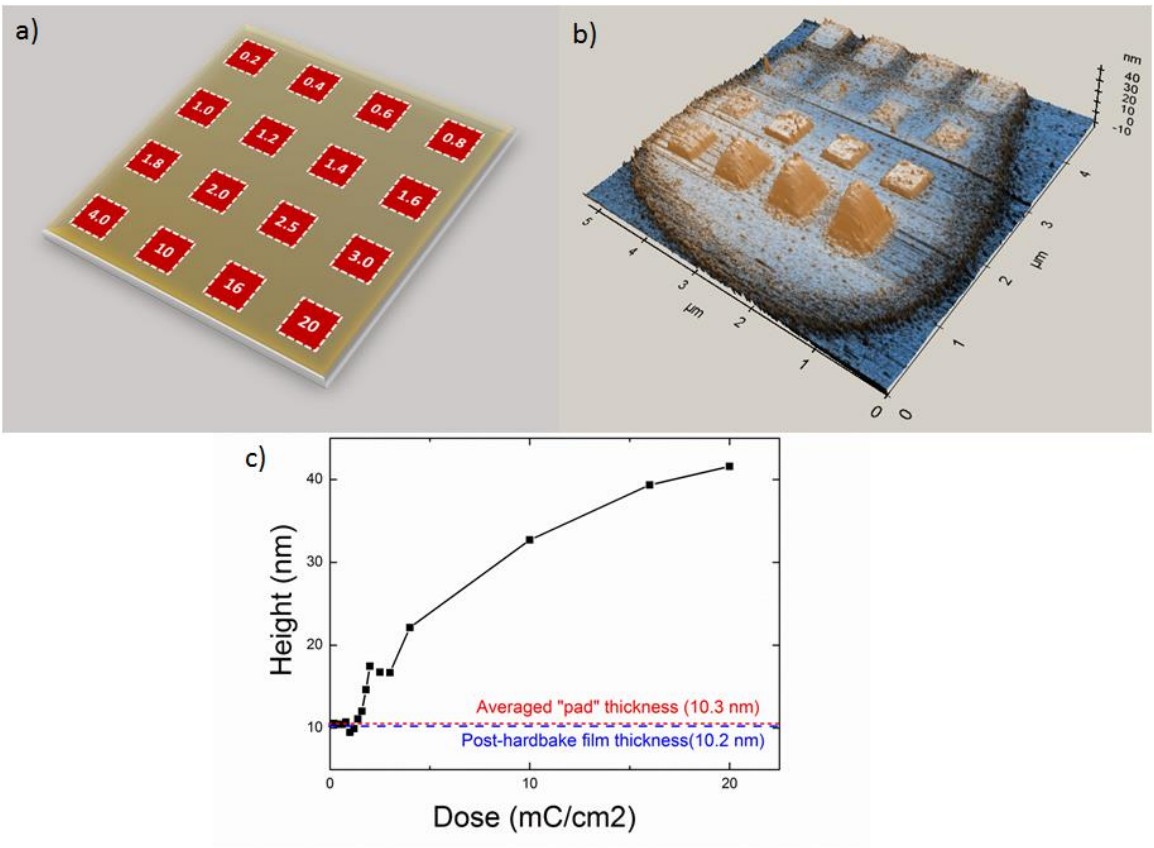

Figure 6.3(a) A scheme showing the exposed square areas at various doses in units of mC/cm^2, and (b) an AFM 3D image of the film after exposure, development (25 wt.% TMAH, 1 min) and post-development hard-bake (300 °C, 5 mins). Reorganization of data in (b) into panel (c) exhibiting the change in the height of the square features as a function of dose**.**

6.3.4 Simulation model construction with Rutherford backscattering spectrometry (RBS)

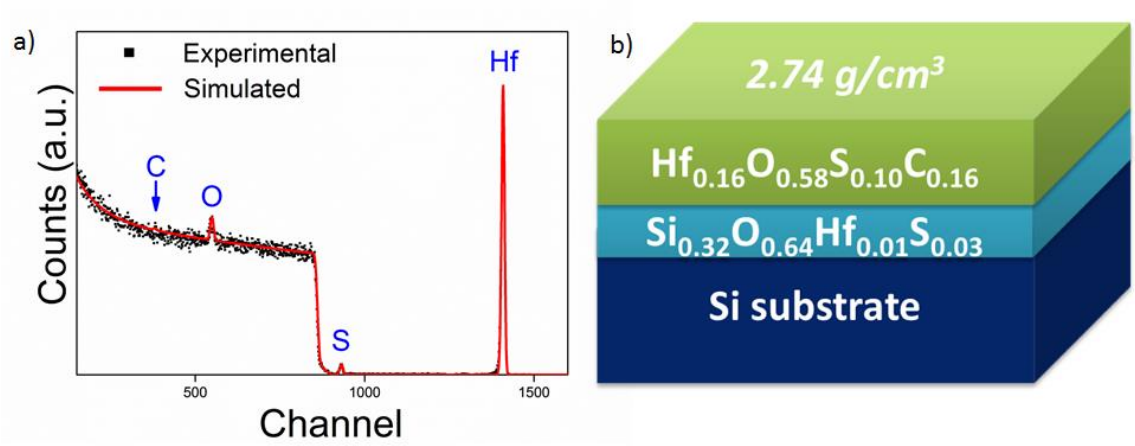

Figure 6.4(a) a RBS spectrum of as-deposited HafSOx films including both experimental data and the simulated curve, and (b) a 3-layer film model derived from it. The top layer density was calculated based on areal density data (RBS) and thickness data (AFM).

An accurate model of film composition and thickness is central to understanding the system. In order to figure out the film composition and structure, RBS was employed. **Figure 6.4 (a)** presents the RBS spectrum of an as-deposited HafSOx film, from which Hf, S, O and C can be distinguished in the form of sharp peaks, while the plateau stands for Si. Considering the low sensitivity of RBS for low Z elements (e.g. O and C), we also conducted x-ray photoelectron spectroscopy (XPS) to better estimate the composition in the surface region. Based on the areal density results

obtained by fitting the RBS spectrum, and the thickness of the top HafSOx (21.1 nm) layer from an AFM measurement, a 3-layer film structure was generated, as shown in **Figure 6.4(b).** On top of the Si substrate is a silicon oxide layer (~ 13.8 nm, calculated based on the known density of 2.196 g/cm^3 for amorphous silicon dioxide) with a trace amount of inter-diffused Hf and S. The HafSOx film had an approximate composition of $Hf_{0.16}O_{0.58}S_{0.10}C_{0.16}$, situated on the surface of silicon oxide layer with a calculated HafSOx film density of 2.74 g/cm^3.

6.3.5 Monte Carlo simulation of helium ions and electrons in HafSOx films

Secondary electron activation has been widely reported[9, 13, 14] to be responsible for the radiation-induced transformation of resists. Helium ions at 30 keV have also been observed [15] to produce secondary electrons with maximum intensity (based on electron emission data) of between 1-5 eV, with an exponential decay in intensity at higher energies. In this study, we first ran SRIM simulation, based on the film model setup in RBS, to study the energy loss of helium ions in HafSOx. We found ionization, which would further initiate the production of electrons, accounted for more than 93% of the total energy loss. **Figure 6.5(a)** shows the energy loss, attributed to

ionization, through the three-layer structure of a HafSOx sample for one 30 keV helium ion. In the top HafSOx layer, the average energy loss was around 6 eV/angstrom spotted from the figure. Therefore, the total energy loss that happened in the 211 angstrom HafSOx equals 1.27 keV. Based on the above discussion, assuming 5 eV as the average energy of the secondary electrons activating the resist film, we would get a number of 253 secondary electrons produced by one 30 keV helium ion in HafSOx layer. Moreover, considering the average fully activation dose D_{100} = 4 $\mu C/cm^2$, which was 0.26 ions/nm^2, it led to a number of 66 secondary electrons/nm^2 to fully activate the HafSOx resist.

On the other hand, comparing the trajectories of helium ions and electrons, as shown in **Figure 6.5(b),** helped us understand the experimental limits and potentials during the exposure process. With the similar starting beam diameter without considering the possible instrumental constraints, we found in the thin (~ 20 nm) HafSOx layer, the electron and helium ion exhibited similar well-confined trajectories Although helium ions have been observed and reported [16] to have much less lateral scattering than the electrons on a much larger scale (e.g. hundreds of nanometers or μm).

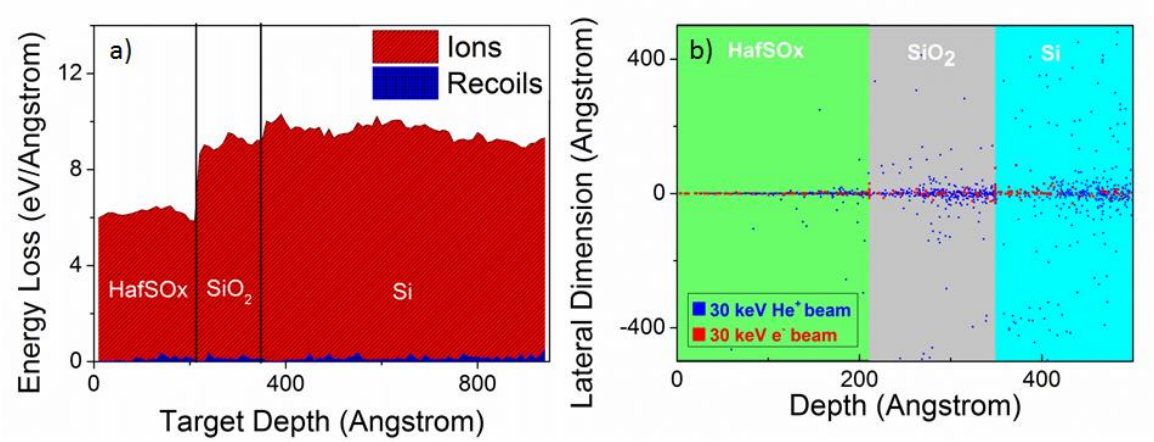

Figure 6.5(a) The simulation result of energy loss, due to ionization, inside the HafSOx film and its substrate; (b) The trajectory comparison between He ion and electron at 30 keV.

6.4 Summary

In this study, we investigated the lithographic performance of the novel inorganic HafSOx resist with HIBL and demonstrated its ultra-high sensitivity (D_{100}< 4 μC/cm^2) and a nearly 100 fold increase in sensitivity compared with EBL under the same conditions. Among tested materials, HafSOx, in the best case, exhibited a sensitivity as good as CAR with HIBL. Sub-10 nm line patterns were achieved with low LER in these initial studies. Interestingly, we found overdosed films, instead of being etched, appeared

inflated, which may be due to helium bubble creation and mechanical deformation during HIBL. A Monte Carlo simulation of helium ions has been conducted to investigate the energy loss and secondary electron production in HafSOx films; a comparison of HIBL with electrons showed similarities in trajectories in the top thin HafSOx region.

References

1. Luo, F.; Manichev, V.; Li, M.; Mitchson, G.; Yakshinskiy, B.; Gustafsson, T.; Johnson, D.; Garfunkel, E. In *Helium ion beam lithography (HIBL) using HafSOx as the resist*, 2016; 2016; pp 977928-977928-9.
2. Blumenstock, G. M.; Meinert, C.; Farrar, N. R.; Yen, A., Evolution of light source technology to support immersion and EUV lithography. *Advanced Microlithography Technologies* **2005,** 5645, 188-195.
3. Watt, F.; Bettiol, A.; Van Kan, J.; Teo, E.; Breese, M., Ion beam lithography and nanofabrication: a review. *International Journal of Nanoscience* **2005,** 4, (03), 269-286.
4. Berger, M. J.; Coursey, J.; Zucker, M.; Chang, J., *Stopping-power and range tables for electrons, protons, and helium ions*.
5. van der Drift, E.; Maas, D. J., *Helium ion lithography*. Springer: 2012.
6. Release, C. Z. S. P. Carl Zeiss SMT Ships World's First ORION Helium Ion Microscope to U.S. National Institute of Standards and Technology. http://www.smt.zeiss.com/C1256A770030BCE0/WebViewTopNewsAllE/573B9EA1B720BBBEC12573080048AF79
7. ITRS, Metrology. **2009**.
8. Sidorkin, V.; van Veldhoven, E.; van der Drift, E.; Alkemade, P.; Salemink, H.; Maas, D., Sub-10-nm nanolithography with a scanning helium beam. *Journal of Vacuum Science & Technology B* **2009,** 27, (4), L18-L20.
9. Maas, D.; van Veldhoven, E.; van Langen-Suurling, A.; Alkemade, P. F. A.; Wuister, S.; Hoefnagels, R.; Verspaget, C.; Meessen, J.; Fliervoet, T., Evaluation of EUV resist performance below 20-nm CD using helium ion lithography. *Extreme Ultraviolet (Euv) Lithography V* **2014,** 9048.
10. Mojarad, N.; Gobrecht, J.; Ekinci, Y., Beyond EUV lithography: a comparative study of efficient photoresists' performance. *Scientific Reports* **2015,** 5.
11. Saeki, A.; Kozawa, T.; Tagawa, S.; Cao, H. B.; Deng, H.; Leeson, M. J., Exposure dose dependence on line edge roughness of a latent image in electron beam/extreme ultraviolet lithographies studied by Monte Carlo technique. *Journal of Micro-Nanolithography Mems and Moems* **2007,** 6, (4).
12. Livengood, R.; Tan, S.; Greenzweig, Y.; Notte, J.; McVey, S., Subsurface damage from helium ions as a function of dose, beam energy, and dose rate. *Journal of Vacuum Science & Technology B* **2009,** 27, (6), 3244-3249.
13. Jeyakumar, A. Development of Inorganic Resists for Electron Beam Lithography: Novel Materials and Simulations. Georgia Institute of Technology, 2004.
14. Kozawa, T.; Tagawa, S., Radiation Chemistry in Chemically Amplified Resists. *Japanese Journal of Applied Physics* **2010,** 49, (3).
15. Petrov, Y.; Vyvenko, O., Secondary electron emission spectra and energy selective imaging in helium ion microscope. *Scanning Microscopies 2011: Advanced Microscopy Technologies for Defense, Homeland Security, Forensic, Life, Environmental, and Industrial Sciences* **2011,** 8036.
16. Cohen-Tanugi, D.; Yao, N., Superior imaging resolution in scanning helium-ion microscopy: A look at beam-sample interactions. *Journal of Applied Physics* **2008,** 104, (6).

Chapter 7 : Conclusions

Metal oxide nanoparticles have become a mainstream photoresist candidate for extreme ultraviolet lithography (EUVL). HafSOx systems, as one of the first generation resists in this category, has attracted our attention due to its systematic simplicity and great versatility.

In this thesis, we develop a mechanistic investigation of inorganic resists first by adopting various material characterization methods, such as x-ray photoelectron spectroscopy (XPS), Rutherford backscattering spectroscopy (RBS), and others, to comprehensively understand film composition and chemistry, from which we then study the underlying photochemistry during ion, electron or photons exposure, respectively. With better mechanistic information in mind, we optimized the HafSOx system, by varying the precursor partition ratio to achieve better patterning performance. The well-known low energy electron activation mechanism in EUVL has also been experimentally investigated and we found clear evidence to support this hypothesis. Besides the mechanistic study, emerging lithography techniques, such as helium ion beam lithography were conducted with HafSOx resists and systematically characterized.

Bibliography

1. Moore, G. E., Cramming more components onto integrated circuits (Reprinted from Electronics, pg 114-117, April 19, 1965). *Proceedings of the Ieee* **1998,** 86, (1), 82-85.
2. Shuler, K. Moore's Law is Dead: Long Live SoC Designers. http://info.arteris.com/blog/moores-law-is-dead-long-live-soc-designers
3. Jaeger, R. C., *Introduction to microelectronic fabrication*. 2nd ed.; Prentice Hall: Upper Saddle River, N.J., 2002; p xiv, 316 p.
4. May, G. S.; Spanos, C. J., *Fundamentals of semiconductor manufacturing and process control*. IEEE ; Wiley-Interscience: Piscataway
Hoboken, N.J., 2006; p xix, 463 p.
5. Levinson, H. J., Principles of lithography. In *Press monograph 198*, 3rd ed.; SPIE Press,: Bellingham, Wash., 2010; pp 1 online resource (xiv, 503 pages).
6. Bucknall, D. G., Nanolithography and patterning techniques in microelectronics. In *Woodhead Publishing in materials*, Woodhead Pub. ;
CRC Press,: Cambridge
Boca Raton, FL, 2005; pp 1 online resource (xiv, 409 p.).
7. Chou, S. Y.; Krauss, P. R.; Renstrom, P. J., Nanoimprint lithography. *Journal of Vacuum Science & Technology B* **1996,** 14, (6), 4129-4133.
8. Srituravanich, W.; Fang, N.; Sun, C.; Luo, Q.; Zhang, X., Plasmonic nanolithography. *Nano Letters* **2004,** 4, (6), 1085-1088.
9. Kim, S. O.; Solak, H. H.; Stoykovich, M. P.; Ferrier, N. J.; de Pablo, J. J.; Nealey, P. F., Epitaxial self-assembly of block copolymers on lithographically defined nanopatterned substrates. *Nature* **2003,** 424, (6947), 411-414.
10. Kim, B. H.; Shin, D. O.; Jeong, S. J.; Koo, C. M.; Jeon, S. C.; Hwang, W. J.; Lee, S.; Lee, M. G.; Kim, S. O., Hierarchical self-assembly of block copolymers for lithography-free nanopatterning. *Advanced Materials* **2008,** 20, (12), 2303-+.
11. Jeong, S. J.; Kim, J. Y.; Kim, B. H.; Moon, H. S.; Kim, S. O., Directed self-assembly of block copolymers for next generation nanolithography. *Materials Today* **2013,** 16, (12), 468-476.
12. Pan, L.; Park, Y.; Xiong, Y.; Ulin-Avila, E.; Wang, Y.; Zeng, L.; Xiong, S. M.; Rho, J.; Sun, C.; Bogy, D. B.; Zhang, X., Maskless Plasmonic Lithography at 22 nm Resolution. *Scientific Reports* **2011,** 1.
13. Kim, Y.; Kim, S.; Jung, H.; Lee, E.; Hahn, J. W., Plasmonic nano lithography with a high scan speed contact probe. *Optics Express* **2009,** 17, (22), 19476-19485.
14. Xia, Q. F.; Pease, R. F., Nanoimprint lithography 20 years on. *Nanotechnology* **2015,** 26, (18).
15. Alphonse-Louis Poitevin. http://www.getty.edu/art/collection/artists/1913/alphonse-louis-poitevin-french-1819-1882/
16. Levenson, M. D., Wave-Front Engineering for Photolithography. *Physics Today* **1993,** 46, (7), 28-36.
17. Borkar, S., Microarchitecture and Design Challenges for Gigascale Integration. In *Proceedings of the 37th annual IEEE/ACM International Symposium on Microarchitecture*, IEEE Computer Society: Portland, Oregon, 2004; pp 3-3.
18. Sansonetti, C. J.; Salit, M. L.; Reader, J., Wavelengths of spectral lines in mercury pencil lamps. *Applied Optics* **1996,** 35, (1), 74-77.
19. Sandstrom, R., Argon Fluoride Excimer Laser Source for Sub-0.25 Mm Optical Lithography. *Optical/Laser Microlithography Iv* **1991,** 1463, 610-616.
20. Besaucele, H.; Das, P.; Duffey, T.; Embree, T.; Ershov, A.; Fleurov, V.; Grove, S.; Melcher, P.; Ness, R.; Padmadandu, G. G., A comparison of ArF and KrF laser performance at 2kHz for microlithography. *Optical Microlithography Xiii, Pts 1 and 2* **2000,** 4000, 1476-1480.
21. Rothschild, M.; Goodman, R. B.; Hartney, M. A.; Horn, M. W.; Kunz, R. R.; Sedlacek, J. H. C.; Shaver, D. C., Photolithography at 193 Nm. *Journal of Vacuum Science & Technology B* **1992,** 10, (6), 2989-2996.
22. Tallents, G.; Wagenaars, E.; Pert, G., OPTICAL LITHOGRAPHY Lithography at EUV wavelengths. *Nature Photonics* **2010,** 4, (12), 809-811.

23. Flagello, D. G.; Renwick, S. P., Evolving Optical Lithography without EUV. *Optical Microlithography Xxviii* **2015,** 9426.
24. Singer, P., Lithography: What are the alternatives to EUV? Hopes remain high for EUV, but long delays has caused attention to shift to various alternatives. *Solid State Technology* **2014,** 57, (6), 14-17.
25. Hruska, J. TSMC announces lithography milestone as EUV moves closer to production. http://www.extremetech.com/computing/199782-tmsc-announces-lithography-milestone-as-euv-moves-closer-to-production
26. Wu, C. S.; Makiuchi, Y.; Chen, C., *High-energy Electron Beam Lithography for Nanoscale Fabrication*. 2010.
27. Chen, Y. F., Nanofabrication by electron beam lithography and its applications: A review. *Microelectronic Engineering* **2015,** 135, 57-72.
28. Hohn, F. J., Electron-Beam Lithography - Its Applications. *Journal of Vacuum Science & Technology B* **1989,** 7, (6), 1405-1411.
29. Vieu, C.; Carcenac, F.; Pepin, A.; Chen, Y.; Mejias, M.; Lebib, A.; Manin-Ferlazzo, L.; Couraud, L.; Launois, H., Electron beam lithography: resolution limits and applications. *Applied Surface Science* **2000,** 164, 111-117.
30. Manfrinato, V. R.; Zhang, L. H.; Su, D.; Duan, H. G.; Hobbs, R. G.; Stach, E. A.; Berggren, K. K., Resolution Limits of Electron-Beam Lithography toward the Atomic Scale. *Nano Letters* **2013,** 13, (4), 1555-1558.
31. Ahmed, H.; Broers, A., Lanthanum hexaboride electron emitter. *Journal of Applied Physics* **1972,** 43, (5), 2185-2192.
32. Broers, A., Some experimental and estimated characteristics of the lanthanum hexaboride rod cathode electron gun. *Journal of Physics E: Scientific Instruments* **1969,** 2, (3), 273.
33. Fukuhara, S.; Todokoro, H.; Sakitani, Y., Field emission electron gun. In Google Patents: 1981.
34. Parker, N. W.; Brodie, A. D.; McCoy, J. H., A high throughput NGL electron beam direct-write lithography system. *Emerging Lithographic Technologies Iv* **2000,** 3997, 713-720.
35. Barron, A. R. Composition and Photochemical Mechanisms of Photoresists. http://cnx.org/contents/2997481b-ecd7-4e38-9465-677d8adbe0ad@2/Composition-and-Photochemical-#id2321669
36. Dammel, R., *Diazonaphthoquinone-based resists*. SPIE Optical Engineering Press: Bellingham, Wash., USA, 1993; p 203 p.
37. Frasch, P.; Saremski, K. H., Feature Size Control in Ic Manufacturing. *Ibm Journal of Research and Development* **1982,** 26, (5), 561-567.
38. Henderson, C. L., Introduction to DNQ-Novolac Resists.
39. Ito, H., Chemical amplification resists: History and development within IBM. *IBM Journal of Research & Development* **2000,** 44, (1/2), 12p.
40. Ito, H.; Willson, C. G.; Frechet, J. H. In *New UV resists with negative or positive tone*, 1982 Symposium on VLSI Technology. Digest of Technical Papers, 1982; 1982; pp 86-87.
41. Yang, C. C.; Chen, W. C., The structures and properties of hydrogen silsesquioxane (HSQ) films produced by thermal curing. *Journal of Materials Chemistry* **2002,** 12, (4), 1138-1141.
42. Yang, J. K. W.; Cord, B.; Duan, H. G.; Berggren, K. K.; Klingfus, J.; Nam, S. W.; Kim, K. B.; Rooks, M. J., Understanding of hydrogen silsesquioxane electron resist for sub-5-nm-half-pitch lithography. *Journal of Vacuum Science & Technology B* **2009,** 27, (6), 2622-2627.
43. Namatsu, H.; Takahashi, Y.; Yamazaki, K.; Yamaguchi, T.; Nagase, M.; Kurihara, K., Three-dimensional siloxane resist for the formation of nanopatterns with minimum linewidth fluctuations. *Journal of Vacuum Science & Technology B* **1998,** 16, (1), 69-76.
44. Zanchetta, E.; Della Giustina, G.; Grenci, G.; Pozzato, A.; Tormen, M.; Brusatin, G., Novel Hybrid Organic-Inorganic Spin-on Resist for Electron- or Photon-Based Nanolithography with Outstanding Resistance to Dry Etching (vol 25, pg 6261, 2013). *Advanced Materials* **2014,** 26, (5), 674-674.
45. Hawryluk, A. M.; Seppala, L. G., Soft x-ray projection lithography using an x-ray reduction camera. *Journal of Vacuum Science & Technology B* **1988,** 6, (6), 2162-2166.
46. Kinoshita, H.; Kurihara, K.; Ishii, Y.; Torii, Y., Soft x-ray reduction lithography using multilayer mirrors. *Journal of Vacuum Science & Technology B* **1989,** 7, (6), 1648-1651.

47. Bjorkholm, J. E.; Bokor, J.; Eichner, L.; Freeman, R. R.; Gregus, J.; Jewell, T. E.; Mansfield, W. M.; Mac Dowell, A. A.; Raab, E. L.; Silfvast, W. T.; Szeto, L. H.; Tennant, D. M.; Waskiewicz, W. K.; White, D. L.; Windt, D. L.; Wood, O. R.; Bruning, J. H., Reduction imaging at 14 nm using multilayer-coated optics: Printing of features smaller than 0.1 μm. *Journal of Vacuum Science & Technology B* **1990,** 8, (6), 1509-1513.
48. Wu, B. Q.; Kumar, A., Extreme ultraviolet lithography and three dimensional integrated circuit-A review. *Applied Physics Reviews* **2014,** 1, (1).
49. Moore, G. E., Cramming more components onto integrated circuits (Reprinted from Electronics, pg 114-117, April 19, 1965). *Proceedings of the Ieee* **1998,** 86, (1), 82-85.
50. Wua, B. Q.; Kumar, A., Extreme ultraviolet lithography: A review. *Journal of Vacuum Science & Technology B* **2007,** 25, (6), 1743-1761.
51. Bakshi, V. 2015 SPIE Advanced Lithography EUVL Conference – Summary and Analysis. http://electroiq.com/euvl-focus/2015/03/10/2015-spie-advanced-lithography-euvl-conference-summary-and-analysis/
52. Wang, F. L.; Liu, L.; Li, W. B.; Zhu, J. T.; Zhang, Z.; Wang, Z. S.; Chen, L. Y., Design of the chirped Mo/Si multilayer mirror with SiC capping layer in extreme ultraviolet region. *Optik* **2012,** 123, (24), 2222-2225.
53. Yulin, S.; Benoit, N.; Feigl, T.; Kaiser, N.; Fang, M.; Chandhok, M., Mo/Si multilayers with enhanced TiO(2)- and RuO(2)-capping layers. *Emerging Lithographic Technologies Xii, Pts 1 and 2* **2008,** 6921.
54. Bajt, S.; Alameda, J. B.; Barbee, T. W.; Clift, W. M.; Folta, J. A.; Kaufmann, B.; Spiller, E. A., Improved reflectance and stability of Mo-Si multilayers. *Optical Engineering* **2002,** 41, (8), 1797-1804.
55. JohnKadaksham, A.; Teki, R.; Godwin, M.; House, M.; Goodwin, F., Low Thermal Expansion Material (LTEM) Cleaning and Optimization for Extreme Ultraviolet (EUV) Blank Deposition. *Extreme Ultraviolet (Euv) Lithography Iv* **2013,** 8679.
56. Stowers, J.; Keszler, D. A., High resolution, high sensitivity inorganic resists. *Microelectronic Engineering* **2009,** 86, (4-6), 730-733.
57. Cardineau, B.; Del Re, R.; Al-Mashat, H.; Marnell, M.; Vockenhuber, M.; Ekinci, Y.; Sarma, C.; Neisser, M.; Freedman, D. A.; Brainard, R. L., EUV Resists based on Tin-Oxo Clusters. *Advances in Patterning Materials and Processes Xxxi* **2014,** 9051.
58. Del Re, R.; Sortland, M.; Passarelli, J.; Cardineau, B.; Ekinci, Y.; Vockenhuber, M.; Neisser, M.; Freedman, D. A.; Brainard, R. L., Low-LER Tin Carboxylate Photoresists using EUV. *Extreme Ultraviolet (Euv) Lithography Vi* **2015,** 9422.
59. X-ray photoelectron spectroscopy. In Wikipedia.
60. Hollander, A.; Haupt, M.; Oehr, C., On depth profiling of polymers by argon ion sputtering. *Plasma Processes and Polymers* **2007,** 4, (9), 773-776.
61. Gilbert, J. B.; Rubner, M. F.; Cohen, R. E., Depth-profiling X-ray photoelectron spectroscopy (XPS) analysis of interlayer diffusion in polyelectrolyte multilayers. *Proceedings of the National Academy of Sciences of the United States of America* **2013,** 110, (17), 6651-6656.
62. Mayer, M., Rutherford Backscattering Spectrometry (RBS). In Workshop on Nuclear Data for Science and Technology: Materials Analysis, 2003.
63. Atomic force microscopy. https://en.wikipedia.org/wiki/Atomic_force_microscopy
64. Melitz, W.; Shen, J.; Kummel, A. C.; Lee, S., Kelvin probe force microscopy and its application. *Surface Science Reports* **2011,** 66, (1), 1-27.
65. Kneipp, K.; Kneipp, H.; I, I.; Dasari, R. R.; Feld, M. S., Ultrasensitive chemical analysis by Raman spectroscopy. *Chemical Reviews* **1999,** 99, (10), 2957-+.
66. Schrader, B., *Infrared and Raman spectroscopy: methods and applications*. John Wiley & Sons: 2008.
67. O'Donnell, A. G.; Young, I. M.; Rushton, S. P.; Shirley, M. D.; Crawford, J. W., Visualization, modelling and prediction in soil microbiology. *Nature Reviews Microbiology* **2007,** 5, (9), 689-699.
68. Scanning electron microscope. https://en.wikipedia.org/wiki/Scanning_electron_microscope
69. Hlawacek, G.; Veligura, V.; van Gastel, R.; Poelsema, B., Helium ion microscopy. *Journal of Vacuum Science & Technology B* **2014,** 32, (2).
70. Anderson, J. T.; Munsee, C. L.; Hung, C. M.; Phung, T. M.; Herman, G. S.; Johnson, D. C.; Wager, J. F.; Keszler, D. A., Solution-processed HafSOx and ZircSOx inorganic thin-film dielectrics and nanolaminates. *Advanced Functional Materials* **2007,** 17, (13), 2117-2124.
71. Stowers, J.; Keszler, D. A., High resolution, high sensitivity inorganic resists. *Microelectronic Engineering* **2009,** 86, (4-6), 730-733.

72. Muha, G. M.; Vaughan, P. A., Structure of the complex ion in aqueous solutions of zirconyl and hafnyl oxyhalides. *The Journal of Chemical Physics* **1960,** 33, (1), 194-199.
73. Aaberg, M., An X-ray investigation of some aqueous zirconium (IV) halide, a hafnium (IV) chloride, and some zirconium (IV) perchlorate solutions. **1977**.
74. Connick, R. E.; McVey, W. H., The aqueous chemistry of zirconium. *Journal of the American Chemical Society* **1949,** 71, (9), 3182-3191.
75. Flynn, B.; Kim, D.; Clark, B. L.; Telecky, A.; Arnadottir, L.; Szanyi, J.; Keszler, D. A.; Herman, G. S., In-situ characterization of aqueous-based hafnium oxide hydroxide sulfate thin films. *Surface and Interface Analysis* **2014,** 46, (4), 210-215.
76. Kalaji, A.; Soderholm, L., A novel nonanuclear hafnium oxide-hydroxide-sulphate cluster crystallised from aqueous solution. *Chemical Communications* **2014,** 50, (8), 997-999.
77. Yoo, Y. B.; Park, J. H.; Lee, K. H.; Lee, H. W.; Song, K. M.; Lee, S. J.; Baik, H. K., Solution-processed high-k HfO2 gate dielectric processed under softening temperature of polymer substrates. *Journal of Materials Chemistry C* **2013,** 1, (8), 1651-1658.
78. Jiang, K.; Anderson, J. T.; Hoshino, K.; Li, D.; Wager, J. F.; Keszler, D. A., Low-Energy Path to Dense HfO2 Thin Films with Aqueous Precursor. *Chemistry of Materials* **2011,** 23, (4), 945-952.
79. Halle, J. C.; Stern, K. H., Vaporization and Decomposition of Na2so4 - Thermodynamics and Kinetics. *Journal of Physical Chemistry* **1980,** 84, (13), 1699-1704.
80. Meskin, P. E.; Sharikov, F. Y.; Ivanov, V. K.; Churagulov, B. R.; Tretyakov, Y. D., Rapid formation of nanocrystalline HfO2 powders from amorphous hafnium hydroxide under ultrasonically assisted hydrothermal treatment. *Materials Chemistry and Physics* **2007,** 104, (2-3), 439-443.
81. Anthony, M. T.; Seah, M. P., Xps - Energy Calibration of Electron Spectrometers .2. Results of an Interlaboratory Comparison. *Surface and Interface Analysis* **1984,** 6, (3), 107-115.
82. Anthony, M. T.; Seah, M. P., Xps - Energy Calibration of Electron Spectrometers .1. An Absolute, Traceable Energy Calibration and the Provision of Atomic Reference Line Energies. *Surface and Interface Analysis* **1984,** 6, (3), 95-106.
83. Seah, M. P.; Gilmore, I. S.; Spencer, S. J., XPS: Binding energy calibration of electron spectrometers 4 - Assessment of effects for different x-ray sources, analyser resolutions, angles of emission and overall uncertainties. *Surface and Interface Analysis* **1998,** 26, (9), 617-641.
84. Seah, M. P.; Gilmore, L. S.; Beamson, G., XPS: Binding energy calibration of electron spectrometers 5 - Re-evaluation of the reference energies. *Surface and Interface Analysis* **1998,** 26, (9), 642-649.
85. Cao, D.; Cheng, X. H.; Xie, Y. H.; Li, X. L.; Wang, Z. J.; Xia, C.; Zheng, L.; Xu, D. W.; Shen, L. Y.; Yu, Y. H., Properties of HfO2/La2O3 nanolaminate films grown on an AlGaN/GaN heterostructure by plasma enhanced atomic layer deposition. *Rsc Advances* **2014,** 4, (69), 36828-36833.
86. Lee, S.; Kim, W. G.; Rhee, S. W.; Yong, K., Resistance switching behaviors of hafnium oxide films grown by MOCVD for nonvolatile memory applications. *Journal of the Electrochemical Society* **2008,** 155, (2), H92-H96.
87. Xie, H. W.; Liu, Q.; Li, Y. T.; Lv, H. B.; Wang, M.; Liu, X. Y.; Sun, H. T.; Yang, X. Y.; Long, S. B.; Liu, S.; Liu, M., Nitrogen-induced improvement of resistive switching uniformity in a HfO2-based RRAM device. *Semiconductor Science and Technology* **2012,** 27, (12).
88. Scientific, T. XPS Reference. http://xpssimplified.com/elements/hafnium.php
89. Gao, H. Y.; Wang, G.; Luan, Y.; Chaikittikul, K.; Zhang, X. W.; Yang, M.; Dong, W. J.; Shi, Z., A fast synthesis of hierarchical yolk-shell copper hydroxysulfates at room temperature with adjustable sizes. *Crystengcomm* **2014,** 16, (12), 2520-2526.
90. Sumboja, A.; Foo, C. Y.; Yan, J.; Yan, C. Y.; Gupta, R. K.; Lee, P. S., Significant electrochemical stability of manganese dioxide/polyaniline coaxial nanowires by self-terminated double surfactant polymerization for pseudocapacitor electrode. *Journal of Materials Chemistry* **2012,** 22, (45), 23921-23928.
91. Park, J. H.; Yoo, Y. B.; Lee, K. H.; Jang, W. S.; Oh, J. Y.; Chae, S. S.; Baik, H. K., Low-Temperature, High-Performance Solution-Processed Thin-Film Transistors with Peroxo-Zirconium Oxide Dielectric. *Acs Applied Materials & Interfaces* **2013,** 5, (2), 410-417.
92. Venkateswaran, S., Raman Spectrum of Hydrogen Peroxide. *Nature* **1931,** 127, 406.
93. Giguère, P. A.; Chen, H., Hydrogen bonding in hydrogen peroxide and water. A raman study of the liquid state. *Journal of Raman spectroscopy* **1984,** 15, (3), 199-204.

94. Giguere, P.; Srinivasan, T., A Raman study of H2O2 and D2O2 vapor. *Journal of Raman Spectroscopy* **1974,** 2, (2), 125-132.
95. Tarafder, M. T. H.; Miah, M. A. L., Novel Peroxo Complexes of Zirconium Containing Organic-Ligands. *Inorganic Chemistry* **1986,** 25, (13), 2265-2268.
96. Tarafder, M.; Bhattacharjee, P.; Sarkar, A., Peroxo complexes of chromium (VI), molybdenum (VI), tungsten (VI) and zirconium (IV) ions containing tridentate and quadridentate neutral ligands. *Polyhedron* **1992,** 11, (7), 795-798.
97. Malinowski, E. R.; Cox, R. A.; Haldna, U. L., Factor-Analysis for Isolation of the Raman-Spectra of Aqueous Sulfuric-Acid Components. *Analytical Chemistry* **1984,** 56, (4), 778-781.
98. Rudolph, W. W.; Brooker, M. H.; Tremaine, P. R., Raman spectroscopy of aqueous ZnSO4 solutions under hydrothermal conditions: Solubility, hydrolysis, and sulfate ion pairing. *Journal of Solution Chemistry* **1999,** 28, (5), 621-630.
99. Szilagyi, I.; Konigsberger, E.; May, P. M., Characterization of Chemical Speciation of Titanyl Sulfate Solutions for Production of Titanium Dioxide Precipitates. *Inorganic Chemistry* **2009,** 48, (5), 2200-2204.
100. Vasilopoulou, M.; Boyatzis, S.; Raptis, I.; Dimotikalli, D.; Argitis, P., Evaluation of poly(hydroxyethyl methacrylate) imaging chemistries for micropatterning applications. *Journal of Materials Chemistry* **2004,** 14, (22), 3312-3320.
101. Lee, E. H.; Rao, G. R.; Mansur, L. K., LET effect on cross-linking and scission mechanisms of PMMA during irradiation. *Radiation Physics and Chemistry* **1999,** 55, (3), 293-305.
102. Zhao, M., Exploration of non-chemically amplified resists based on chain-scission mechanism for 193 nm lithography. **2010**.
103. Thompson, L.; Ballantyne, J.; Feit, E., Molecular parameters and lithographic performance of poly (glycidyl methacrylate-co-ethyl acrylate): A negative electron resist. *Journal of Vacuum Science & Technology* **1975,** 12, (6), 1280-1283.
104. Caster, A. G.; Kowarik, S.; Schwartzberg, A. M.; Nicolet, O.; Lim, S. H.; Leone, S. R., Observing hydrogen silsesquioxane cross-linking with broadband CARS. *Journal of Raman Spectroscopy* **2009,** 40, (7), 770-774.
105. Barber, R. L.; Ghantasala, M. K.; Divan, R.; Mancini, D. C.; Harvey, E. C., Study of stress and adhesion strength in SU-8 resist layers on silicon substrate with different seed layers. *Journal of Micro-Nanolithography Mems and Moems* **2007,** 6, (3).
106. Warren, B. E., *X-ray Diffraction*. Courier Corporation: 1969.
107. Benninghoven, A., Chemical-Analysis of Inorganic and Organic-Surfaces and Thin-Films by Static Time-of-Flight Secondary-Ion Mass-Spectrometry (Tof-Sims). *Angewandte Chemie-International Edition in English* **1994,** 33, (10), 1023-1043.
108. Oleksak, R. P.; Ruther, R. E.; Luo, F. X.; Fairley, K. C.; Decker, S. R.; Stickle, W. F.; Johnson, D. W.; Garfunkel, E. L.; Herman, G. S.; Keszler, D. A., Chemical and Structural Investigation of High-Resolution Patterning with HafSOx. *Acs Applied Materials & Interfaces* **2014,** 6, (4), 2917-2921.
109. Nam, S. W.; Rooks, M. J.; Yang, J. K. W.; Berggren, K. K.; Kim, H. M.; Lee, M. H.; Kim, K. B.; Sim, J. H.; Yoon, D. Y., Contrast enhancement behavior of hydrogen silsesquioxane in a salty developer. *Journal of Vacuum Science & Technology B* **2009,** 27, (6), 2635-2639.
110. Kim, J.; Chao, W. L.; Griedel, B.; Liang, X. G.; Lewis, M.; Hilken, D.; Olynick, D., Understanding the base development mechanism of hydrogen silsesquioxane. *Journal of Vacuum Science & Technology B* **2009,** 27, (6), 2628-2634.
111. Vu, M. Allred-Rochow Electronegativity. http://chemwiki.ucdavis.edu/Physical_Chemistry/Physical_Properties_of_Matter/Atomic_and_Molecular_Properties/Electronegativity/Allred-Rochow_Electronegativity
112. Arumainayagam, C. R.; Lee, H. L.; Nelson, R. B.; Haines, D. R.; Gunawardane, R. P., Low-energy electron-induced reactions in condensed matter. *Surface Science Reports* **2010,** 65, (1), 1-44.
113. Duke, C. B., The birth and evolution of surface science: Child of the union of science and technology. *Proceedings of the National Academy of Sciences of the United States of America* **2003,** 100, (7), 3858-3864.
114. Stowers, J., Imageable Oxides: New Solutions for Resist. In rev3.pptx, S.-I. E. S., Ed. 2010 International Symposium on Extreme Ultraviolet Lithography, 2010.
115. Seah, M.; Dench, W., Quantitative electron spectroscopy of surfaces. *Surface and interface analysis* **1979,** 1, (1), 2-11.

116. Bayard-Alpert Gauge Filaments: Tungsten or Thoria? . http://www.thinksrs.com/downloads/PDFs/ApplicationNotes/IG1filamentsapp.pdf
117. Jenkins, R., A review of thermionic cathodes. *Vacuum* **1969,** 19, (8), 353-359.
118. Gear, P., The choice of cathode material in a hot cathode ionization gauge. *Vacuum* **1976,** 26, (1), 3-10.
119. Samsonov, G., Handbook of thermionic properties. In Plenum Data Division, New York: 1966.
120. Casino: monte carlo simulation of electron trajectory in solids. http://www.gel.usherbrooke.ca/casino/index.html
121. Demers, H.; Poirier-Demers, N.; Couture, A. R.; Joly, D.; Guilmain, M.; de Jonge, N.; Drouin, D., Three-Dimensional Electron Microscopy Simulation with the CASINO Monte Carlo Software. *Scanning* **2011,** 33, (3), 135-146.
122. Drouin, D.; Couture, A. R.; Joly, D.; Tastet, X.; Aimez, V.; Gauvin, R., CASINO V2. 42-A fast and easy-to-use modeling tool for scanning electron microscopy and microanalysis users. *Scanning* **2007,** 29, (3), 92-101.
123. Mott, N. F., The exclusion principle and aperiodic systems. *Proceedings of the Royal Society of London. Series A, Containing Papers of a Mathematical and Physical Character* **1929**, 222-230.
124. Browning, R.; Eimori, T.; Traut, E. P.; Chui, B.; Pease, R. F. W., An Elastic Cross-Section Model for Use with Monte-Carlo Simulations of Low-Energy Electron-Scattering from High Atomic-Number Targets. *Journal of Vacuum Science & Technology B* **1991,** 9, (6), 3578-3581.
125. Browning, R.; Eimori, T.; Traut, E. P.; Chui, B.; Pease, R. F. W., An Elastic Cross-Section Model for Use with Monte-Carlo Simulations of Low-Energy Electron-Scattering from High Atomic-Number Targets. *Journal of Vacuum Science & Technology B* **1991,** 9, (6), 3578-3581.
126. Browning, R.; Li, T. Z.; Chui, B.; Ye, J.; Pease, R. F. W.; Czyzewski, Z.; Joy, D. C., Empirical Forms for the Electron-Atom Elastic-Scattering Cross-Sections from 0.1 to 30 Kev. *Journal of Applied Physics* **1994,** 76, (4), 2016-2022.
127. Browning, R.; Li, T. Z.; Chui, B.; Ye, J.; Pease, R. F. W.; Czyzewski, Z.; Joy, D. C., Low-Energy-Electron Atom Elastic-Scattering Cross-Sections from 0.1-30 Kev. *Scanning* **1995,** 17, (4), 250-253.
128. Drouin, Computation of Polar Angle of Collisions from Partial Elastic Mott Cross-Sections (Vol 16, Pg 67, 1994). *Scanning* **1995,** 17, (3), U8-U8.
129. Drouin, D.; Gauvin, R.; Joy, D. C., Computation of Polar Angle of Collisions from Partial Elastic Mott Cross-Sections. *Scanning* **1994,** 16, (2), 67-77.
130. Casnati, E.; Tartari, A.; Baraldi, C., An Empirical-Approach to K-Shell Ionization Cross-Section by Electrons. *Journal of Physics B-Atomic Molecular and Optical Physics* **1982,** 15, (1), 155-167.
131. Joy, D. C.; Luo, S., An Empirical Stopping Power Relationship for Low-Energy Electrons. *Scanning* **1989,** 11, (4), 176-180.
132. Villarrubia, J. S.; Ritchie, N. W. M.; Lowney, J. R., Monte Carlo modeling of secondary electron imaging in three dimensions - art. no. 65180K. *Metrology, Inspection, and Process Control for Microlithography XXI, Pts 1-3* **2007,** 6518, K5180-K5180.
133. Scholtz, J. J.; Dijkkamp, D.; Schmitz, R. W. A., Secondary electron emission properties. *Philips Journal of Research* **1996,** 50, (3-4), 375-389.
134. Dapor, M., Transport of energetic electrons in solids. *Springer Tracts in Modern Physics* **2014,** 257.
135. Nikzad, S.; Smith, A. L.; Elliott, S. T.; Jones, T. J.; Tombrello, T. A.; Yu, Q., Low-energy electron detection with delta-doped CCDs. *Solid State Sensor Arrays: Development and Applications* **1997,** 3019, 241-248.
136. Watt, F.; Bettiol, A.; Van Kan, J.; Teo, E.; Breese, M., Ion beam lithography and nanofabrication: a review. *International Journal of Nanoscience* **2005,** 4, (03), 269-286.
137. Berger, M. J.; Coursey, J.; Zucker, M.; Chang, J., *Stopping-power and range tables for electrons, protons, and helium ions*.
138. Blumenstock, G. M.; Meinert, C.; Farrar, N. R.; Yen, A., Evolution of light source technology to support immersion and EUV lithography. *Advanced Microlithography Technologies* **2005,** 5645, 188-195.
139. van der Drift, E.; Maas, D. J., *Helium ion lithography*. Springer: 2012.
140. Release, C. Z. S. P. Carl Zeiss SMT Ships World's First ORION Helium Ion Microscope to U.S. National Institute of Standards and Technology.

http://www.smt.zeiss.com/C1256A770030BCE0/WebViewTopNewsAllE/573B9EA1B720BBBEC12573080048AF79
141. ITRS, Metrology. **2009**.
142. Maas, D.; van Veldhoven, E.; van Langen-Suurling, A.; Alkemade, P. F. A.; Wuister, S.; Hoefnagels, R.; Verspaget, C.; Meessen, J.; Fliervoet, T., Evaluation of EUV resist performance below 20-nm CD using helium ion lithography. *Extreme Ultraviolet (Euv) Lithography V* **2014,** 9048.
143. Sidorkin, V.; van Veldhoven, E.; van der Drift, E.; Alkemade, P.; Salemink, H.; Maas, D., Sub-10-nm nanolithography with a scanning helium beam. *Journal of Vacuum Science & Technology B* **2009,** 27, (4), L18-L20.
144. Jeyakumar, A. Development of Inorganic Resists for Electron Beam Lithography: Novel Materials and Simulations. Georgia Institute of Technology, 2004.
145. Kozawa, T.; Tagawa, S., Radiation Chemistry in Chemically Amplified Resists. *Japanese Journal of Applied Physics* **2010,** 49, (3).
146. Livengood, R.; Tan, S.; Greenzweig, Y.; Notte, J.; McVey, S., Subsurface damage from helium ions as a function of dose, beam energy, and dose rate. *Journal of Vacuum Science & Technology B* **2009,** 27, (6), 3244-3249.
147. Mojarad, N.; Gobrecht, J.; Ekinci, Y., Beyond EUV lithography: a comparative study of efficient photoresists' performance. *Scientific Reports* **2015,** 5.
148. Saeki, A.; Kozawa, T.; Tagawa, S.; Cao, H. B.; Deng, H.; Leeson, M. J., Exposure dose dependence on line edge roughness of a latent image in electron beam/extreme ultraviolet lithographies studied by Monte Carlo technique. *Journal of Micro-Nanolithography Mems and Moems* **2007,** 6, (4).
149. Cohen-Tanugi, D.; Yao, N., Superior imaging resolution in scanning helium-ion microscopy: A look at beam-sample interactions. *Journal of Applied Physics* **2008,** 104, (6).
150. Petrov, Y.; Vyvenko, O., Secondary electron emission spectra and energy selective imaging in helium ion microscope. *Scanning Microscopies 2011: Advanced Microscopy Technologies for Defense, Homeland Security, Forensic, Life, Environmental, and Industrial Sciences* **2011,** 8036.
151. Yang, W.; Song, K.; Jung, Y.; Jeong, S.; Moon, J., Solution-deposited Zr-doped AlOx gate dielectrics enabling high-performance flexible transparent thin film transistors. *Journal of Materials Chemistry C* **2013,** 1, (27), 4275-4282.
152. Nayak, P. K.; Wang, Z. W.; Anjum, D. H.; Hedhili, M. N.; Alshareef, H. N., Highly stable thin film transistors using multilayer channel structure. *Applied Physics Letters* **2015,** 106, (10).
153. Nayak, P. K.; Caraveo-Frescas, J. A.; Wang, Z. W.; Hedhili, M. N.; Wang, Q. X.; Alshareef, H. N., Thin Film Complementary Metal Oxide Semiconductor (CMOS) Device Using a Single-Step Deposition of the Channel Layer. *Scientific Reports* **2014,** 4.
154. Luo, F.; Manichev, V.; Li, M.; Mitchson, G.; Yakshinskiy, B.; Gustafsson, T.; Johnson, D.; Garfunkel, E. In *Helium ion beam lithography (HIBL) using HafSOx as the resist*, 2016; 2016; pp 977928-977928-9.
155. Ryan, D.; Parviz, B. A.; Linder, V.; Semetey, V.; Sia, S. K.; Su, J.; Mrksich, M.; Whitesides, G. M., Patterning multiple aligned self-assembled monolayers using light. *Langmuir* **2004,** 20, (21), 9080-9088.
156. French, R. H.; Tran, H. V., Immersion Lithography: Photomask and Wafer-Level Materials. *Annual Review of Materials Research* **2009,** 39, 93-126.
157. Cumpson, P. J., Angle-Resolved Xps and Aes - Depth-Resolution Limits and a General Comparison of Properties of Depth-Profile Reconstruction Methods. *Journal of Electron Spectroscopy and Related Phenomena* **1995,** 73, (1), 25-52.